August 2015

Assembly and Deformation of Amphiphilic Copolymers and Networks at Fluid Interfaces

Jinhye Bae
University of Massachusetts - Amherst

ASSEMBLY AND DEFORMATION OF AMPHIPHILIC COPOLYMERS AND NETWORKS AT FLUID INTERFACES

A Dissertation Presented

by

JINHYE BAE

Submitted to the Graduate School of the
University of Massachusetts Amherst in partial fulfillment
of the requirements for the degree of

DOCTOR OF PHILOSOPHY

MAY 2015

Polymer Science and Engineering

ASSEMBLY AND DEFORMATION OF AMPHIPHILIC COPOLYMERS AND NETWORKS AT FLUID INTERFACES

A Dissertation Presented

by

JINHYE BAE

Approved as to style and content by:

_____
Ryan C. Hayward, Chair

_____
Thomas P. Russell, Member

_____
Anthony D. Dinsmore, Member

_____
David A. Hoagland, Department Head
Polymer Science and Engineering

DEDICATION

To my grandmother and grandfather

ACKNOWLEDGMENTS

First and foremost, I would like to thank my advisor and mentor, Professor Ryan C. Hayward. He has been the most important influence on the accomplishment of my Ph.D. He is a great advisor, scientist, and person. His support, guidance, and patience allowed me to grow as a scientist for 5 years. I should say I truly have enjoyed doing the research under guidance of Ryan. It has been the greatest fortune to have the opportunity to work with and learn from Ryan during my Ph.D.

I sincerely thank my thesis committee, Professor Thomas P. Russell and Professor Anthony D. Dinsmore, both of whom I have had the great pleasure to talk about my research. They always encouraged, taught me, and suggest great ideas by sharing their scientific insight. I have appreciated their interest and support in my research and future career. I also want to thank Professor Kookheon Char at Seoul National University who advised and supported me during and after my M.S., as well as Professor Jinhan Cho at Korea University who encouraged and cared for me scientifically and personally.

I would like to thank my collaborators: Professor Christian Santangelo, Arthur Evans, Professor Jennifer Ross, Michael Gramlich, Professor Thomas Russell, Professor Todd Emrick, Jimmy Lawrence, Caroline Miesch, Professor Jintao Zhu, Weikun Li and Jun-Hee Na. They gave me great opportunities to learn many interesting and different aspects of other fields of science. I am very grateful to all Hayward group members past and present—Jungwook, Le, Ian, Felicia, Scott, Cheolhee, Dayong, Maria, Rachel, Kyle, Anesia, Kyuyoung, Laju, Myunghwan, Bin, Eunji, Jinhwan, Kwanyeol, Junhee, Seog-Jin, Adam, Ying, Nakul, Daniel, Weigu, Tetsu, Di, Hyeongjun, Hyunki, and Qi— always willing to help each other from A to Z. My Ph.D life and research could not be finished in

a good shape without the tremendous help from my collaborators and Hayward group members.

I would like to thank the faculty in the Polymer Science and Engineering department who actually allowed me to study in this department, and have taught me in and out of classes. Also, I want thank the great staff in PSE—Lisa Groth, Cathy Russell, Alyssa Kristek, and Maria Farrigton—for their administrative assistance, and technical staff members—Alex Ribbe, Lou Raboin, and Sekar Thirunavukkarasu—for their support and help on my research. I also want to thank Sophie for managing many of important paper work.

The class of 2009, we started the first day in PSE, went through the first year and cumes together. Now, we have begun or will begin the next step in different places. Best of luck with your bright future. I would like to thank the conte 3rd floor friends, Dan, Jon, Mike, Angela, Yu Cheng and Shruti. Specially, I want to thank Maria (MC), Irem, Yujie (UJ), and Polina for being amazing friends in PSE, I cannot wait for our annual reunion. I would like to thank my friends who are or were in Amherst: Hyunsuk, Jungwon, Dongyun, Paul, Gajin, Jooyoung, Hyunbok, Byoung-jin, Bomee, Jiyeon, Ujin, Soeun, and Hyeyoung.

Finally, I want to thank my parents, grandparents, sister, brother, my family-in-law and Jaewon for your uncountable love and support for the years. You are all a great source of my happiness and energy.

Thank you, I mean you, because you are reading this now. I hope you enjoy this thesis.

ABSTRACT

ASSEMBLY AND DEFORMATION OF AMPHIPHILIC COPOLYMERS AND NETWORKS AT FLUID INTERFACES

MAY 2015

JINHYE BAE, B.S., KYUNG HEE UNIVERSITY

M.S., SEOUL NATIONAL UNIVERSITY

M.S., UNIVERSITY OF MASSACHUSETTS AMHERST

Ph.D., UNIVERSITY OF MASSACHUSETTS AMHERST

Directed by: Professor Ryan C. Hayward

Surface tension generally plays a negligible role on macroscopic scales, but it is often the dominant force on nanometer to micrometer length-scales. The efforts of this dissertation are mainly focused on understanding the role that surface tension plays on sub-millimeter scale objects, especially on soft material systems, and how to utilize this phenomenon to assemble and deform objects. This dissertation addresses several phenomena of nano-and micron-sized objects at fluid interfaces.

For nano-scale objects, amphiphilic block copolymer chains were used to explore interfacial behaviors due to their enhanced stability, mechanical properties, and tunability compared to other interfacially active materials such as small molecule surfactants or lipids. We investigate the tailoring of amphiphilic block copolymer assemblies through deformation at the oil/water interface by inducing interfacial instabilities to incorporate inorganic nanoparticles into micelles (chapter 2) or by controlling osmotic stresses to prepare multi-compartment emulsions and capsules (chapter 3).

Next, we utilize photo-crosslinkable and temperature-responsive copolymer networks (i.e., thin hydrogel sheets) with simple to complex geometries as micro-scale soft objects. Competition between surface energy and elastic bending energy allows us to quantitatively characterize elastic properties of crosslinked thin hydrogel sheets in micron dimensions by using surface tension of liquids (chapter 4). In addition, we have found significant edge imperfections due to the finite resolution of the photo-lithographic patterning method by observation of interfacial deformations. We employ the edge imperfections to drive the buckling of narrow photo-crosslinkable hydrogel ribbons (chapter 5). Lastly, we introduce a new concept of capillary assembly of soft hydrogel sheets with various geometries. This study allows us to examine correlations between elastic properties and surface tension, as well as capillary interactions between soft materials which can be extended to more complex multi-polar interface deformation (chapter 6).

TABLE OF CONTENTS

Page

LIST OF TABLES

Table Page

LIST OF FIGURES

Figure Page

CHAPTER 1

INTRODUCTION

1.1 Surface tension for nano- and micro-scale objects

The origins of the phenomenon known as surface tension lie within the cohesive interactions among liquid molecules. A molecule in the bulk of a liquid phase can interact with all of its neighbors and find itself in a favorable state. By contrast, a molecule packed at an interface loses half of its cohesion interactions and is in an unfavorable energy state. This is the fundamental reason that a liquid droplet adjusts its shape to expose the smallest possible surface area. The surface tension is the cohesion energy per unit surface area, $\gamma \approx U/2a^2$, where U is the cohesion energy per molecule, and a^2 is the exposed area of the molecule. The value of the interfacial tension between two immiscible liquids A and B (γ_{AB}) is characterized by the thermodynamic energy of adhesion between two liquids in contact as well as the cohesion energy for each liquid.[1]

Surface tension generally plays a negligible role at large scales, but it can induce dramatic effects on the sub-millimeter scale. For instance, in the case of placing a compact object with a characteristic length (R) in the range of nano- to micro-meter at a fluid interface, contributions from thermal energy and gravitational forces relative to surface tension should be considered. For a particle at a fluid interface (surface tension $\gamma \sim 10$ mN/m), the interfacial energy $G = \gamma R^2$ greatly exceeds the thermal energy $k_B T$. Thus, the interfacial behaviors of the object predominates over thermal fluctuation during adsorption to the fluid interface. On the other hand, in the case of larger or higher density objects, the gravitational force on the objects may be significant enough to dislodge a particle from the

fluid interface. The balance between gravitational and surface energies is defined by the dimensionless parameter known as the Bond number[2] $Bo = \Delta\rho g R^2 / \gamma$, where $\Delta\rho$ is the difference in density between the particle and the liquid phase, g is the acceleration due to gravity, and R is the characteristic dimension of the object. For an object with $R < 1$ mm, $\Delta\rho \sim 10^3$ kg/m^3, and $\gamma \sim 10$ mN/m, Bo is less than 1. Therefore, in the case of nano- to micro-scale objects, both thermal fluctuation and gravitational forces can be neglected and adsorption to the interface is driven by surface tension. Based on the considerations above, this thesis focuses on the phenomena of nano-and micron-sized objects at a fluid interface, and how we utilize the phenomena to assemble and deform objects.

1.2 The role of surface tension in assembly of amphiphilic block copolymers

Emulsions are thermodynamically unstable systems prepared by one liquid phase dispersed in another immiscible fluid (i.e., emulsification) such as oil-in-water (o/w) or water-in-oil (w/o). The stability of emulsions can be enhanced by the presence of surface active species that effectively adsorb at the interface, and prevent or delay their destructions by coalescence or Ostwald ripening.[3, 4] These irreversible transitions by coalescence between dispersed droplets are driven in order to reduce their Laplace pressure.[1, 5] For instance, when liquid *A* is dispersed as a spherical droplet with radius *r* in liquid *B*, a Laplace pressure difference (ΔP) arises between the interior and exterior of the droplet.

$$\Delta P = \frac{2\gamma_{AB}}{r}$$

Where γ_{AB} is the interfacial tension between two immiscible liquids *A* and *B*. When the interfacial tension is fixed, the smaller droplet induces the greater pressure difference according to this relationship.

In this thesis, we will investigate *non-classical* behaviors and choose amphiphilic copolymer chains as surface active agents which strongly adsorbs to liquid/vapor or liquid/liquid interfaces due to their amphiphilicity. Indeed, amphiphilic block copolymers have significant advantages in terms of mechanical properties, stability, and tunability compared to other surface active species such as small molecule surfactants, nanoparticles or lipids.[6] For a few decades, the combination of emulsification and solvent evaporation processes has been considered a useful means to prepare copolymer assemblies of microspheres for drug delivery.[7, 8] Weitz and co-workers[9-12] have contributed to this area with microfluidic techniques to form single to multiple emulsions stabilized by block copolymers with controllable size and structures.

Zhu and Hayward have reported on the formation of exotic structures of block copolymer assemblies including budding vesicles and dendritic particles,[13] and the effect of surfactant concentration on the amphiphilic block copolymer assemblies via solvent evaporation induced interfacial instabilities upon emulsion processing.[14, 15] They observed a significant reduction in interfacial tension of the organic solvent containing amphiphilic block copolymers/aqueous solution interface during removal of the organic phase. Subsequently, this interface becomes unstable, which is associated with an approach to near zero interfacial tension. These solvent evaporation-induced instabilities eventually deform the interface and the copolymer chains rearrange depending on their packing parameter (shape factor).[16, 17] We will adopt the interfacial instabilities to fabricate

multifunctional assemblies of amphiphilic copolymers by encapsulation of various hydrophobic nanoparticles. Next, the focus of interest will be on osmotic pressure, which can act as a counterpart to Laplace pressure in the development of osmotically-driven emulsification to tailor amphiphilic block copolymer assemblies

1.3 Balance between surface energy and elastic energy of copolymer networks

Since capillary forces (~ R) decrease slower than pressure (~ R^2) and body forces (~ R^3), when the characteristic length (R) of a given object is scaled down, capillary forces become dominant. Previous studies on the interplay between capillarity and elasticity have focused on deformations of slender structures by capillary forces. The dimension criterion for dominance of capillary force on a liquid droplet is generally explained by the capillary length $R_c = \sqrt{\gamma / \rho g}$, where ρ is the liquid density and g gravitational acceleration.[1, 18]

In real life, we experience hairs and brushes assemble into bundles by wetting with water. Similarly, the capillary attraction and stiction of slender structures in contact with a liquid gives rise to hierarchical bundling[19, 20] and can cause disastrous damage in micro and nanoscale devices.[21-24] Capillary interactions have also been utilized as a means to assemble and orient solid objects in 2-dimensions at the fluid surface.[25, 26] Furthermore, capillary interactions have shown to be a useful way to build 3-dimesional microstructures by folding of thin sheets with a liquid droplet.[27-32]

These previous studies have shown that surface energy of a fluid is comparable to the energy necessary to deform sub-millimeter scale flexible objects. That means the fluid surface tension can be utilized as a versatile probe to characterize the elastic properties,

thus this phenomenon can potentially be exploited as a metrology for characterizing elastic properties. Here, the balance between interfacial tension and elastic properties of a micro-scale objects with low elastic moduli (E) consisting of thin elastic sheets can be explained by two dimensionless parameters.[18, 33] The first is the elasto-capillary bending number, $C_b = B/\gamma R^2$, which is the ratio of the bending modulus ($B = Eh^3/12(1-\nu^2) = \overline{E}h^3/12$, where ν is Poisson's ratio and $\overline{E}$ is the plane stain modulus) of sheet to a characteristic length of R and surface tension of a fluid (γ). For the case of $C_b \leq 1$, the surface tension can make changes in mean curvature of such an elastic sheet by interfacial adsorption; whereas, the bending behaviors do not depend on surface tension for $C_b >> 1$. The other parameter is the elasto-capillary stretching number, $C_s = Y/\gamma$ (where the areal stretching modulus is $Y = Eh/(1-\nu)$) of the sheet. When $C_s >> 1$, the surface tension cannot stretch or unstretch the thin elastic sheets; otherwise, the fluid interface can distort the configuration of soft objects associated with a stretching energy contribution for $C_s \leq 1$.

In this thesis, we will focus on understanding the role of surface tension on bendable thin objects at the fluid interface. Then, we will explore the bending behavior of thin polymer sheets due to a liquid droplet in terms of initial geometry of sheet and contact angle of a liquid droplet to quantitatively measure the elastic moduli of thin sheets. Furthermore, we will study how the fluid interface can be effectively deformed according to a configuration of elastic soft objects to understand the competition between elastic and surface energies. Finally, we will explore 2-dimensional assemblies of soft objects due to induced capillary interactions.

1.4 References

1. de Gennes, P. G., Brochard-Wyart, F. & Quere, D. *Capillarity and wetting phenomena: Drops, bubbles, pearls, waves*. Springer (2003).

2. Hager, W. H. Wilfrid Noel Bond and the Bond number. *Journal of Hydraulic Research* **50**, 3-9 (2012).

3. Bibette, J., Calderon, F. L. & Poulin, P. Emulsions: Basic principles. *Rep Prog Phys* **62**, 969-1033 (1999).

4. Lopez-Montilla, J. C., Herrera-Morales, P. E., Pandey, S. & Shah, D. O. Spontaneous emulsification: Mechanisms, physicochemical aspects, modeling, and applications. *J Disper Sci Technol* **23**, 219-268 (2002).

5. Aserin, A. *Multiple emulsion: Technology and applications*. Wiley (2008).

6. Wyman, I., Njikang, G. & Liu, G. When emulsification meets self-assembly: The role of emulsification in directing block copolymer assembly. *Progress in Polymer Science* **36**, 1152-1183 (2011).

7. Ogawa, Y., Yamamoto, M., Okada, H., Yashiki, T. & Shimamoto, T. A new technique to efficiently entrap leuprolide acetate into microcapsules of polylactic acid or copoly(lactic/glycolic) acid. *Chem Pharm Bull* **36**, 1095-1103 (1988).

8. Ouchi, T., Hamada, A. & Ohya, Y. Biodegradable microspheres having reactive groups prepared from l-lactic acid-depsipeptide copolymers. *Macromol Chem Physic* **200**, 436-441 (1999).

9. Utada, A. S., Lorenceau, E., Link, D. R., Kaplan, P. D., Stone, H. A. & Weitz, D. A. Monodisperse double emulsions generated from a microcapillary device. *Science* **308**, 537-541 (2005).

10. Hayward, R. C., Utada, A. S., Dan, N. & Weitz, D. A. Dewetting instability during the formation of polymersomes from block-copolymer-stabilized double emulsions. *Langmuir* **22**, 4457-4461 (2006).

11. Kim, S. H., Shum, H. C., Kim, J. W., Cho, J. C. & Weitz, D. A. Multiple polymersomes for programmed release of multiple components. *J Am Chem Soc* **133**, 15165-15171 (2011).

12. Kim, S. H. & Weitz, D. A. One-step emulsification of multiple concentric shells with capillary microfluidic devices. *Angewandte Chemie-International Edition* **50**, 8731-8734 (2011).

13. Zhu, J. & Hayward, R. C. Hierarchically structured microparticles formed by interfacial instabilities of emulsion droplets containing amphiphilic block copolymers. *Angew. Chem. Int. Ed.* **47**, 2113-2116 (2008).

14. Zhu, J. T., Ferrer, N. & Hayward, R. C. Tuning the assembly of amphiphilic block copolymers through instabilities of solvent/water interfaces in the presence of aqueous surfactants. *Soft Matter* **5**, 2471-2478 (2009).

15. Zhu, J. & Hayward, R. C. Interfacial tension of evaporating emulsion droplets containing amphiphilic block copolymers: Effects of solvent and polymer composition. *J Colloid Interf Sci* **365**, 275-279 (2012).

16. Blanazs, A., Armes, S. P. & Ryan, A. J. Self-assembled block copolymer aggregates: From micelles to vesicles and their biological applications. *Macromolecular Rapid Communications* **30**, 267-277 (2009).

17. Rodríguez-Hernández, J., Chécot, F., Gnanou, Y. & Lecommandoux, S. Toward 'smart' nano-objects by self-assembly of block copolymers in solution. *Progress in Polymer Science* **30**, 691-724 (2005).

18. Roman, B. & Bico, J. Elasto-capillarity: Deforming an elastic structure with a liquid droplet. *J Phys-Condens Mat* **22**, (2010).

19. Bico, J., Roman, B., Moulin, L. & Boudaoud, A. Elastocapillary coalescence in wet hair. *Nature* **432**, 690-690 (2004).

20. Kim, H. Y. & Mahadevan, L. Capillary rise between elastic sheets. *J. Fluid Mech.* **548**, 141-150 (2006).

21. Tanaka, T., Morigami, M. & Atoda, N. Mechanism of resist pattern collapse during development process. *Jpn J Appl Phys 1* **32**, 6059-6064 (1993).

22. Chakrapani, N., Wei, B. Q., Carrillo, A., Ajayan, P. M. & Kane, R. S. Capillarity-driven assembly of two-dimensional cellular carbon nanotube foams. *Proc. Natl. Acad. Sci. USA* **101**, 4009-4012 (2004).

23. Mastrangelo, C. H. & Hsu, C. H. Mechanical stability and adhesion of microstructures under capillary forces. I. Basic theory. *Microelectromechanical Systems, Journal of* **2**, 33-43 (1993).

24. Raccurt, O., Tardif, F., d'Avitaya, F. A. & Vareine, T. Influence of liquid surface tension on stiction of soi mems. *J Micromech Microeng* **14**, 1083-1090 (2004).

25. Bowden, N., Choi, I. S., Grzybowski, B. A. & Whitesides, G. M. Mesoscale self-assembly of hexagonal plates using lateral capillary forces: Synthesis using the

"capillary bond". *Journal of the American Chemical Society* **121**, 5373-5391 (1999).

26. Botto, L., Lewandowski, E. P., Cavallaro, M. & Stebe, K. J. Capillary interactions between anisotropic particles. *Soft Matter* **8**, 9957-9971 (2012).

27. Py, C., Reverdy, P., Doppler, L., Bico, J., Roman, B. & Baroud, C. N. Capillary origami: Spontaneous wrapping of a droplet with an elastic sheet. *Phys. Rev. Lett.* **98**, 156103 (2007).

28. van Honschoten, J. W. *et al.* Elastocapillary fabrication of three-dimensional microstructures. *Appl Phys Lett* **97**, - (2010).

29. Guo, X. Y. *et al.* Two- and three-dimensional folding of thin film single-crystalline silicon for photovoltaic power applications. *Proc. Natl. Acad. Sci. USA* **106**, 20149-20154 (2009).

30. Syms, R. R. A., Yeatman, E. M., Bright, V. M. & Whitesides, G. M. Surface tension-powered self-assembly of microstructures - the state-of-the-art. *Microelectromechanical Systems, Journal of* **12**, 387-417 (2003).

31. de Langre, E., Baroud, C. N. & Reverdy, P. Energy criteria for elasto-capillary wrapping. *Journal of Fluids and Structures* **26**, 205-217 (2010).

32. Li, H. A., Guo, X. Y., Nuzzo, R. G. & Hsia, K. J. Capillary induced self-assembly of thin foils into 3d structures. *Journal of the Mechanics and Physics of Solids* **58**, 2033-2042 (2010).

33. Py, C., Reverdy, P., Doppler, L., Bico, J., Roman, B. & Baroud, C. N. Capillary origami: Spontaneous wrapping of a droplet with an elastic sheet. *Physical Review Letters* **98**, (2007).

CHAPTER 2

MULTIFUNCTIONAL NANOPARTICLE-LOADED SPHERICAL AND WORMLIKE MICELLES FORMED BY INTERFACIAL INSTABILITIES*

2.1 Introduction

Multifunctional nano-objects containing discrete domains of different inorganic materials are of interest for their ability to combine the advantageous optical, magnetic, or electronic properties of the constituent materials. Such heterostructures are commonly formed through seeded-growth of one material on seed particles of another, yielding core/shell, peanut-, dumbbell- or flower-like composite nanoparticles.[1-8] Other approaches include embedding of different inorganic materials together within silica spheres,[9, 10] or within polymer particles or capsules.[11] A recent approach of interest is the encapsulation of multiple different individually synthesized inorganic nanoparticles within the hydrophobic domains of self-assembled polymer micelles. Such structures offers particular promise for applications in nanomedicine through the combination of diagnostic and therapeutic components in one delivery system, [12-17] for example to allow any desired combination of magnetic targeting, fluorescence imaging, MRI imaging, photothermal therapy, and drug delivery capabilities in a single vehicle. In this case, the role of the polymer micelle is not only to bind together the different nanoparticles and protect them from the surrounding environment, but also to yield additional control over the

* Reproduced and modified with permission from J. Bae, J. Lawrence, C. Miesch, A. Ribbe, W. Li, T. Emrick, J. Zhu, and R. C. Hayward, "Multifunctional Nanoparticle-Loaded Spherical and Wormlike Micelles Formed by Interfacial Instabilities", *Advanced Materials*, **24**, 2735-2741 (2012). Copyright © 2012 WILEY-VCH Verlag GmbH & Co. KGaA, Weinheim

morphology,[18-22] degradability,[23-26] and chemical functionality[27-31] of the resulting hybrid nano-objects.

Co-encapsulation of magnetic nanoparticles and quantum dots,[32-34] or magnetic nanoparticles and gold nanoparticles,[33] within amphiphilic polymer micelles has been achieved using a "precipitation" processing route. In this method, water is added to a solution of amphiphilic block copolymers and hydrophobic nanoparticles initially dispersed in a good solvent for both materials. As the result of simultaneous desolvation of both the nanoparticles and the hydrophobic block of the amphiphilic block copolymer, nanoparticles are incorporated into the cores of the copolymer micelles. These studies have focused on spherical micelles as vehicles, because the need to achieve synchronous precipitation of nanoparticles and block copolymer does not easily lend itself to growth of extended cylindrical aggregates.

Given the advantages offered by wormlike, or cylindrical, micelles as nano-carriers, in terms of providing high loading capacity of hydrophobic objects per micelle and long *in vivo* circulation times,[35-37] preparation of nanoparticle-loaded cylindrical micelles is of considerable interest. There have been several reports of *in situ* formation of nanoparticles within the cores[38-40] or coronae[41] of wormlike micelles, as well as adsorption of pre-formed nanoparticles into the micelle corona.[42-44] Li, et al. have shown that block copolymer cylinders loaded with nanoparticles in the melt state can be dispersed in aqueous media to form cylinder micelles.[45] Recently, Mai and Eisenberg have successfully incorporated gold nanoparticles into cylindrical micelle cores by precipitation; however, this required pre-coating the nanoparticles with a custom polystyrene-block-poly(acrylic acid) diblock copolymer ligand that matched the chemistry of the micelle forming copolymer.[46] To our

knowledge, multifunctional wormlike micelles containing multiple encapsulated inorganic nanoparticles have not previously been reported.

We have recently developed an alternative process to drive assembly of amphiphilic polymer micelles that we term the "interfacial instability" route.[47] In this approach, the tendency of amphiphilic polymer chains to populate the interface between water and evaporating droplets of organic solvent leads to a near vanishing of the solvent/water interfacial tension and corresponding hydrodynamic instabilities of the droplet surfaces that lead to generation of copolymer micelles. As we have described previously, the tendency for hydrophobic species dispersed in the organic phase to be entrained as the micelles form provides a viable route to encapsulate nanoparticles within spherical and wormlike micelles, albeit with pronounced non-uniformities in particle distribution.[47] Winter and co-workers used this interfacial instability method to fabricate of multifunctional spherical micelles containing quantum dots and magnetic nanoparticles,[14, 48] as well as quantum dots with different colors of fluorescence emission.[49]

In the current chapter, we show that this method is general to the encapsulation of several different types of pre-synthesized hydrophobic inorganic nanoparticles within both spherical and wormlike micelles of amphiphilic block copolymers. For the case of cylindrical micelles, loading is found to be both efficient and rather uniform, with essentially every micelle containing encapsulated particles. For spherical micelles, the uniformity of nanoparticle loading is not as high, but simple centrifugal or magnetic separation steps allow for straightforward enrichment of samples to ~ 90 % of loaded micelles. The encapsulation behavior of hydrophobic nanoparticles is found to be surprisingly insensitive to particle surface chemistry, shape, and size (from ~ 1 to 20 nm),

thus providing a flexible route to fabricate multi-functional spherical and wormlike micelles.

2.2 Experimental

2.2.1 Materials and methods

Copper(I) bromide, N,N,N',N',N''-pentamethyldiethylenetriamine (PMDETA) 1-phenylethyl bromide (1-PEBr) (Aldrich, purity: 97%). NaOH (Fisher), gold(III) chloride trihydrate ($HAuCl_4.3H_2O$), cetyltrimethyl ammonium bromide (CTAB), sodium citrate tribasic dehydrate, iron(III) acetylacetonate (Fe(III) $(acac)_3$), hexadecanediol, phenyl ether, cadmium acetate dihydrate ($Cd(ac)_2$), trioctylphosphine oxide (TOPO), selenium powder (Se) (Alfa Aesar) and trioctylphosphine (TOP) (Alfa Aesar) were used as received. Styrene was purified from inhibitor by passing through an alumina column before use. All chemicals listed above were obtained from Aldrich, except where noted.

Solvent-in-water emulsions were formed by mixing the organic phase (chloroform containing 10 mg/mL PS-PEO and 1.0 mg/mL nanoparticles) with the aqueous phase (deionized water containing 5 mg/mL poly(vinyl alcohol); M_w=13-23 kg/mol, 87-89% hydrolyzed; Aldrich) in a 1:5 volumetric ratio and shaking by hand. Following emulsification, samples were diluted by an additional factor of 5 with deionized water, and the emulsion was left open to air in a glass container (3.6 mL of the emulsion in a 20 mL vial) with magnetic stirring at 60 rpm, to allow evaporation of chloroform and micelle formation. Loaded micelles were separated from PVOH and empty micelles by centrifugation at 10 krpm (or 6700 × g) for 15 min, after which the upper 80-90 % of solution was discarded and the same volume of deionized water added. This procedure was

repeated 5 times. In the case of micelles loaded with magnetic nanoparticles, purification could also be achieved using an equivalent procedure with separation by holding a permanent magnet at the bottom of the vial for 3 - 5 min instead of centrifugation. Experiments were conducted using two PS-PEO diblock copolymers purchased from Polymer Source Inc. (M_n = 9.5 kg/mol - 9.5kg/mol and 19 kg/mol - 6.4kg/mol).

Magnetic nanoparticles (Fe_3O_4) dispersed in hexane were prepared according to the procedure of Sun et al.[50] Iron(III) acetylacetonate ($Fe(acac)_3$, 2 mmol), phenyl ether (20 ml), 1,2-hexadecane diol (10 mmol), oleic acid (6 mmol) and oleylamine (6 mmol) were mixed in a flask equipped with a thermocouple, magnetic stirring bar and condenser, and sealed with rubber septa and stirred under N_2 atmosphere. The mixture was heated to 200 °C for 30 min and heated to reflux (265 °C) for 30 min. The dark brown mixture was cooled down to room temperature, precipitated with ethanol and centrifuged. The product was dissolved in a hexane solution of (~20 mL) oleic acid and oleylamine (each 0.05 mL). The undispersed residue was removed by centrifugation of this solution (6 krpm (or 2400 × g), 10 min). The product was precipitated with ethanol, centrifuged (6 krpm (or 2400 × g), 10 min) and redispersed into hexane.

CdSe quantum dots were synthesized according to the literature procedure.[51] Briefly, 0.0514 g of CdO, 0.223 g of TDPA and 3.78 g of TOPO were loaded into a 25 mL 3-neck flask. The flask was equipped with thermocouple, stirring bar, and condenser, and sealed with rubber septa. The mixture was heated to 300-320 °C under N_2 flow until CdO was dissolved. The solution was cooled down to 270 °C and Se-TOP stock solution (0.066 selenium powder dissolved in 2 g of TOP) was swiftly injected to the flask. The

nanocrystals were let to grow at 250 °C to reach target size. Quantum dot size can also be adjusted by increasing the heating time of the precursor solution prior to Se injection.

Dodecanethiol covered gold nanoparticles (5 nm diameter) were purchased from Ocean NanoTech (AuO-05-0025). Gold nanoparticles coated with PS ligands were prepared by first synthesizing 4 nm diameter particles using the seeding growth method.[52] A 20 mL aqueous solution of $HAuCl_4.3H_2O$ (0.25 mM) and trisodium citrate (0.25 mM) was stirred in a flask; then 0.6 mL of ice-cold, freshly prepared $NaBH_4$ solution (0.1 M) was added. These nanoparticles were also used as seed particles to obtain 7 nm gold nanoparticles. A growth solution was prepared by adding 6 g of CTAB into $HAuCl_4$ aqueous solution (200 mL, 0.25 mM) under heating until the solution turned orange and then cooled to room temperature. In another flask, 9 mL of the above growth solution was mixed with 0.05 mL of 0.1 M ascorbic acid solution and 1 mL of the suspension of seed particles was added under vigorous stirring (10 minutes).

CdSe nanorods were prepared as described previously.[53] CdO (0.204 g, 1.6 mmol), TDPA (0.89 g, 3.2 mmol) and TOPO (2.9 mg, 7.5 mmol) were loaded into a 25 mL three-neck round-bottom flask equipped with condenser, inlet and septa, and heated to 320 ˚C under an inert atmosphere. After the initially brown solution turned colorless, the solution was cooled to room temperature and aged for 3 days. A solution of Se (63 mg, 0.80 mmol), tri-n-butylphosphine (0.23 g, 1.1 mmol), TOP (1.45 g, 3.9 mmol) and anhydrous toluene (0.3 mL, 2.8 mmol) was quickly injected into the initial mixture heated to 320˚C under inert atmosphere. The reaction was maintained at 250˚C for 30 minutes and then cooled to 50˚C. Anhydrous methanol was slowly added to the red solution to precipitate the quantum

dots. The quantum dots were centrifuged and washed with a mixture of toluene/methanol in a ratio of 1/1.

Thiol terminated polystyrene was synthesized by atom transfer radical polymerization ([M]:[I]:[CuBr]:[PMDETA]=18:1:0.3:0.3, 100 °C, 4 h). The obtained polymer was diluted with tetrahydrofuran and precipitated twice in cold MeOH, filtered and dried *in vacuo*. Functionalization of polymer chain end from bromine to thiol was carried out by reacting the bromine terminated PS with thiourea, followed by treatment with NaOH.[54] (M_w: 5.2k, M_n: 4.5k, PDI: 1.15).

In a typical experiment, CdSe nanoparticles (7.5 mg) in $CHCl_3$ were added drop-wise to 75 mg of thiol terminated PS in $CHCl_3$. The mixture was sonicated for 30 min and incubated overnight. The solution was later subjected to dialysis (Spectrum Laboratories, MWCO 10k) for 3 d, followed by centrifugation. The precipitated nanoparticles were dispersed in chloroform and washed with methanol to remove traces of TOPO and free polymer.

Gold nanoparticles stabilized with thiol terminated polystyrene ligand were prepared by mixing the obtained citrate stabilized gold nanoparticle aqueous solution with 50 mg of PS-SH dissolved in 10 mL of chloroform. The mixture was added with acetone to transfer nanoparticles to the organic phase. The organic layer was washed with brine and precipitated by centrifugation (13 krpm (or 11400 × g), 30 min) after adding acetone/MeOH (1:2) mixture. The nanoparticle-polymer solution was redispersed in chloroform, washed with acetone/MeOH mixture and centrifuged 2 or 3 times at 5 krpm (1700 × g) for 15 min to remove excess polymers.

2.2.3 Fabrication of functional micelles by interfacial instabilities

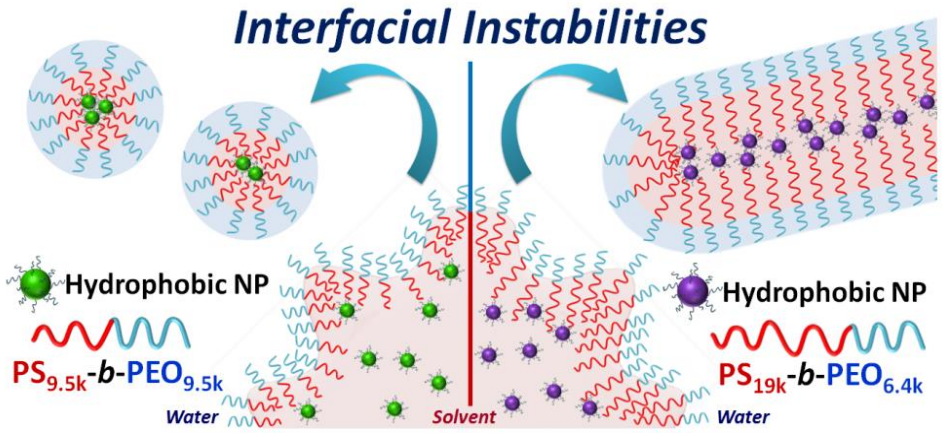

Figure 2.1 Schematic illustration of the formation of nanoparticle-loaded spherical and wormlike amphiphilic block copolymer micelles by evaporation-induced interfacial instabilities of emulsion droplets.

Formation of nanoparticle-loaded micelles was investigated using amphiphilic polystyrene-block-poly (ethylene oxide) (PS-PEO) diblock copolymers. The copolymers were initially dissolved in chloroform along with hydrophobic inorganic nanoparticles, and this solution was emulsified in water containing poly(vinyl alcohol) (PVOH) as a surfactant. Here, we used 87-89 % hydrolyzed PVOH, this hydrolysis degree is determined by the percentage of acetate groups converted to alcohol groups. Thus, due to the hydrophobic character of remaining acetate groups, this partially hydrolyzed PVOH can act as a surface active agent. Prepared emulsions were left in an open glass container and stirred magnetically (at 60 rpm) to enhance the rate and uniformity of solvent removal; stirring was continued for 2 days to completely remove chloroform. The increasing concentration of PS-PEO within each shrinking droplet eventually triggered spontaneous roughening of the organic/water interface and subsequent ejection of either spherical or wormlike micelles, as dictated primarily by the hydrophilic/hydrophobic balance of the diblock

copolymer (Figure 2.1).[47] Notably, stirring of the emulsions during solvent evaporation was found to increase the curvature of the micellar structures formed; while $PS_{9.5k}$-$PEO_{9.5k}$ (weight faction of PEO, f_{EO} = 0.50) yields a mixture of spherical and wormlike micelles for evaporation under quiescent conditions,[47] here it gave exclusively spherical micelles. Similarly, the morphology adopted by PS_{19k}-$PEO_{6.4k}$ (f_{EO} = 0.25) was found to shift from a mixture of wormlike and lamellar structures[47] to exclusively cylindrical micelles.

2.2.2 Characterization

The morphologies of micelles and encapsulated nanoparticles were observed by drop casting solutions on TEM grids coated with a carbon film, and performing bright field TEM on unstained samples using a JEOL 2000FX electron microscope operated at an accelerating voltage of 200 kV. HAADF-STEM measurements where performed using an FEI Magellan 400 FESEM in STEM mode equipped with the HAADF detector, and elemental analysis was performed using an EDX detector (Oxford Instruments X-MAX). The microscope was operated at 20 kV and beam current 3.2 nA. Movement of fluorescent micelles in the presence of an applied magnetic field was monitored using a Zeiss Axiovert 200 inverted optical microscope with a 100X oil-immersion objective. Thermogravimetic analysis (TGA) was carried out on a TA Instruments TGA Q500. Samples were analyzed in platinum pans at a heating rate of 5 °C/min to 120 °C and then 10 °C/min to 500 °C under flow of N_2.

2.3 Results and discussion

2.3.1 Encapsulation of singe particles into micelles

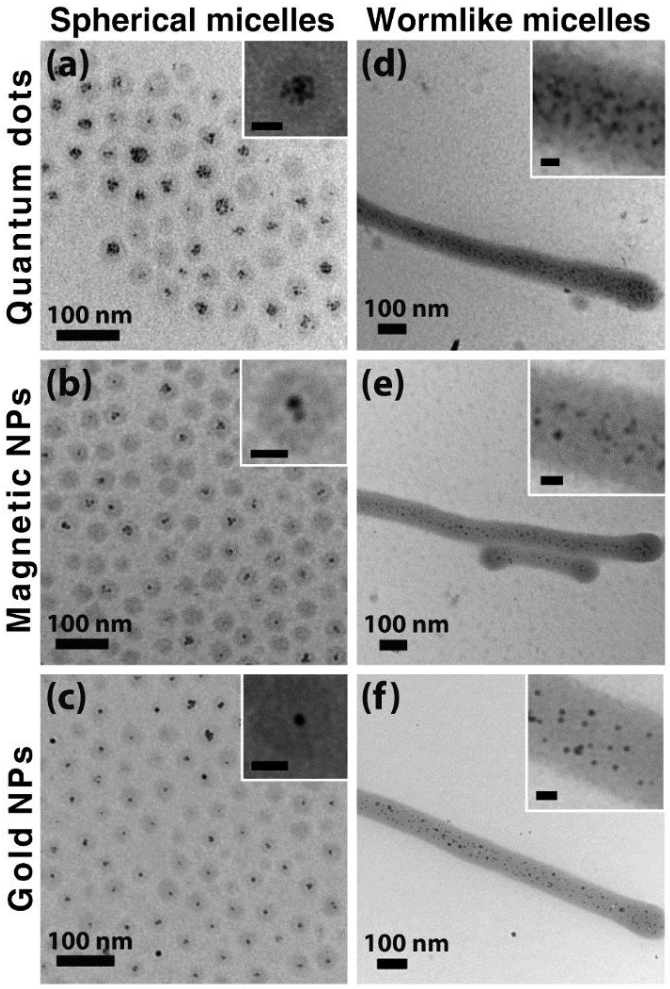

Figure 2.2 TEM images of PS-PEO micelles with hydrophobic nanoparticles encapsulated in their PS cores. Spherical micelles of $PS_{9.5k}$-$PEO_{9.5k}$ with (a) CdSe-TOPO nanoparticles; (b) oleic acid/oleylamine-coated iron oxide nanoparticles; and (c) Au-DDT nanoparticles. Wormlike micelles of PS_{19k}-$PEO_{6.4k}$ with (d) CdSe-TOPO nanoparticles; (e) oleic acid/oleylamine-coated iron oxide nanoparticles; and (f) Au-DDT nanoparticles. Insets: magnified images (scale bars, 20 nm).

Formation of micelles by hydrodynamic interfacial instabilities provides a simple and effective means to encapsulate hydrophobic nanoparticles within micelle cores.[14, 48, 49] For example, Figure 2.2 shows transmission electron microscope (TEM) images of both

spherical and wormlike micelles containing three different types of spherical nanoparticles—CdSe (4 nm diameter), gold (5 nm), and iron oxide (1 - 10 nm)—each bearing the native alkane ligands used in particle synthesis, i.e., trioctylphosphine oxide (TOPO), dodecanethiol (DDT), and oleic acid/oleylamine, respectively. Similar results were also obtained for larger CdSe nanoparticles (7 nm) and CdSe nanorods (3 x 18 nm) (Figure 2.3). To probe the importance of particle surface chemistry, CdSe and gold nanoparticles were functionalized with thiol-terminated polystyrene (M_n = 4.5 kg/mol) and examined in micelle formation. In both cases, no significant differences in the encapsulation behavior were observed between the PS-coated nanoparticles (Figure 2.4) and those with alkane ligands, indicating that encapsulation of hydrophobic nanoparticles in this manner does not require careful matching of the interactions between the particles and the core-forming blocks of the copolymers. Further, our results show that the method is applicable to a variety of different particle core chemistries, and appropriate for both spherical and rod-like particles of at least ~ 1 – 10 nm diameter.

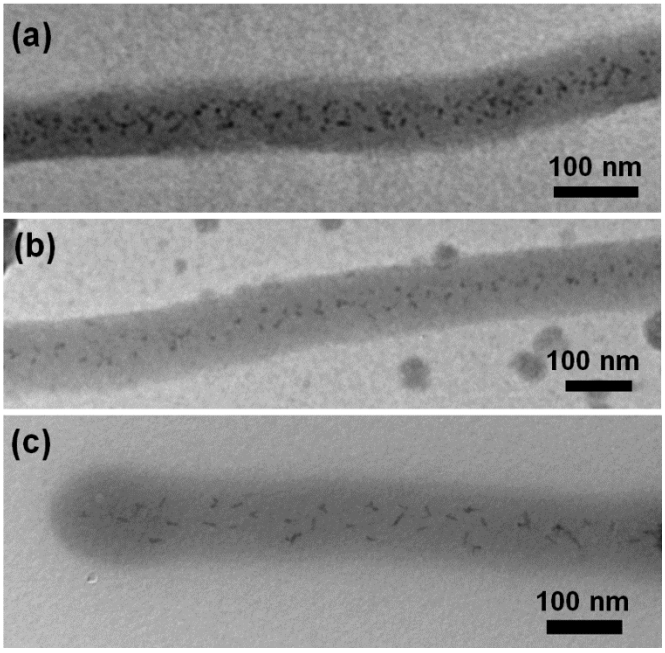

Figure 2.3 TEM images of wormlike micelles of PS_{19k}-$PEO_{6.4k}$ with (a) CdSe-PS nanoparticles (7 nm), (b) CdSe-TOPO nanoparticles (7 nm), and (c) CdSe-TOPO nanorods.

Importantly, the TEM images in Figure 2.2 reveal fairly uniform loading of nanoparticles within micelles. For the case of wormlike micelles (Figure 2.2d-f), essentially every micelle was found to contain nanoparticles, and the density of nanoparticles was quite regular along the length of each individual micelle, and varied only slightly between micelles. Spherical micelles showed somewhat less uniformity of nanoparticle loading, as seen in Figure 2.2a-c, including a significant fraction (typically 20 - 50 %) of empty micelles. The reduced uniformity for the spherical micelles likely arises from two effects. The first is simply geometrical, i.e., since spheres have much lower loading capacity per micelle compared to cylinders, the probability of finding an empty micelle is higher. Second, the molecular weight of the core block of the sphere-forming $PS_{9.5k}$-$PEO_{9.5k}$ is half that of the cylinder-forming PS_{19k}-$PEO_{6.4k.}$ To confirm the influence of core molecular weight, we also tested loading of nanoparticles within spherical micelles

prepared from higher molecular weight polymers, PS_{40k}-PEO_{36k}. The fraction of nanoparticle-loaded micelles was found to improve substantially; for the case of magnetic nanoparticles, micelles of PS_{40k}-PEO_{36k} showed 91 ± 3 % loaded micelles, compared to 50 ± 5 % for $PS_{9.5k}$-$PEO_{9.5k}$. Within loaded micelles, the mean number (± standard deviation) of nanoparticles was 7 ± 4 for PS_{40k}-PEO_{36k} (Figure 2.4) compared to 2 ± 1 for $PS_{9.5k}$-$PEO_{9.5k}$, reflecting a comparable relative breadth in the distribution of the number of particles per micelle. These findings represent substantial improvements over previous results wherein significant nonuniformity between and within even wormlike micelles was found when solvent was evaporated under quiescent conditions.[47]

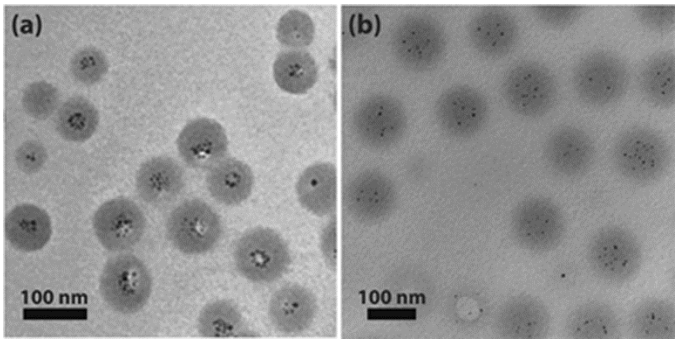

Figure 2.4 TEM images of spherical micelles of PS_{40k}-PEO_{36k} with (a) iron oxide- oleic acid/oleylamine nanoparticles and (b) Au-PS nanoparticles (4 nm) encapsulated in the PS cores.

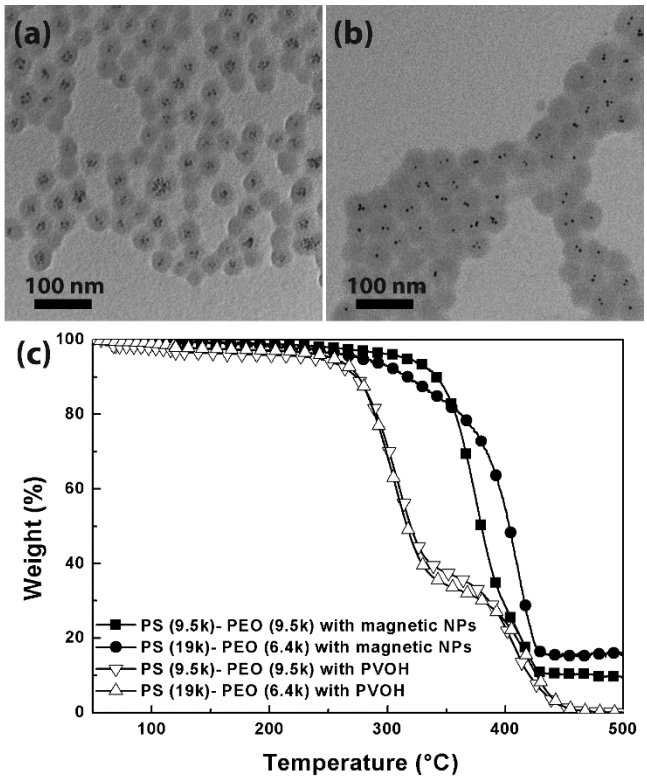

Figure 2.5 TEM images of hybrid spherical micelles of $PS_{9.5k}$-$PEO_{9.5k}$ with (a) encapsulated iron oxide nanoparticles purified using a permanent magnet and (b) encapsulated Au-DDT nanoparticles purified by centrifugation. (c) Thermogravimetric analyses of magnetically purified spherical $PS_{9.5k}$-$PEO_{9.5k}$ and cylindrical PS_{19k}-$PEO_{6.4k}$ micelles with encapsulated iron oxide nanoparticles reveal the effective removal of PVOH, and allow the average inorganic content to be determined.

To further improve the uniformity of nanoparticle distribution within spherical micelles, and also remove PVOH, simple separations were performed. For the case of micelles containing magnetic nanoparticles, a permanent magnet was used to concentrate loaded particles, followed by removal of the supernatant and resuspension (5 times). For micelles loaded with non-magnetic particles, centrifugation at 10 krpm (6700 × g) for 15 min (5 times) was used to similar effect. Following either type of purification, typically 80 – 90 % of micelles were loaded with nanoparticles. For example, Figure 2.5a shows a

purified sample containing magnetic nanoparticles enriched to 86 ± 1 % of loaded micelles, while Figure 2.5b shows micelles containing Au-DDT nanoparticles enriched to 78 ± 5 %.

To determine the quantity of nanoparticles loaded within micelles, we performed thermogravimetric analysis (TGA) on dried suspensions following magnetic or centrifugal purification. As shown in Figure 2.5c for micelles containing magnetic nanoparticles, a single-step degradation of polymer centered around 370 °C for spherical $PS_{9.5k}$-$PEO_{9.5k}$ micelles and 390 °C for wormlike PS_{19k}-$PEO_{6.4k}$ micelles was observed. For comparison, TGA was also performed on micelles of both copolymers without encapsulated nanoparticles, and not subjected to any purification steps. In these cases (Figure 2.5c), clear two-step degradation was observed; the first step, centered around 270 °C corresponds to decomposition of PVOH, which occurs at lower temperature than PS-PEO.[55] Since the lower temperature degradation was not observed for samples of loaded micelles purified in either way, we conclude that purification successfully removed the large majority of PVOH. Thus, comparing the mass of inorganic material remaining after heating to the initial mass of the purified loaded micelles provides a reliable measurement of the quantity of encapsulated nanoparticles. As summarized in Table 2.1, the inorganic content determined in this manner for nanoparticles coated with native alkane ligands ranged from 4 to 15 wt %, with slightly higher values for gold than either iron oxide or CdSe. Given the composition changes that occur during purification, these values are in reasonable agreement with the initial content of nanoparticles in the organic solvent of 9 wt % (relative to PS-PEO and nanoparticles), highlighting that this method provides an efficient means to load significant quantities of inorganic material within micelles.

Table 2.1 Inorganic content for nanoparticle-loaded spherical and wormlike micelles of PS-PEO block copolymers after purification by centrifugation.

Nanoparticles	Inorganic content (wt %)	
	Spherical micelles	Wormlike micelles
CdSe	6.2 ± 0.1	4.3 ± 0.1
Fe_3O_4	6.4 ± 0.3	7.0 ± 0.4
Au	14.9 ± 0.2	10.1 ± 0.2

2.3.2 Co-encapsulated nanoparticle within micelles

Having established that three different types of nanoparticles can each be successfully encapsulated in this manner, we next considered the preparation of multifunctional hybrid micelles containing both iron oxide nanoparticles and CdSe quantum dots. Centrifugal purification was applied to increase the fraction of loaded spherical micelles from 24 ± 6 % as prepared (Figure 2.6a) to 90 ± 2 % post-purification (Figure 2.6b), while wormlike micelles (Figure 2.6c) once again showed loading of essentially all micelles. While formation of multifunctional micelles thus requires a multi-step process (emulsification, solvent evaporation, and purification), we note that the complexity of the procedure is comparable to existing approaches to co-encapsulate nanoparticles.[9-11,15,32-34] Since bright-field TEM images do not allow for unambiguous discrimination of the different nanoparticle types, several additional experiments were undertaken to definitively establish successful co-encapsulation.

First, fluorescence images were collected as a permanent magnet was placed near suspensions of both spherical and wormlike micelles (movies available in the Supporting Information). As shown in Figure 2.6d-e for a wormlike micelle, motion of micelles along

the direction of increasing magnetic field strength was observed, clearly indicating the presence of both CdSe and iron oxide nanoparticles, and that the respective fluorescent and magnetic properties of the primary nanoparticles were retained in the composite micelle.

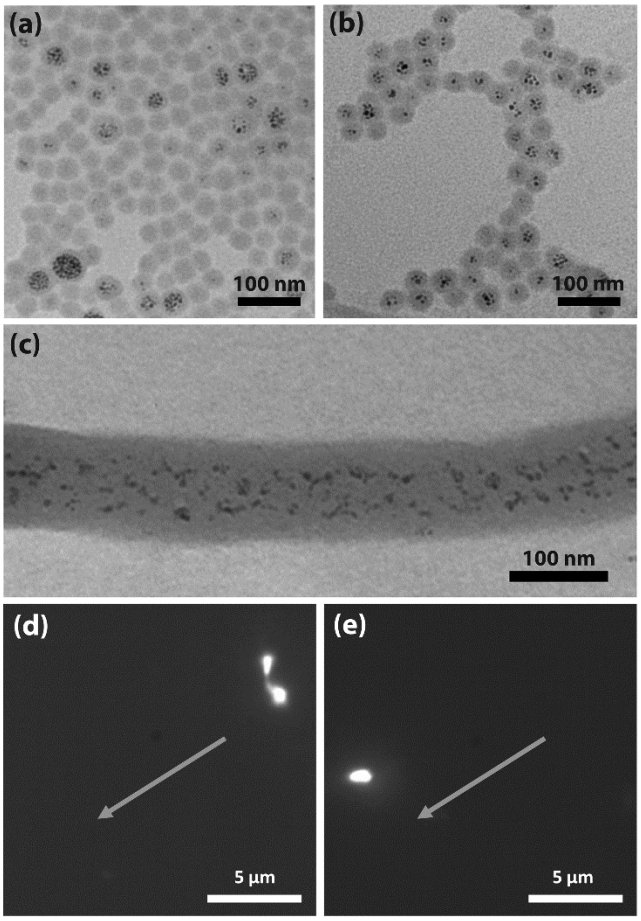

Figure 2.6 TEM images of spherical micelles of $PS_{9.5k}$-$PEO_{9.5k}$ with co-encapsulated iron oxide and CdSe nanoparticles: (a) before purification; (b) after purification by centrifugation, (c) wormlike micelles of PS_{19k}-$PEO_{6.4k}$ with co-encapsulated iron oxide and CdSe nanoparticles. Fluorescence images of a wormlike micelle of PS_{19k}-$PEO_{6.4k}$ with co-encapsulated iron oxide and CdSe nanoparticles (d) 0 and (e) 11 s after placing a permanent magnet beside the micelle suspension. The arrow denotes the direction of increasing magnetic field strength.

Next, we used a mixture of CdSe nanorods (3×18 nm) with either magnetic nanoparticles or Au nanoparticles, allowing the different types of nanoparticles to be distinguished by shape. As revealed by presence of both nanorods and nanoparticles within

single micelle cores in the TEM images in Figure 2.7a-d, co-encapsulation with high uniformity was achieved both for spherical and wormlike micelles. As shown in Figure 2.7a-b, purification of spherical micelles by centrifugation led to enrichment to over 90 % of nanoparticle-loaded micelles, with ~ 90 % of loaded micelles showing both nanorods and nanoparticles, while every wormlike micelle had both nanorods and nanoparticles.

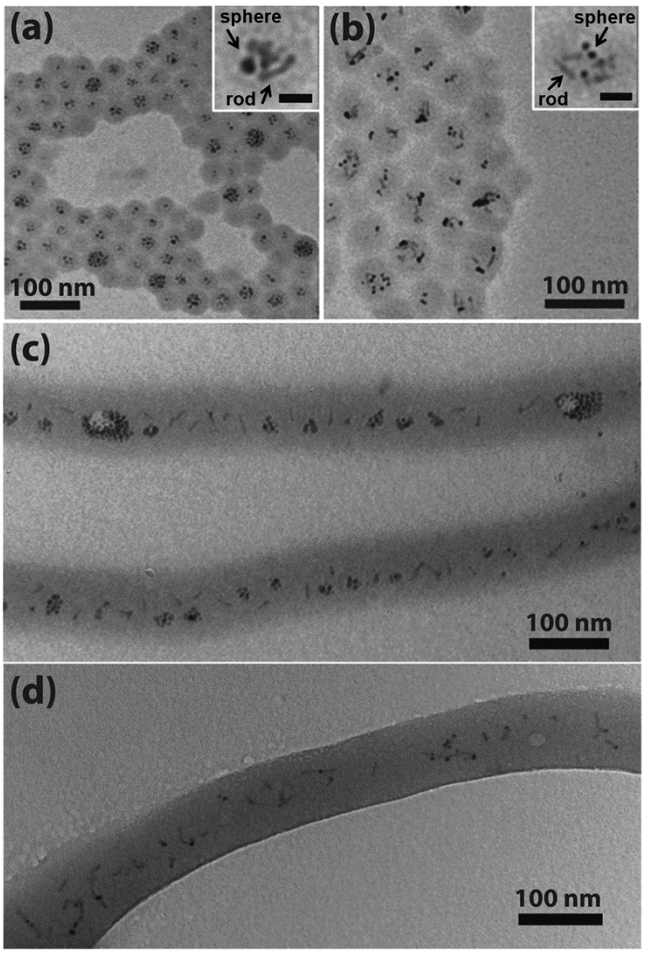

Figure 2.7 TEM images of purified spherical micelles of $PS_{9.5k}$-$PEO_{9.5k}$ with co-encapsulated (a) iron oxide nanoparticles and CdSe nanorods and (b) Au-DDT nanoparticles and CdSe nanorods. Inset: magnified images (scale bars, 20 nm). Wormlike micelles of PS_{19k}-$PEO_{6.4k}$ with co-encapsulated (c) iron oxide nanoparticles and CdSe nanorods and (d) Au-DDT nanoparticles and CdSe nanorods.

Finally, we performed analytical TEM measurements on multi-functional wormlike micelles, as summarized in Figure 2.8 While high-angle annular dark-field scanning transmission electron microscopy (HAADF-STEM) imaging (Figure 2.8a) provides clear contrast between nanoparticles and PS-PEO due to the large differences in atomic numbers, it was not straightforward to distinguish CdSe from iron oxide in this manner due to distributions in particle size and position relative to the microscope focal plane.[56, 57] Thus, we also employed energy dispersive X-ray spectroscopy (EDX) point scan measurements at different positions along the contour of a cylindrical micelle, as indicated in Figure 2.8 (a). The position marked (b) (corresponding to the EDX spectrum in Figure 2.8b) showed both Kα and Lα lines of iron, while position (c) (Figure 2.8c) showed the Lα peak of cadmium, indicating the presence of both particles in the same wormlike micelle. Similar results were also obtained for wormlike micelles containing both CdSe and Au nanoparticles (Figure 2.9).

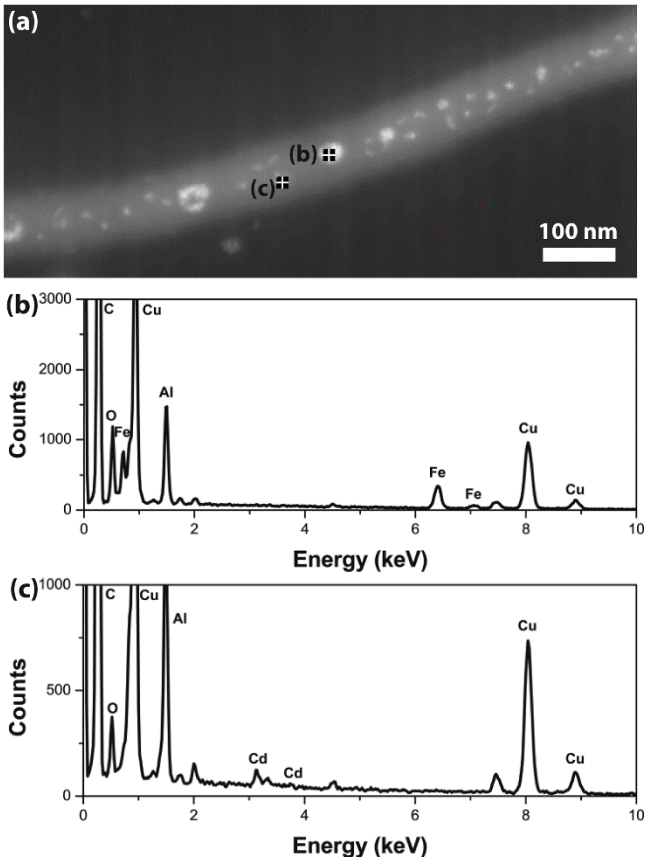

Figure 2.8 (a) HAADF-STEM image and (b-c) EDX point analyses of wormlike micelles of PS_{19k}-$PEO_{6.4k}$ with co-encapsulated iron oxide nanoparticles and CdSe nanorods. EDX spectra at points (b) and (c) indicate the presence of iron and cadmium, respectively.

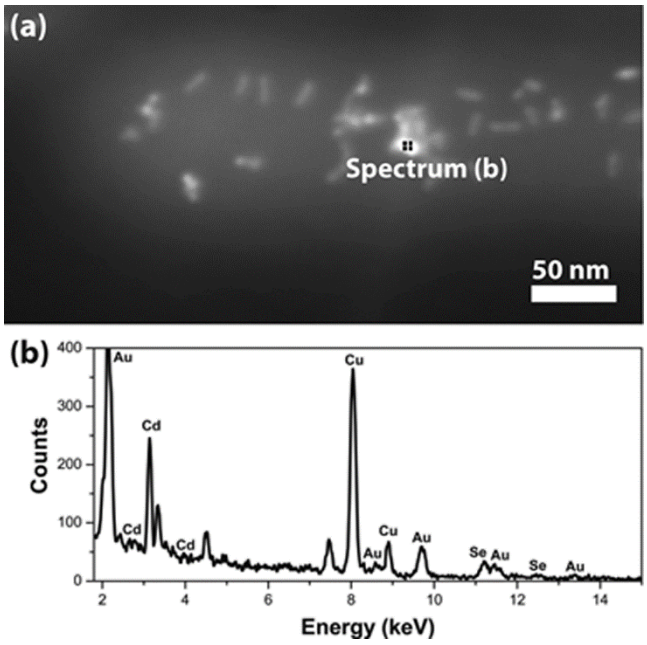

Figure 2.9 (a) HAADF-STEM image and (b) EDX point analysis of wormlike micelles of PS_{19k}-$PEO_{6.4k}$ with co-encapsulated Au-DDT nanoparticles and CdSe nanorods.

2.4 Conclusions

In conclusion, we have studied the formation of multifunctional hybrid spherical and wormlike micelles of PS-PEO block copolymers with several types of inorganic nanoparticles encapsulated in their PS cores. Emulsion processing, followed by evaporation-induced instabilities of the solvent droplet/water interfaces, was found to yield efficient encapsulation of pre-synthesized hydrophobic nanoparticles of iron oxide, CdSe, and Au, including co-encapsulation of different particle types. In all cases, particles coated with native alkane ligands were effectively encapsulated, thus the use of custom polymer-based ligands was not required. The simplicity and versatility of this method makes it a powerful route for the preparation of multifunctional polymer micelles, as we have

demonstrated through the first report of cylindrical micelles containing multiple types of hydrophobic nanoparticles.

2.5 References

1. Shi, W. L. *et al.* A general approach to binary and ternary hybrid nanocrystals. *Nano Lett.* **6**, 875-881 (2006).

2. Gu, H. W., Zheng, R. K., Zhang, X. X. & Xu, B. Facile one-pot synthesis of bifunctional heterodimers of nanoparticles: A conjugate of quantum dot and magnetic nanoparticles. *J. Am. Chem. Soc.* **126**, 5664-5665 (2004).

3. Yu, H., Chen, M., Rice, P. M., Wang, S. X., White, R. L. & Sun, S. H. Dumbbell-like bifunctional au-fe3o4 nanoparticles. *Nano Lett.* **5**, 379-382 (2005).

4. Khon, E. *et al.* Suppression of the plasmon resonance in au/cds colloidal nanocomposites. *Nano Lett.* **11**, 1792-1799 (2011).

5. Lopez-Lorente, A. I., Simonet, B. M. & Valcarcel, M. Analytical potential of hybrid nanoparticles. *Anal. Bioanal. Chem.* **399**, 43-54 (2011).

6. Sitt, A., Salant, A., Menagen, G. & Banin, U. Highly emissive nano rod-in-rod heterostructures with strong linear polarization. *Nano Lett.* **11**, 2054-2060 (2011).

7. Shevchenko, E. V. *et al.* Gold/iron oxide core/hollow-shell nanoparticles. *Adv Mater* **20**, 4323-4329 (2008).

8. Cozzoli, P. D., Pellegrino, T. & Manna, L. Synthesis, properties and perspectives of hybrid nanocrystal structures. *Chem. Soc. Rev.* **35**, 1195-1208 (2006).

9. Insin, N., Tracy, J. B., Lee, H., Zimmer, J. P., Westervelt, R. M. & Bawendi, M. G. Incorporation of iron oxide nanoplarticles and quantum dots into silica microspheres. *ACS Nano* **2**, 197-202 (2008).

10. Yi, D. K., Selvan, S. T., Lee, S. S., Papaefthymiou, G. C., Kundaliya, D. & Ying, J. Y. Silica-coated nanocomposites of magnetic nanoparticles and quantum dots. *J. Am. Chem. Soc.* **127**, 4990-4991 (2005).

11. Quarta, A., Di Corato, R., Manna, L., Ragusa, A. & Pellegrino, T. Fluorescent-magnetic hybrid nanostructures: Preparation, properties, and applications in biology. *Ieee T Nanobiosci* **6**, 298-308 (2007).

12. Shi, J. J., Votruba, A. R., Farokhzad, O. C. & Langer, R. Nanotechnology in drug delivery and tissue engineering: From discovery to applications. *Nano Lett.* **10**, 3223-3230 (2010).

13. Hammond, P. T. Virtual issue on nanomaterials for drug delivery. *ACS Nano* **5**, 681-684 (2011).

14. Ruan, G., Thakur, D., Deng, S., Hawkins, S. & Winter, J. O. Fluorescent-magnetic nanoparticles for imaging and cell manipulation. *Proc. Inst. Mech. Eng., Part N: J. Nanoengineering and Nanosystems* **223**, 81-86 (2010).

15. Park, J.-H., von Maltzahn, G., Ruoslahti, E., Bhatia, S. N. & Sailor, M. J. Micellar hybrid nanoparticles for simultaneous magnetofluorescent imaging and drug delivery. *Angew. Chem., Int. Ed.* **47**, 7284-7288 (2008).

16. Koo, H. *et al.* Nanoprobes for biomedical imaging in living systems. *Nano Today* **6**, 204-220 (2011).

17. Gu, Z., Biswas, A., Zhao, M. X. & Tang, Y. Tailoring nanocarriers for intracellular protein delivery. *Chem. Soc. Rev.* **40**, 3638-3655 (2011).

18. Jain, S. & Bates, F. S. On the origins of morphological complexity in block copolymer surfactants. *Science* **300**, 460-464 (2003).

19. Hayward, R. C. & Pochan, D. J. Tailored assemblies of block copolymers in solution: It is all about the process. *Macromolecules* **43**, 3577-3584 (2010).

20. Blanazs, A., Armes, S. P. & Ryan, A. J. Self-assembled block copolymer aggregates: From micelles to vesicles and their biological applications. *Macromol. Rapid Commun.* **30**, 267-277 (2009).

21. Gohy, J. F. Block copolymer micelles. *Block Copolymers Ii* **190**, 65-136 (2005).

22. Rodríguez-Hernández, J., Chécot, F., Gnanou, Y. & Lecommandoux, S. Toward 'smart' nano-objects by self-assembly of block copolymers in solution. *Prog. Polym. Sci.* **30**, 691-724 (2005).

23. Zhang, L., Liu, W. G., Lin, L., Chen, D. Y. & Stenze, M. H. Degradable disulfide core-cross-linked micelles as a drug delivery system prepared from vinyl functionalized nucleosides via the raft process. *Biomacromolecules* **9**, 3321-3331 (2008).

24. Li, W. *et al.* The fine-tuning of thermosensitive and degradable polymer micelles for enhancing intracellular uptake and drug release in tumors. *Biomaterials* **32**, 3832-3844 (2011).

25. Huang, W. *et al.* Glycyrrhetinic acid-functionalized degradable micelles as liver-targeted drug carrier. *J. Mater. Sci.: Mater. Med.* **22**, 853-863 (2011).

26. Hruby, M. *et al.* Thermoresponsive, hydrolytically degradable polymer micelles intended for radionuclide delivery. *Macromol. Biosci.* **9**, 1016-1027 (2009).

27. Fuks, G., Talom, R. M. & Gauffre, F. Biohybrid block copolymers: Towards functional micelles and vesicles. *Chem. Soc. Rev.* **40**, 2475-2493 (2011).

28. O'Reilly, R. K., Hawker, C. J. & Wooley, K. L. Cross-linked block copolymer micelles: Functional nanostructures of great potential and versatility. *Chem. Soc. Rev.* **35**, 1068-1083 (2006).

29. Bae, Y. & Kataoka, K. Intelligent polymeric micelles from functional poly(ethylene glycol)-poly(amino acid) block copolymers. *Adv. Drug Deliv. Rev.* **61**, 768-784 (2009).

30. Stenzel, M. H. Raft polymerization: An avenue to functional polymeric micelles for drug delivery. *Chem Commun*, 3486-3503 (2008).

31. Sudeep, P. K. & Emrick, T. Pearls of wisdom: Stringing nanoparticles and polymers into new assemblies and materials. *ACS Nano* **3**, 2870-2875 (2009).

32. Kamps, A. C., Sanchez-Gaytan, B. L., Hickey, R. J., Clarke, N., Fryd, M. & Park, S. J. Nanoparticle-directed self-assembly of amphiphilic block copolymers. *Langmuir* **26**, 14345-14350 (2010).

33. Kim, B.-S. & Taton, T. A. Multicomponent nanoparticles via self-assembly with cross-linked block copolymer surfactants. *Langmuir* **23**, 2198-2202 (2007).

34. Di Corato, R. *et al.* Multifunctional nanobeads based on quantum dots and magnetic nanoparticles: Synthesis and cancer cell targeting and sorting. *ACS Nano* **5**, 1109-1121 (2011).

35. Geng, Y. *et al.* Shape effects of filaments versus spherical particles in flow and drug delivery. *Nat. Nanotechnol.* **2**, 249-255 (2007).

36. Nishiyama, N. Nanomedicine - nanocarriers shape up for long life. *Nat. Nanotechnol.* **2**, 203-204 (2007).

37. Cai, S. S., Vijayan, K., Cheng, D., Lima, E. M. & Discher, D. E. Micelles of different morphologies - advantages of worm-like filomicelles of peo-pcl in paclitaxel delivery. *Pharm. Res.* **24**, 2099-2109 (2007).

38. Wang, X. S., Wang, H., Coombs, N., Winnik, M. A. & Manners, I. Redox-induced synthesis and encapsulation of metal nanoparticles in shell-cross-linked organometallic nanotubes. *J. Am. Chem. Soc.* **127**, 8924-8925 (2005).

39. Wang, H., Wang, X. S., Winnik, M. A. & Manners, I. Redox-mediated synthesis and encapsulation of inorganic nanoparticles in shell-cross-linked cylindrical polyferrocenylsilane block copolymer micelles. *J. Am. Chem. Soc.* **130**, 12921-12930 (2008).

40. Djalali, R., Li, S. Y. & Schmidt, M. Amphipolar core-shell cylindrical brushes as templates for the formation of gold clusters and nanowires. *Macromolecules* **35**, 4282-4288 (2002).

41. Walther, A., Yuan, J., Abetz, V. & Muller, A. H. E. Structure-tunable bidirectional hybrid nanowires via multicompartment cylinders. *Nano Lett.* **9**, 2026-2030 (2009).

42. Zhang, M. *et al.* Preparation and photo/chemical-activation of wormlike network micelles of core-shell quantum dots and block copolymer hybrids. *J. Mater. Chem.* **21**, 9692-9701 (2011).

43. Zhang, M. *et al.* Sphere-to-wormlike network transition of block copolymer micelles containing cdse quantum dots in the corona. *Macromolecules* **43**, 5066-5074 (2010).

44. Wang, M. F. *et al.* Self-assembly of colloidal quantum dots on the scaffold of triblock copolymer micelles. *ACS Appl. Mater. Interfaces* **2**, 3160-3169 (2010).

45. Li, W., Liu, S., Deng, R. & Zhu, J. Encapsulation of nanoparticles in block copolymer micellar aggregates by directed supramolecular assembly. *Angew. Chem., Int. Ed.* **50**, 5865-5868 (2011).

46. Mai, Y. Y. & Eisenberg, A. Controlled incorporation of particles into the central portion of block copolymer rods and micelles. *Macromolecules* **44**, 3179-3183 (2011).

47. Zhu, J. T. & Hayward, R. C. Spontaneous generation of amphiphilic block copolymer micelles with multiple morphologies through interfacial instabilities. *J. Am. Chem. Soc.* **130**, 7496-7502 (2008).

48. Ruan, G. *et al.* Simultaneous magnetic manipulation and fluorescent tracking of multiple individual hybrid nanostructures. *Nano Lett.* **10**, 2220-2224 (2010).

49. Ruan, G. & Winter, J. O. Alternating-color quantum dot nanocomposites for particle tracking. *Nano Lett.* **11**, 941-945 (2011).

50. Sun, S. H. *et al.* Monodisperse mfe2o4 (m = fe, co, mn) nanoparticles. *J. Am. Chem. Soc.* **126**, 273-279 (2004).

51. Peng, X. G. & Peng, Z. A. Formation of high-quality cdte, cdse, and cds nanocrystals using cdo as precursor. *J. Am. Chem. Soc.* **123**, 183-184 (2001).

52. Jana, N. R., Gearheart, L. & Murphy, C. J. Seeding growth for size control of 5-40 nm diameter gold nanoparticles. *Langmuir* **17**, 6782-6786 (2001).

53. Peng, Z. A. & Peng, X. G. Nearly monodisperse and shape-controlled cdse nanocrystals via alternative routes: Nucleation and growth. *J. Am. Chem. Soc.* **124**, 3343-3353 (2002).

54. Garamszegi, L., Donzel, C., Carrot, G., Nguyen, T. Q. & Hilborn, J. Synthesis of thiol end-functional polystyrene via atom transfer radical polymerization. *React. Funct. Polym.* **55**, 179-183 (2003).

55. Mark, J. E. *Physical properties of polymers handbook*. Springer (2007).

56. Browning, N. D., Chisholm, M. F. & Pennycook, S. J. Atomic-resolution chemical-analysis using a scanning-transmission electron-microscope. *Nature* **366**, 143-146 (1993).

57. Li, Z. Y., Yuan, J., Chen, Y., Palmer, R. E. & Wilcoxon, J. P. Local three-dimensional visualization of nanoparticle assemblies. *Adv Mater* **17**, 2885-2888 (2005).

CHAPTER 3

OSMOTICALLY-DRIVEN FORMATION OF DOUBLE EMULSIONS STABILIZED BY AMPHIPHILIC BLOCK COPOLYMERS[†]

3.1 Introduction

Double emulsions consisting of water-in-oil-in-water (w/o/w) or oil-in-water-in-oil (o/w/o) droplets are of significant interest for pharmaceuticals,[1-6] cosmetics,[7, 8] separation technologies,[9] and microreactors.[10-12] Most commonly, double emulsions are formed through a two-step emulsification process using a combination of oil-soluble and water-soluble surfactants to stabilize the o/w and w/o interfaces, respectively. However, this approach generally yields a broad distribution of droplet sizes, and the second emulsification step introduces the possibility of destabilization through rupturing of the inner droplets.[13-19] Very recently, Hong et al.[20] and Besnard et al.[21] have reported one-step methods for the preparation of double emulsions stabilized by amphiphilic block copolymers as a result of phase inversion processes. However, control over the structures of double emulsions obtained via one-step processes remains challenging. Alternatively, the use of microfluidic techniques enables precise control over droplet size and number at each level within multiple emulsions, but the throughput of these methods is low.[22-26]

For w/o/w emulsions in particular, osmotic pressure differences between the inner and

[†] Reproduced and modified with permission from J. Bae, T. P. Russell, and R. C. Hayward, "Osmotically-driven formation of double emulsions stabilized by amphiphilic block copolymers", *Angewandte Chemie International Edition,* **53**, 8240-8245 (2014).

outer aqueous phases have played a central role in efforts to control droplet stability.[15, 16, 27-34] In particular, the addition of osmolytes to the internal phase is commonly used to prevent instability due to transport of water to the external phase driven by differences in Laplace pressure (i.e., Ostwald ripening). However, such osmotically-stabilized double emulsions have previously been prepared only by two-step processes because the inner water droplets must contain a different concentration of water-soluble species than the continuous phase.

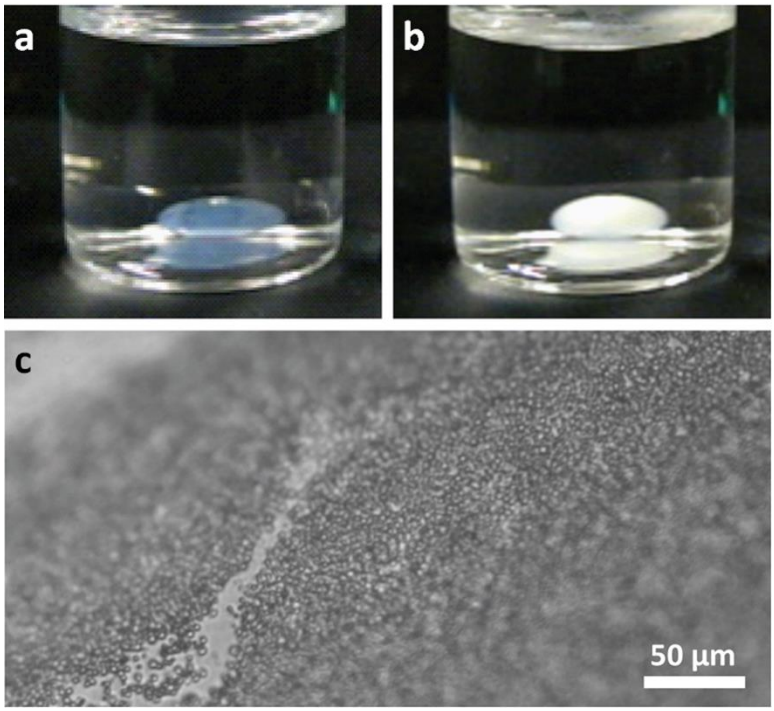

Figure 3.1 Photographs taken (a) 15 s and (b) 25 min after placing a large drop of chloroform containing 10 mg/mL of as received PS-PNIPAM into deionized water. (c) Optical micrograph of the µm-scale w/o emulsion droplets spontaneously formed at the macroscopic o/w interface, which account for the clouding seen from (a)-(b).

In this chapter, we introduce a new single step method that takes advantage of osmotic pressure differences to yield formation of highly stable w/o/w double emulsions with tailored inner droplet characteristics. Our approach is inspired by the observation that

an organic solvent containing amphiphilic block copolymers placed in contact with water will often spontaneously develop a cloudy appearance, for example as shown in Figure 3.1 for polystyrene-block-poly(*N*-isopropylacrylamide) (PS-PNIPAM) diblock copolymers dissolved in chloroform (see also Supporting Information Movie 1). As revealed by optical microscopy, the cloudiness arises from the spontaneous formation of micrometer-sized water droplets within the solvent phase near the interface with water. In this case, the droplets show a fairly narrow size distribution with an average diameter of 2.8 μm and standard deviation of 0.4 μm. This phenomenon has been described several times previously,[35-37] but its origin is not well understood. Indeed, the spontaneous transport of water from the bulk into micrometer-sized droplets, which experience a Laplace pressure of ~ 10 kPa due to the solvent/water interfacial tension, seems at first to contradict basic thermodynamic principles. However, we hypothesized that droplet formation was driven by water-soluble impurities present in the copolymer that would be preferentially solvated in the forming droplets, thus providing an osmotic driving force to counterbalance Laplace pressure. Specifically, we suspected this behavior to arise from residual salt species originating from the organometallic initiators used in polymer synthesis, which have previously been shown to play an important role in facilitating electric-field alignment within block copolymer thin films.[38-40]

3.2 Experimental

3.2.1 Materials and methods

Large-scale solvent/water interfaces were formed by adding 200 µL of chloroform containing 10 mg/mL of PS-PNIPAM into 10 mL of deionized water in a 20 mL vial. Formation of primary solvent-in-water emulsions with ~ 10 – 100 µm scale droplets was accomplished by adding the solvent phase (chloroform containing 10 mg/mL PS-PNIPAM, or toluene containing 10 mg/mL PS-PEO; with different salt concentrations) to the aqueous phase (deionized water containing 5mg/mL poly(vinyl alcohol); M_w=13-23 kg/mol, 87-89 % hydrolyzed) in a 1:5 volumetric ratio and gently shaking by hand. After emulsification, a 5 to 10 fold excess of deionized water was added. In the case of adding salts to chloroform solution containing PS-PNIPAM, the solution was stirred continuously for 1-2 d. Experiments were conducted with PS-PNIPAM diblock copolymer (M_n = 16 kg/mol – 5.2 kg/mol) and two PS-PEO diblock copolymers (M_n = 9.5 kg/mol - 9.5 kg/mol and 9.5 kg/mol – 18 kg/mol) purchased from Polymer Source Inc. For fluorescent labeling, 0.1 mg/mL of Nile red or FITC-Dextran (M_w= 10 kg/mol) were included in the block copolymer solution. All chemicals were obtained from Aldrich and used without purification, except where noted.

Purification of PS_{16k}-$PNIPAM_{5.2k}$ was conducted by dissolving the as-received sample in dichloromethane (DCM) at 100 mg/mL, and adding the solution (total volume: 2 mL) dropwise over 30 min into 250 mL of methanol with stirring. The re-precipitated polymer was filtered and dried in a vacuum oven. Purification of $PS_{9.5k}$-$PEO_{9.5k}$ was carried out by forming micelles in aqueous solution using the interfacial instability route described

previously.[41] Micelles were separated by centrifugation at 14 krpm for 15 min, after which the upper ~ 80 % of solution was discarded and the same volume of deionized water added. This process was repeated 5 times, and the sample subsequently lyophilized to recover dry polymer.

Porous PS-PNIPAM films prepared by drop casting of chloroform solution containing 10 mg/mL of as received and purified PS-PNIPAM, respectively, on pre-cleaned Si substrates under ambient conditions (temperature ~ 20 ºC, relative humidity ~ 35 %) for 1 d.

3.2.2 Digestion of polymer samples for ICP-MS analysis

0.5 mL of nitric acid (70 % HNO_3, for trace metal analysis; BDH Chemicals) was added to polymer samples (25-100 mg) in a Teflon tube, which was placed in an oil bath at 50 °C with continuous stirring (250 rpm) for 1-2 d in an acid fume hood. (*Caution*: Do not leave digestion unattended for the first 20 min. If the sample is overflowing, the digestion temperature may need to be decreased.) Following complete digestion of the polymer, the solution was cooled to room temperature, followed by careful addition of hydrogen peroxide solution (30 % H_2O_2, for trace analysis; Fluka Analytical) in ~ 0.5 mL increments followed by stirring for 3-12 h until no further CO_2 gas bubble formation was observed. This digested solution was next centrifuged at 3800 rpm for 30 min, and the supernatant was collected in a Teflon tube. The absence of carbon in this clean supernatant was confirmed by adding 2 mL of 30 % H_2O_2. Next, the solution was filtered using a 0.2 μm pore size Teflon filter and diluted by adding 18 MΩ water to reach an HNO_3

concentration of 2 %. Multi-element calibration standard 3 (PerkinElmer, Inc.) containing known concentrations of lithium (Li) and potassium (K) was used for calibration.

3.2.3 Characterization

Micrographs and movies of osmotically-driven emulsification were taken using a digital camera (PowerShot A640, Canon) on the macro-scale and a Zeiss Axiovert 200 inverted optical microscope with 10x and 20x objectives and QImaging camera (Retiga-2000R Fast 1394 Mono Cooled) on the micro-scale. Fluorescence images were obtained using a 100x oil-immersion objective. An FEI Magellan 400 FESEM was used at 5 kV accelerating voltage and 30 pA beam current to image porous PS-PNIPAM films which were coated by a thin layer of carbon. Inductively coupled plasma mass spectrometry (ICP-MS) (ELAN-DRC-e, PerkinElmer SCIEX) was used to analyze the concentrations of lithium and potassium elements in diblock copolymer samples. The presence of salt aggregates in chloroform containing 10 mg/mL of as received and purified PS- PNIPAM, respectively, was observed by drop casting solutions on TEM grids coated with a carbon film, and performing bright field TEM on unstained samples using a JEOL 2000FX electron microscope operated at an accelerating voltage of 200 kV. The size distribution of salt aggregates were analysed by DLS (Malvern Zetasizer Zen 3600, Malvern Instruments) using chloroform containing 1 mg/mL of as received PS-PNIPAM with a 90º scattering angle at 25 ºC.

3.3 Results and discussion

3.3.1 Mechanism of Osmotically-Driven Emulsification

We first verified the presence of impurities remaining from the organo-lithium and organo-potassium initiator species using inductively coupled plasma mass spectrometry (ICP-MS) to characterize three commercial amphiphilic block copolymers (Table 3.1): PS_{16k}-$PNIPAM_{5.2k}$ and two polystyrene-block-poly(ethylene oxide) samples ($PS_{9.5k}$-$PEO_{9.5k}$ and $PS_{9.5k}$-PEO_{18k}). As received, PS_{16k}-$PNIPAM_{5.2k}$ contained 0.162 Li^+ species per polymer chain, while $PS_{9.5k}$-$PEO_{9.5k}$ contained 0.112 K^+ species per chain; following purification steps described in the Experimental section, these values were reduced to 0.0212 and 0.003, respectively. (We report concentrations on a per-chain basis, since one initiator salt species per chain would be present following synthesis in the absence of any purification.) Interestingly, the as-received sample of $PS_{9.5k}$-PEO_{18k} contained less than 0.01 K^+ per chain, and thus no additional purification was conducted.

Table 3.1 Salt impurity content for three commercial amphiphilic block copolymers as received, and after purification, as measured by ICP-MS analysis.

Cations/polymer chain	As received	Purified
Li^+ / PS_{16k}-$PNIPAM_{5.2k}$	0.162 ± 0.002	0.0212 ± 0.0004
K^+ / $PS_{9.5k}$-$PEO_{9.5k}$	0.112 ± 0.003	0.003 ± 0.001
K^+ / $PS_{9.5k}$-PEO_{18k}	0.0089 ± 0.0005	–

As the solubilities of lithium and potassium salts in the organic solvents considered here are quite low, their presence in solution must be facilitated by the block copolymer. Indeed, transmission electron microscope (TEM) images of as-received PS-PNIPAM samples cast from chloroform solution revealed domains of 20 – 80 nm in diameter (Figure 3.2a). Coupled with dynamic light scattering (DLS) measurements indicating the existence of objects with average hydrodynamic diameters of ~ 100 nm in solution (Figure 3.2b), these results suggest that the salts exist in solution as block-copolymer-stabilized aggregates. Following purification to remove lithium salts, PS-PNIPAM solutions showed no signs of such aggregates (Figure 3.3), consistent with the good solubility of both polymer blocks in chloroform.

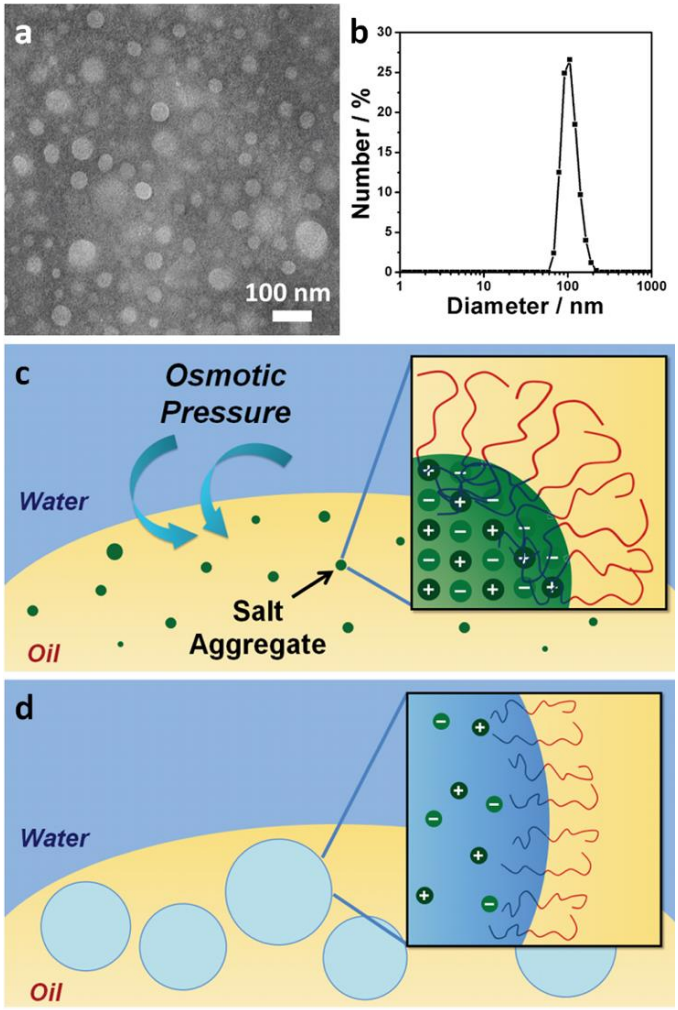

Figure 3.2 (a) TEM image and (b) hydrodynamic diameter distribution from DLS of salt aggregates dispersed in the organic solution (chloroform containing 10 mg/mL of as received PS-PNIPAM). Schematic illustration of the spontaneous formation of water droplets at an o/w droplet interface: (c) water is pulled into the oil phase due to the presence of salt-aggregates, (d) leading to osmotically-driven formation of a w/o/w double emulsion.

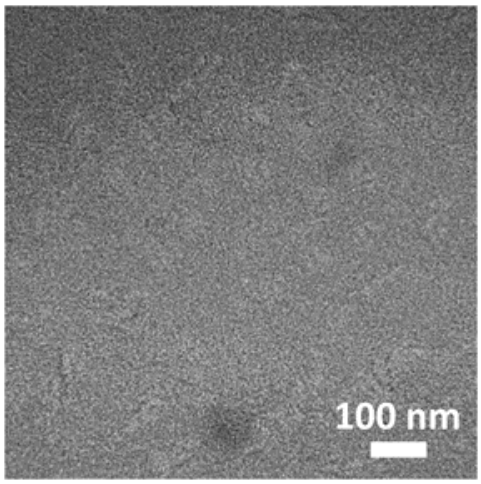

Figure 3.3 TEM image of a film cast from a 10 mg/mL solution of purified PS-PNIPAM in chloroform. No evidence is observed of the ~ 20 – 80 nm aggregates seen for as-received PS-PNIPAM (Figure 3.2a).

We suggest that these salts provide an osmotic driving force that exceeds the Laplace pressure associated with the oil/water interface, thereby drawing water out of the surrounding bulk phase and into the spontaneously forming droplets (Figure 3.2c-d). Specifically, after the organic phase is brought into contact with water, the salt aggregates grow in size due to the inflow of water until they reach a final size R_{eq} where the osmotic pressure and Laplace pressure balance. Without the large osmotic driving force provided by the salt species, one might expect the presence of inverse block copolymer micelles that could be swollen by water until a maximum size that is dictated by the characteristics of the copolymer, typically ~ 100 nm or below.[42, 43] Here, the presence of salt causes expansion into macro-emulsion droplets with micrometer-scale sizes dictated by the balance between osmotic stress and interfacial tension.

While the initial formation of droplets near the interface can be seen within ~ 1 s, since the process relies on diffusion of water through chloroform, the time required for

each aggregate to ‘inflate’ into an emulsion droplet of size R_{eq} will depend on the overall dimensions of the organic phase. For example, in Figure 3.1, the formation of internal droplets within a macroscopic chloroform phase with dimensions of several mm requires ~ 25 min to reach completion. Notably, since the forming droplets are less dense than the surrounding organic solvent, they will float upwards, which also provides some convective mixing. Due to the presence of the amphiphilic block copolymer that can continually adsorb to the solvent/water interface during growth, the resulting droplets are highly stable against coalescence. Indeed, we have not observed any coalescence between spontaneously formed droplets or with the external water phase. Based on this stability, we propose that each salt aggregate within the organic phase gives rise to a single emulsion droplet, such that the final details of the osmotically formed emulsions are not sensitive to these kinetics, but instead only to the initial characteristics of the salt aggregates. Here, we neglect the possibility for the salt species to diffuse out of the droplets and into the continuous phase, although for species showing more pronounced solubility in the organic phase, the relative rates of salt and water transport would be an important consideration.

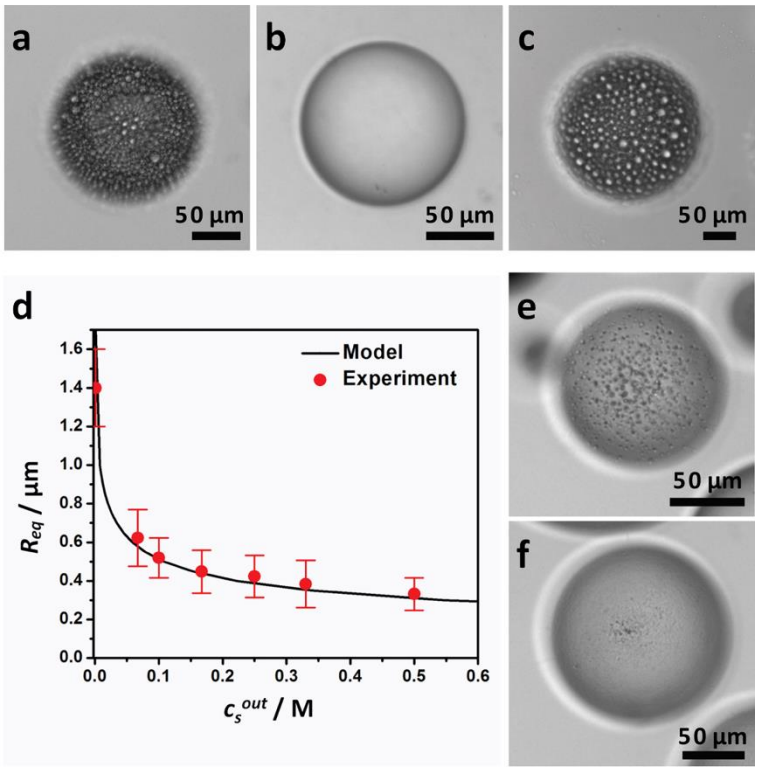

Figure 3.4 Optical micrographs of primary o/w emulsion droplets, where the continuous phase is 5 mg/mL PVOH in deionized water and the droplet phase is chloroform containing: (a) 10 mg/mL of as-received PS-PNIPAM (b) 10 mg/mL of purified PS-PNIPAM, and (c) 10 mg/mL of purified PS-PNIPAM with 4.2 mg/mL LiCl. (d) Measured equilibrium radius (R_{eq}) of secondary w/o emulsions of chloroform containing 10 mg/mL of as-received PS-PNIPAM with different salt concentration of the continuous phase (c_s^{out}) (gray circles), and the calculated values (black line). Optical micrographs of the deflation of w/o secondary emulsion droplets formed using chloroform containing 10 mg/mL of as-received PS-PNIPAM as the oil phase and deionized water containing 5 mg/ml PVOH with c_s^{out} = (e) 0.17 M and (f) 0.5 M LiCl.

The Laplace pressure difference (ΔP) between the interior of a droplet of radius R and the external phase resulting from the solvent/water interfacial tension (γ) is given by $\Delta P = 2\gamma / R$, where we have ignored the pressure drop across the outer droplet surface due to the relatively small curvature of this interface.[27] Approximating the osmotic pressure Π in the fully inflated droplet as that for a dilute deal solution with a concentration c_s of monovalent salt, $\Pi = 2c_s k_B T$, yields an equilibrium condition of

$$\Delta P = \frac{2\gamma}{R_{eq}} - \frac{2n_s k_B T}{(4\pi/3)R_{eq}^{\ 3}} \approx 0 \qquad (1)$$

where n_s is the number of salt molecules in the initial aggregate, which we assume remains constant during osmotic inflation of a water droplet. Using pendent drop tensiometry, we measured the interfacial tension of a chloroform solution containing 10 mg/mL of purified PS-PNIPAM as γ = 19.4 ± 0.9 mN/m. Thus, for the observed droplet sizes of R_{eq} = 1.4 μm, Equation (1) indicates a value of n_s = 6.5 x 10^{-17} mole. This value is in reasonably good agreement with the measured aggregate sizes; while the exact nature of the salt is unknown, if we take them to be crystals of LiOH, the value of D_h ~ 100 nm from DLS (Figure 3.2b) yields n_s = 3.2 x 10^{-17} mole.

Further support for the proposed mechanism is provided by a series of experiments using purified copolymers. In this case, we prepared primary o/w emulsions with droplet sizes of ~ 100 μm by agitation of copolymer solutions in chloroform with a water phase containing 5 mg/mL of poly(vinyl alcohol). For as-received PS-PNIPAM, secondary water droplets with diameters of 2 – 3 μm formed near the primary o/w emulsion interface within a few seconds, as seen in Figure 3.4a. In contrast, purified PS-PNIPAM showed no evidence of secondary emulsion formation (Figure 3.4b). Finally, the addition of 4.2 mg/mL LiCl to the chloroform solution of PS-PNIPAM caused the spontaneous formation of double emulsions to be recovered with similar secondary droplet size (R_{eq} = 1.4 ± 0.8 μm) as seen in Figure 3.4c.

Similar behaviors were also found for toluene solutions of the two PS-PEO copolymers described in Table 3.1. As-received $PS_{9.5k}$-$PEO_{9.5k}$ showed spontaneous

formation of secondary w/o/w droplets, while the purified polymer did not (Figure 3.5a-b). Again, the behavior could be recovered by the addition of 7.5 µg/mL KCl to the block copolymer solution (Figure 3.5c). In the case of as-received $PS_{9.5k}$-PEO_{18k}, no spontaneous formation of emulsions was observed, consistent with the much lower salt concentration in the sample. However, the addition of 7.5 µg/mL or 7.5 mg/mL KCl to the solvent phase leads to self-emulsification. (Figure 3.5d-f).

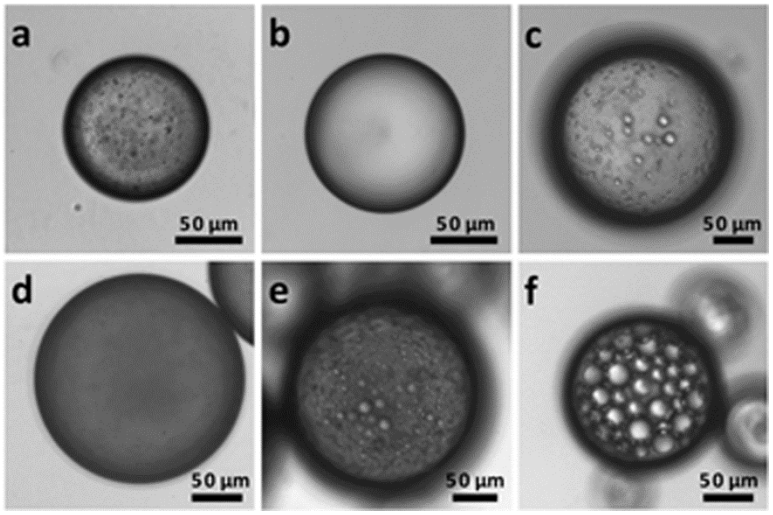

Figure 3.5 Optical micrographs of o/w emulsions, where the aqueous phase is deionized water containing 5 mg/mL PVOH and the oil phase is toluene containing 10 mg/mL of copolymer: (a) as-received $PS_{9.5k}$-$PEO_{9.5k}$, (b) purified $PS_{9.5k}$-$PEO_{9.5k}$, (c) purified $PS_{9.5k}$-$PEO_{9.5k}$ and 7.5 µg/mL KCl (d) as-received $PS_{9.5k}$-PEO_{18k}, (e) as-received $PS_{9.5k}$-PEO_{18k} and 7.5 µg/mL KCl, (f) as-received $PS_{9.5k}$-PEO_{18k} and 7.5 mg/mL KCl.

3.3.2 Osmotic-tailoring of amphiphilic copolymer assemblies

For osmotically-driven transport of water from the bulk aqueous phase into droplets, the salt concentration of the continuous phase c_s^{out} should provide a means to modulate the formation of spontaneously formed droplets. Treating the external phase as a dilute ideal

solution, the pressure balance in Eq (1) is modified as $\Delta P = 2\gamma/R_{eq} - [2n_s k_B T/(4\pi R_{eq}^3/3)] + 2c_s^{out} k_B T \approx 0$. To test this simple model, as-received PS-PNIPAM in chloroform was first emulsified in a salt-free aqueous phase, then LiCl was added to the outer phase to osmotically 'deflate' the spontaneously formed droplets (Supporting Information Movie 2). As shown in Fig. 3c-f, a progressive decrease in final droplet size with c_s^{out} was found, with the measured dependence of R_{eq} matching very closely the prediction of the model (Figure 3.4d).

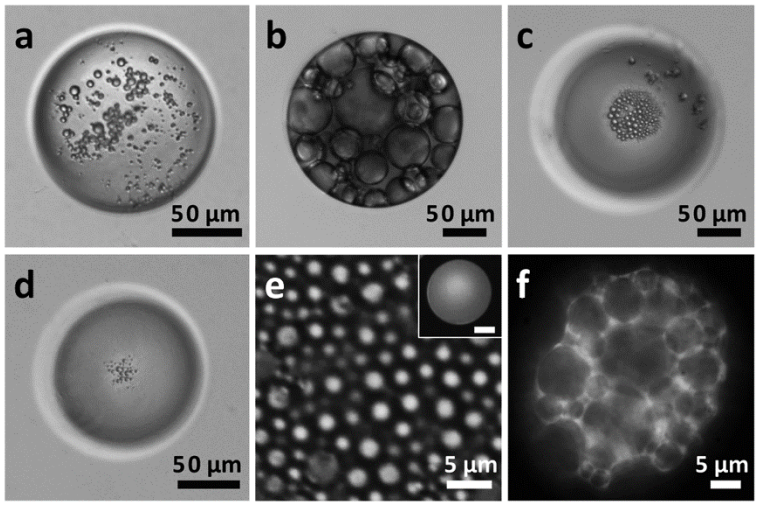

Figure 3.6 Optical micrographs of primary o/w emulsion droplets; chloroform containing (a) 10 mg/mL of purified PS-PNIPAM with 4.2 µg/mL LiCl, and (b) 10 mg/mL of as-received PS-PNIPAM with 42 mg/mL LiCl as the oil phase, and deionized water containing 5 mg/mL PVOH as the aqueous phase. Optical micrographs of w/o secondary emulsion droplets formed using chloroform with 10 mg/mL of as-received PS-PNIPAM and 42 mg/mL LiCl as the oil phase and water containing 5 mg/mL PVOH and c_s^{out} = (c) 1 M and (d) 7.5 M LiCl. (e) High magnification and (inset; scale bar: 50 µm) low magnification fluorescence micrographs showing that FITC-dextran (added at 0.1 mg/mL to a 10 mg/mL solution of as-received PS-PNIPAM in chloroform) is successfully encapsulated within internal water droplets. (f) Fluorescence micrograph of a multi-compartment polymer capsule formed by evaporation of organic solvent from w/o/w double emulsions prepared using 10 mg/mL of as-received PS-PNIPAM and 0.1 mg/mL of the hydrophobic fluorophore Nile red in chloroform as the oil phase.

We next demonstrate how osmotically-driven emulsification can be used to tailor the characteristics of internal compartments within w/o/w double emulsions and polymer capsules. When increasing amounts of LiCl were added to a chloroform solution containing PS-PNIPAM, the resulting secondary water droplets were found to have a larger size. For example, the addition of 4.2 μg/mL of LiCl to purified PS-PNIPAM induced formation of secondary water droplets with R_{eq} = 0.8 ± 0.4 μm (Figure 3.6a), while the addition of 42 mg/mL LiCl to as-received PS-PNIPAM yielded R_{eq} = 19.6 ± 7.6 μm (Figure 3.6b). This indicates that higher salt concentrations in the organic phase lead to the formation of larger salt aggregates (i.e., with greater values n_s). However, variations in c_s^{out} provide a further means to control the size of inner water droplets, at essentially constant number density. For the case of 42 mg/mL LiCl added to as-received PS-PNIPAM, increasing c_s^{out} to 1 and 7.5 M LiCl led to respective reductions in R_{eq} to 1.5 and 0.8 μm (Figure 3.6c-d and Figure 3.7). Together, variations in the amount of salt included in the organic and aqueous phases therefore provide a means to fine-tune the average size of the resulting secondary water droplets. Better control over the size, and size distribution, of the salt aggregates present in the organic phase would allow for even more precise control over double emulsion characteristics.

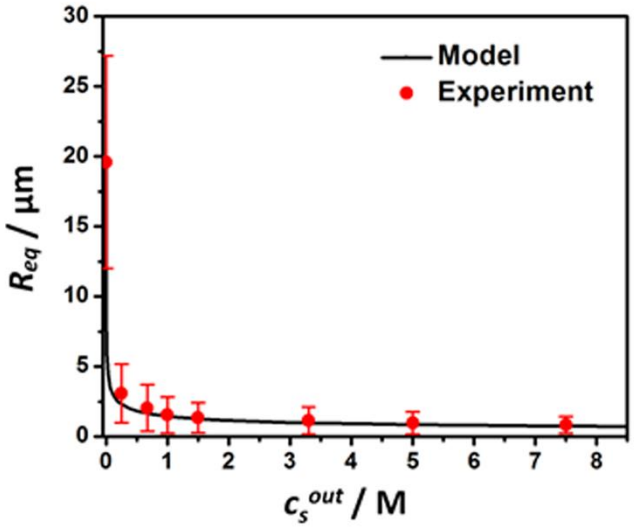

Figure 3.7 Measured equilibrium radius (R_{eq}) of secondary w/o emulsions formed with chloroform containing 10 mg/mL of as-received PS-PNIPAM and 42 mg/mL LiCl as the oil phase, and deionized water containing 5 mg/mL PVOH with different salt concentrations (c_s^{out}) as the aqueous phase, along with the dependence predicted by the simple model for osmotic emulsification (black line).

Notably, this self-emulsification approach allows for the encapsulation of water-soluble ingredients within the inner aqueous phases of w/o/w double emulsions. To demonstrate this capability, we added 0.1 mg/mL of dextran labeled with fluorescein isothiocyanate (FITC-dextran) to chloroform solutions of as-received PS-PNIPAM. The resulting double emulsions showed bright fluorescence within the internal water droplets (Figure 3.6e), and negligible fluorescence of the external aqueous phase (Figure 3.6e, inset), confirming the highly selective encapsulation of FITC-dextran within the inner emulsion droplets. Furthermore, the excellent stability of the double emulsions formed in this manner against both coalescence and Ostwald ripening allows them to be easily converted to amphiphilic block copolymer capsules by evaporation of the organic solvent, for example the multi-compartment structures shown in Figure 3.6f (see also Figure 3.8). These finding

suggest a straightforward means to prepare polymeric capsules containing hydrophilic and lipophilic species with control over the size and number of internal compartments by osmotically tuning the value of R_{eq} of the secondary w/o emulsions, and controlling the size of the primary o/w emulsions, respectively.

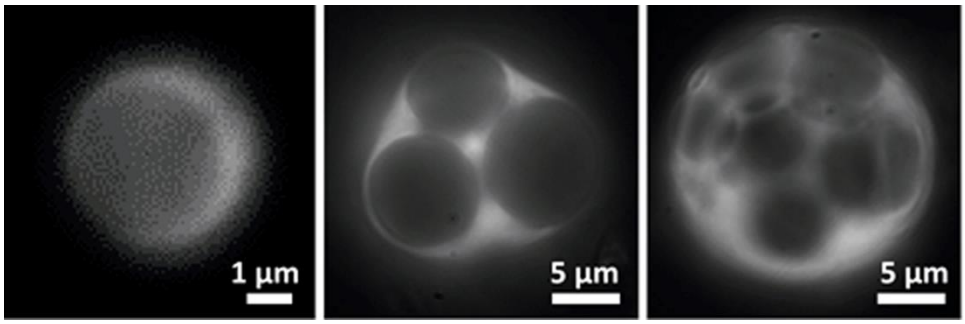

Figure 3.8 Fluorescence micrographs of single-, triple- and multi-compartment polymer capsules formed by evaporation of organic solvent from w/o/w double emulsions with different primary o/w emulsion drop sizes; chloroform containing 10 mg/mL of as-received PS-PNIPAM as the oil phase and deionized water containing 5 mg/mL PVOH as the aqueous phase were employed. Nile red was included in the organic phase to indicate the location of the hydrophobic capsule walls.

In addition to formation of controlled double emulsions and capsules, osmotically-driven uptake of water by block copolymer solutions offers opportunities for fabrication of hierarchically porous polymer films. Specifically, we consider the "breath figure" method, which has been widely used to make porous films of interest for applications in electronics, photonics, biotechnology, catalysis, and separations.[44-47] We find that chloroform solutions of purified PS-PNIPAM copolymers yield conventional breath figure structures, with a single and fairly uniform pore size (1.1 ± 0.1 µm), as shown in Figure 3.9a-b. In contrast, solutions of as-received PS-PNIPAM containing salt yield a hierarchical pore structure with sizes ranging from ~ 10 – 400 nm (Figure 3.9c-d). Presumably, this structure occurs due to the combined action of water condensation at the solvent/air interface due to cooling

by solvent evaporation, as is well-known for formation of breath figures, and subsequently osmotically-driven emulsification at the solvent/condensed water interface due to the presence of salt aggregates, as investigated here. This method provides a simple means to greatly increase the surface area of porous block copolymer polymer films.

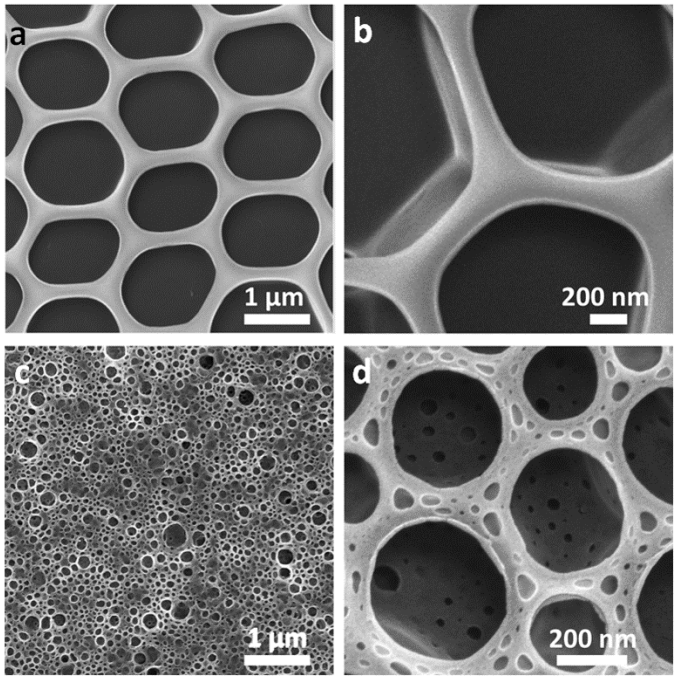

Figure 3.9 SEM images of (a-b) a 2-D porous film formed by casting a chloroform solution containing 10 mg/mL of purified PS-PNIPAM by the breath figure method, and (c-d) a hierarchically porous film formed by the combination of breath figures and osmotic-emulsification during casting from a chloroform solution containing 10 mg/mL of as-received PS-PNlPAM.

3.4 Conclusions

In conclusion, we have described a simple one-step method for the formation of tailored w/o/w double emulsions with highly stable inner water droplets. The inner water droplets with µm-scale sizes are spontaneously formed the interface of primary o/w droplets due to an osmotic pressure difference relative to the continuous water phase provided by salt species dispersed in the oil phase. This osmotic driving force, and thus the

characteristics of the resulting emulsions, can be easily tuned by varying the amount of salt dispersed in the oil phase, as well as the concentration of salt dissolved in the continuous water phase. These highly stable double emulsions can be converted to multi-compartment polymer capsules with encapsulated species in their cores and shells, and similar effects can also be used to obtain hierarchically structured porous polymer films. We anticipate that the simplicity, versatility, and potential scalability of this route will make it a valuable tool in the formulation of multiple emulsions and block copolymer assemblies.

3.5 References

1. Seifriz, W. Studies in emulsions. *J Phys Chem-Us* **29**, 834-841 (1925).

2. van Dongen, S. F. M., Verdurmen, W. P. R., Peters, R. J. R. W., Nolte, R. J. M., Brock, R. & van Hest, J. C. M. Cellular integration of an enzyme-loaded polymersome nanoreactor. *Angew. Chem. Int. Ed.* **49**, 7213-7216 (2010).

3. Dams, S. S. & Walker, I. M. [5] multiple emulsions as targetable delivery systems. In: *Methods in enzymology* (Ed:Ralph Green KJW). Academic Press (1987).

4. Lindenstruth, K. & Müller, B. W. W/o/w multiple emulsions with diclofenac sodium. *European Journal of Pharmaceutics and Biopharmaceutics* **58**, 621-627 (2004).

5. Choi, S.-W., Zhang, Y. & Xia, Y. Fabrication of microbeads with a controllable hollow interior and porous wall using a capillary fluidic device. *Adv. Funct. Mater.* **19**, 2943-2949 (2009).

6. Liu, L., Wang, W., Ju, X.-J., Xie, R. & Chu, L.-Y. Smart thermo-triggered squirting capsules for nanoparticle delivery. *Soft Matter* **6**, 3759-3763 (2010).

7. Gallarate, M., Carlotti, M. E., Trotta, M. & Bovo, S. On the stability of ascorbic acid in emulsified systems for topical and cosmetic use. *Int. J. Pharm.* **188**, 233-241 (1999).

8. Miyazawa, K., Yajima, I., Kaneda, I. & Yanaki, T. Preparation of a new soft capsule for cosmetics. *J Cosmet Sci* **51**, 239-252 (2000).

9. Chakravarti, A. K., Chowdhury, S. B., Chakrabarty, S., Chakrabarty, T. & Mukherjee, D. C. Liquid membrane multiple emulsion process of chromium(vi) separation from waste waters. *Colloids and Surfaces A: Physicochemical and Engineering Aspects* **103**, 59-71 (1995).

10. Bose, S. & Saha, S. K. Synthesis and characterization of hydroxyapatite nanopowders by emulsion technique. *Chem Mater* **15**, 4464-4469 (2003).

11. Norton, J., Malik, K. R., Darr, J. A. & Rehman, I. Recent developments in processing and surface modification of hydroxyapatite. *Adv Appl Ceram* **105**, 113-139 (2006).

12. Sadasivan, S., Khushalani, D. & Mann, S. Synthesis of calcium phosphate nanofilaments in reverse micelles. *Chem Mater* **17**, 2765-2770 (2005).

13. Ficheux, M. F., Bonakdar, L., Leal-Calderon, F. & Bibette, J. Some stability criteria for double emulsions. *Langmuir* **14**, 2702-2706 (1998).

14. Garti, N. Double emulsions - scope, limitations and new achievements. *Colloid Surface A* **123**, 233-246 (1997).

15. Mezzenga, R., Folmer, B. M. & Hughes, E. Design of double emulsions by osmotic pressure tailoring. *Langmuir* **20**, 3574-3582 (2004).

16. Kanouni, M., Rosano, H. L. & Naouli, N. Preparation of a stable double emulsion (w1/o/w2): Role of the interfacial films on the stability of the system. *Advances in Colloid and Interface Science* **99**, 229-254 (2002).

17. Palencia, M. & Rivas, B. L. Metal-ion retention properties of water-soluble amphiphilic block copolymer in double emulsion systems (w/o/w) stabilized by non-ionic surfactants. *J Colloid Interf Sci* **363**, 682-689 (2011).

18. Sameh, H., Wafa, E., Sihem, B. & Fernando, L.-C. Influence of diffusive transport on the structural evolution of w/o/w emulsions. *Langmuir* **28**, 17597-17608 (2012).

19. Florence, A. T. & Whitehill, D. The formulation and stability of multiple emulsions. *Int. J. Pharm.* **11**, 277-308 (1982).

20. Hong, L., Sun, G., Cai, J. & Ngai, T. One-step formation of w/o/w multiple emulsions stabilized by single amphiphilic block copolymers. *Langmuir* **28**, 2332-2336 (2012).

21. Besnard, L. *et al.* Multiple emulsions controlled by stimuli-responsive polymers. *Adv. Mater.* **25**, 2844-2848 (2013).

22. Utada, A. S., Lorenceau, E., Link, D. R., Kaplan, P. D., Stone, H. A. & Weitz, D. A. Monodisperse double emulsions generated from a microcapillary device. *Science* **308**, 537-541 (2005).

23. Shum, H. C., Zhao, Y. J., Kim, S. H. & Weitz, D. A. Multicompartment polymersomes from double emulsions. *Angewandte Chemie-International Edition* **50**, 1648-1651 (2011).

24. Lee, M. H., Hribar, K. C., Brugarolas, T., Kamat, N. P., Burdick, J. A. & Lee, D. Harnessing interfacial phenomena to program the release properties of hollow microcapsules. *Adv. Funct. Mater.* **22**, 131-138 (2012).

25. Kim, S. H. & Weitz, D. A. One-step emulsification of multiple concentric shells with capillary microfluidic devices. *Angewandte Chemie-International Edition* **50**, 8731-8734 (2011).

26. Chu, L. Y., Utada, A. S., Shah, R. K., Kim, J. W. & Weitz, D. A. Controllable monodisperse multiple emulsions. *Angewandte Chemie-International Edition* **46**, 8970-8974 (2007).

27. Aserin, A. *Multiple emulsion: Technology and applications*. Wiley (2008).

28. Jiao, J. & Burgess, D. J. Rheology and stability of water-in-oil-in-water multiple emulsions containing span 83 and tween 80. *Aaps Pharmsci* **5**, (2003).

29. Bonnet, M., Cansell, M., Placin, F., David-Briand, E., Anton, M. & Leal-Calderon, F. Influence of ionic complexation on release rate profiles from multiple water-in-oil-in-water (w/o/w) emulsions. *J Agr Food Chem* **58**, 7762-7769 (2010).

30. Bibette, J., Calderon, F. L. & Poulin, P. Emulsions: Basic principles. *Rep Prog Phys* **62**, 969-1033 (1999).

31. Shum, H. C., Bandyopadhyay, A., Bose, S. & Weitz, D. A. Double emulsion droplets as microreactors for synthesis of mesoporous hydroxyapatite. *Chem Mater* **21**, 5548-5555 (2009).

32. Jiao, J., Rhodes, D. G. & Burgess, D. J. Multiple emulsion stability: Pressure balance and interfacial film strength. *J Colloid Interf Sci* **250**, 444-450 (2002).

33. Yafei, W., Tao, Z. & Gang, H. Structural evolution of polymer-stabilized double emulsions. *Langmuir* **22**, 67-73 (2005).

34. Jager-Lezer, N. *et al.* Influence of lipophilic surfactant on the release kinetics of water-soluble molecules entrapped in a w/o/w multiple emulsion. *J Control Release* **45**, 1-13 (1997).

35. Hayward, R. C., Utada, A. S., Dan, N. & Weitz, D. A. Dewetting instability during the formation of polymersomes from block-copolymer-stabilized double emulsions. *Langmuir* **22**, 4457-4461 (2006).

36. Rother, G. & Findenegg, G. H. Monolayer firms of ps-b-peo diblock copolymers at the air/water- and an oil/water-interface. *Colloid Polym Sci* **276**, 496-502 (1998).

37. Zhu, J. & Hayward, R. C. Interfacial tension of evaporating emulsion droplets containing amphiphilic block copolymers: Effects of solvent and polymer composition. *J Colloid Interf Sci* **365**, 275-279 (2012).

38. Wang, J. Y., Xu, T., Leiston-Belanger, J. M., Gupta, S. & Russell, T. P. Ion complexation: A route to enhanced block copolymer alignment with electric fields. *Phys Rev Lett* **96**, 128301 (2006).

39. Xu, T., Goldbach, J. T., Leiston-Belanger, J. & Russell, T. P. Effect of ionic impurities on the electric field alignment of diblock copolymer thin films. *Colloid Polym Sci* **282**, 927-931 (2004).

40. Kim, C. S. & Oh, S. M. Importance of donor number in determining solvating ability of polymers and transport properties in gel-type polymer electrolytes. *Electrochim Acta* **45**, 2101-2109 (2000).

41. Zhu, J. & Hayward, R. C. Spontaneous generation of amphiphilic block copolymer micelles with multiple morphologies through interfacial instabilities. *J Am Chem Soc* **130**, 7496-7502 (2008).

42. Langevin, D. Micelles and microemulsions. *Annu Rev Phys Chem* **43**, 341-369 (1992).

43. Narang, A. S., Delmarre, D. & Gao, D. Stable drug encapsulation in micelles and microemulsions. *Int. J. Pharm.* **345**, 9-25 (2007).

44. Widawski, G., Rawiso, M. & Francois, B. Self-organized honeycomb morphology of star-polymer polystyrene films. *Nature* **369**, 387-389 (1994).

45. Srinivasarao, M., Collings, D., Philips, A. & Patel, S. Three-dimensionally ordered array of air bubbles in a polymer film. *Science* **292**, 79-83 (2001).

46. Karthaus, O., Maruyama, N., Cieren, X., Shimomura, M., Hasegawa, H. & Hashimoto, T. Water-assisted formation of micrometer-size honeycomb patterns of polymers. *Langmuir* **16**, 6071-6076 (2000).

47. Bunz, U. H. F. Breath figures as a dynamic templating method for polymers and nanomaterials. *Adv. Mater.* **18**, 973-989 (2006).

CHAPTER 4

MEASURING MECHANICAL PROPERTIES OF THIN POLYMER SHEETS BY ELASTO-CAPILLARY BENDING‡

4.1 Introduction

Flexible elastic sheets present a rich array of basic questions in mechanics,[1-4] and offer applications in areas such as biomaterials and stimuli-responsive devices.[5-8] However, while knowledge of the elastic properties of these materials is critical for understanding and controlling their behavior, classical macroscopic methods such as tensile or compression testing, or shear rheology are often poorly suited for characterizing thin and highly compliant membranes. Further, when the materials are also limited to small in-plane sizes, or need to be studied while immersed in a liquid medium, traditional testing methods are further complicated.

Several methods have been developed in recent years to address these limitations on the mechanical characterization of compliant materials on small scales. Nano-indentation, frequently conducted with an atomic force microscope (AFM) tip, has become a valuable tool for measuring the local elastic properties of nano- to micro-scale soft objects such as thin polymer films,[9-11] gels,[12-14] and cells.[15-20] However, interpretation of data from this technique often leads to model-dependent conclusions that are complicated by the presence of adhesion between the tip and the sample, by viscoelastic and/or poroelastic relaxation processes, and by effects from underlying rigid substrates.[9, 20, 21] Aspiration methods based on measuring the deformation of a sample pulled into a capillary by a

‡ Submitted to journal

known hydrostatic pressure are also useful, but have so far been applied only to nearly spherical samples.[22-26] Cavitation rheology—a measurement of the pressure needed to form a bubble of fluid in a material—is especially promising due to its simplicity and flexibility, though so far has not been applied to thin layers, and can be complicated for brittle materials where fracture precedes elastic cavitation.[27-29] Wrinkling of thin films supported on soft and thick elastic substrates,[30] or floating on liquid surfaces[31] has been exploited to quantitatively characterize elastic properties of thin films, and very recently, tensile testing of thin films floating on the surface of water was reported.[32] However, these techniques generally require films with in-plane dimensions of several millimeters and elastic moduli in the range of MPa - GPa.

In this chapter, we introduce a simple approach for characterizing the elastic modulus of soft materials and thin films that takes advantage of bending driven by interfacial tension, inspired by previous work on capillary folding of polymer sheets.[33] The balance between interfacial tension γ and bending energy of elastic sheets is described by a critical dimension (R) of sheet where $C_b \sim 1$. This critical dimension is referred to as the elasto-capillary bending length $L_{EC} = \sqrt{\bar{E}h^3/12\gamma}$, where $\bar{E}$ is the plane stain modulus and h is the thickness of the sheet. When the in-plane size of the sheet is comparable to L_{EC}, interfacial tension between a liquid droplet and the surrounding medium is just sufficient to bend the material, providing a very simple means to determine $\bar{E}$ of the sold film. For appropriate wetting conditions, this condition does not depend on the advancing contact angle of the solid/liquid/medium interface, meaning that the method requires separate measurements of only the liquid/medium interfacial tension, and the sheet thickness. We demonstrate that the technique is suitable for measuring materials over a broad range of

moduli (from kPa to GPa), including those with small in-plane dimensions, and immersed in liquid media as well as air.

4.2 Experimental

4.2.1 Materials and methods

Poly(*para*-methyl styrene) (PpMS) containing pendent benzophenone photo-crosslinkers and Poly(*N*-isopropyl acrylamide-*co*-acrylamidobenzophenone-*co*-acrylic acid-*co*-rhodamine B- methacrylate) (PNIPAM copolymer) were synthesized by free-radical polymerization at 80 in 1,4-dioxane for 15 h following 3 freeze-pump-thaw cycles and a nitrogen purge using re-crystallized azobisisobutyronitrile (AIBN, Aldrich) as initiator, as described in more detail previously[34]. Polymers were purified by precipitation into stirring diethyl ether (for PNIPAM) or methanol (for PpMS), washed by filtration and dried in a vacuum oven overnight. Solvent, monomer and initiator concentrations were chosen as follows: *N*-isopropylacrylamide (NIPAm; 3 g, Tokyo Chemical Industry Co., Ltd), acrylamidobenzophenone (AAmBP; 533 mg), acrylic acid (AAc; 114.5 L), rhodamine B- methacrylate (RhBMA; 47.6 mg), and AIBN (5 mg) in 30 mL of 1,4-dioxane, resulting in a copolymer with 7 mol% AAmBP, 5.5 mol% AAc, and 0.3 mol% RhBMA; *p*-methylstyrene (pMS; 3 mL, Aldrich), AAmBP (0.45 g), and AIBN (0.015 g) in 30 mL of 1,4-dioxane, resulting in a copolymer containing 10 mol% AAmBP. Polymer compositions were confirmed by ^{1}H NMR (Bruker DPX300).

Polyacrylamide (PAAm) hydrogels were synthesized using 1000 µL of an aqueous pre-gel solution containing 660 mM acrylamide (Aldrich), 19.8 mM bisacrylamide

(Research Organics), and 25 µL of 3.4 wt% 2,2'-Azobis[2-methyl-N-(2-hydroxyethyl)propionamide] aqueous solution as the photo-initiator (VA-086, Wako Pure Chemical Industries, Ltd.). The degassed pre-gel solution was inserted between two (tridecafluoro-1,1,2,2-tetrahydrooctyl)dimethylchlorosilane (Gelest) treated glass slides separated by 1 mm spacers. Gelation was induced by exposure to UV light (wavelength: 365 nm) for 20 min, followed by immersion in deionized water for 2 – 3 d to fully swell the gel and remove unreacted monomers.

For experiments with Kapton film, a glass pasteur pipette (size 5 ¾") with a latex bulb was used to reduce the volume of the mm-scale liquid droplet. For micro-capillary suction, a cylindrical glass capillary (1 mm outer and 0.6 mm inner diameters, World Precision Instruments) was tapered to a sharp tip (~ 10 µm diameter) using a Narishige PC-10 micropipette puller and MF-900 microforge, then connected to a syringe pump.

4.2.2 Preparation of polymer sheets and photolithography

We employ a single mask lithographic patterning of photo-crosslinkable copolymer films. To prepare copolymer films, 3 wt% poly(sodium acrylate) (Sigma-Aldrich, M_w = 30 kg/mol) was spin-coated onto a pre-cleaned 1 x 1 cm^2 silicon substrate, yielding a film of ~ 100 nm thickness. The residual solvent was evaporated on a 150 °C hot plate for 2 h, then the film was soaked in 1.35 M $CaCl_2$ solution for 20 s to form a Ca^{2+}-crosslinked sacrificial layer.[35]

Films of PpMS with thicknesses of 120 and 670 nm were prepared by spin-casting (2 krpm) of 20 and 100 mg/mL PpMS solutions in toluene onto the sacrificial layer, respectively. Films of PpMS with thicknesses of 2 µm were prepared via drop-casting of

30 µL PpMS solution in toluene (10 mg/mL) on the sacrificial layer, and the solvent was slowly removed for 5 h at 68 °C in a closed glass bottle (0.13 oz capacity glass jar, Freund Container). To prepare PNIPAM copolymer sheets, a 100 µL drop of copolymer solution in chloroform (1 wt %) was dropcast on the sacrificial layer, and the solvent was slowly evaporated for 5 h at 50 °C in a closed glass bottle (0.13 oz capacity glass jar, Freund Container). The film thickness was measured using a stylus profilometer (Dektak, Veeco).

Square and triangular mask patterns with a variety of side lengths were designed in AutoCAD (AutoDesk) and printed on transparent photomasks (Front Range PhotoMask). The PpMS and PNIPAM copolymer films were crosslinked by using an epi-fluorescence microscope (Zeiss Axiovert 200) and a homemade mask aligner. Films were exposed to 120 J cm^{-2} of UV light (X-Cite Series 120, Lumen Dynamics; excitation filter: 365 nm) through the photomask to fully crosslink PpMS, and 3 to 30 J cm^{-2} to partially crosslink PNIPAM, using a 10x objective. Reported UV doses are measured using X-Cite XR2100 power meter (Lumen Dynamics) at 365 nm.

The PpMS and PNIPAM sheets were submerged in solvent mixture of toluene:hexane = 1:0.6, and water:ethanol = 1:2, respectively, to dissolve uncrosslinked portions; then immersed in an aqueous medium (containing 1 mM NaCl, and 1 mM phosphate buffer, pH 7.2) to dissolve the sacrificial layer, release the films, and induce swelling in the case of the PNIPAM films.

4.2.3 Characterization

Micrographs and movies of elasto-capillary bending of Kapton films were taken using a digital camera (PowerShot A640, Canon). For PpMS and PNIPAM films,

fluorescence and bright field optical micrographs and movies were obtained using a Zeiss Axiovert 200 inverted optical microscope with a 2.5x objective, and a QImaging camera (Retiga-2000R). PNIPAM samples for UV/vis absorption spectroscopy were dropcast by placing 200 μL of copolymer solution in chloroform (1 wt%) onto UV-ozone treated 1 × 1/2 in. quartz plates, and the solvent was slowly evaporated for 5 h at 50 °C in a closed 0.13 oz capacity glass jar. Prepared PNIPAM film on quartz substrates were exposed to 365 nm UV radiation using a UV illumination system (Newport, Model 97434). Conversion of AAmBP was monitored as a function of UV dose with a Hitachi U-3010 spectrophotometer in absorbance mode over a wavelength range of 200−800 nm. Due to differences in the spectral profiles, a given dose corresponds to different extents of benzophenone conversion using the two lamps. To correct for this difference, the swelling ratio was determined as a function of dose for both lamps (Figure 4.1) and used to convert doses from one lamp to the other. Doses stated in the manuscript correspond to those measured for the X-Cite light source. The shear modulus of PAAm hydrogels was measured by rheometer (Kinexus Pro+, Malvern) with 8 or 20 mm diameter stainless steel parallel plates; the storage modulus was determined at 1 Hz and 3 % strain.

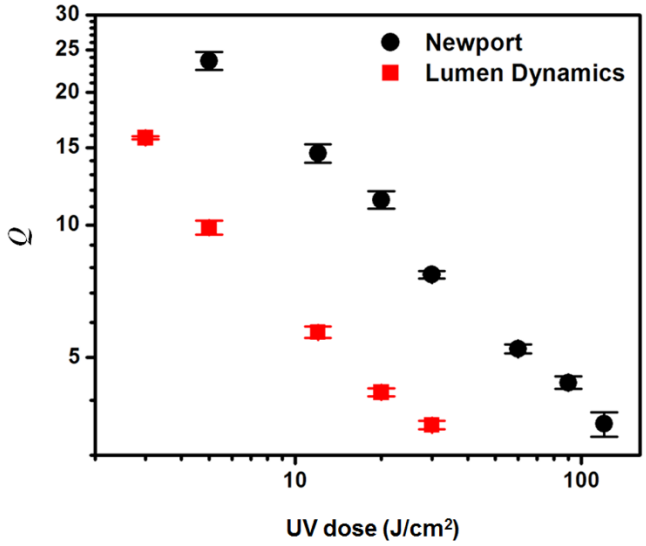

Figure 4.1 The degree of volumetrc swelling Q is used to convert between UV doses measured for two different light sources with different spectral characteristics.

4.3 Results and discussion

4.3.1 Calibration of the method

When a liquid droplet supported on a thin solid film is reduced in volume, and the contact line remains pinned at the film boundaries, interfacial tension is sufficient to wrap the sheet into a 'closed' state, where opposite edges or corners of the film are brought into contact. The minimum in-plane size of the sheet required for wrapping is given by $L_c = A L_{EC}$, where A is a prefactor that depends on the geometric shape of the sheet.[33] Importantly, the value of A is anticipated to be *independent of the contact angle* of the liquid droplet on the sheet, due to the pinning of the contact line at the sheet edge. This means that once A is determined for a given shape, a simple measurement of L_c using any probe fluid that has

a known (or measurable) value of γ with the medium will directly reveal the sheet's bending stiffness $\bar{E}h^3/12$.

Table 4.1 Liquid droplet and continuous fluid pairs used, and the corresponding advancing contact angles on planar Kapton films.

Drop phase	Continuous phase	Contact angle
Aqueous buffer solution*	Air	70°
Aqueous buffer solution*	Chloroform	115°
Aqueous buffer solution*	Silicone oil	102°
Chloroform	Aqueous buffer solution*	65°
Silicone oil	Aqueous buffer solution*	78°
Perfluorooctane	Aqueous buffer solution*	89°

(*Aqueous buffer solution containing 1 mM phosphate buffer and 1 mM NaCl, pH7.2)

To verify this expected independence with respect to the contact angle, and confirm previously reported values of *A*, we used samples of a commercial polyimide film (Kapton 30 HN, h = 7.6 μm) of known plane-strain modulus ($\bar{E}$ = 2.83 GPa) cut into square or equilateral triangles with side length *L*. Due to the excellent chemical resistance of the polyimide film, it was possible to use a variety of droplet and continuous phases, giving rise three-phase advancing contact angles ranging from 65 – 115 ° (Table 4.1). A liquid droplet with a size larger than *L* was first prepared, and then the film was placed at the droplet/medium interface, allowing the entire surface of the film to be wet with very small initial curvature (Figure 4.2a and d). Unlike in previous experiments relying on evaporation,[33] here we reduce the volume of the droplet by pipetting, enabling the use of non-volatile fluids, and increasing the speed of the experiments.

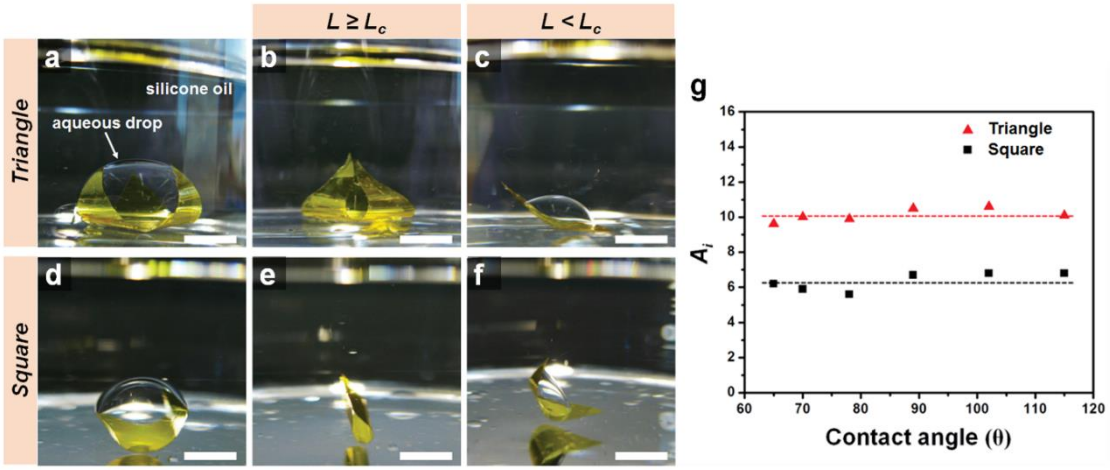

Figure 4.2 Calibration of geometric prefactors and contact angle effects. (a) A triangular polyimide sheet (Kapton 30 HN; h = 7.6 μm) was placed at the interface of an aqueous droplet and the silicone oil medium. Upon reducing the droplet volume by pipetting, (b) a film with L = 21 mm continually bent until opposing vertices contacted each other, indicating that $L \geq L_c$. In contrast, (c) a triangular film with L = 13 mm unbent due to depinning of the droplet from the sheet edges before the vertices met, indicating that $L < L_c$. (d) Similarly, a square sheet with (e) L = 11 mm bent until opposite sides were contacting, which (f) one with L = 9 mm did not. All scale bars are 5 mm. (g) The measured geometric prefactor A for triangles and squares is confirmed to be independent of the advancing contact angle of the liquid/solid/medium interface.

For films with $L > L_c$, a reduction in droplet volume caused the film to bend until opposite edges or corners met (Figure 4.2b and e). By contrast, for $L < L_c$, the droplet depinned from the sheet edges prior to contact of opposing edges/corners, and the bending of the film was reduced with further decreases in droplet volume (Figure 4.2c and f). By measuring sheets of several lengths, the critical value L_c was determined, and the prefactor A evaluated. As shown in Figure 4.2g, A was confirmed to be independent of the advancing contact angle over the range studied, with average values of 10.1 ± 0.4 for triangles and 6.3 ± 0.5 for squares. These values are in reasonable agreement with the respective literature values[33] of A = 11.9 and 7.0. For these sheets with L_c ~ 10 mm, the height of the

liquid droplet during bending to the closed state is only slightly smaller than the capillary length $\lambda_c = \sqrt{\gamma / \rho g}$ ($\lambda_c \approx 12$ mm for an aqueous droplet in the silicone oil medium), where ρ is the liquid density and g gravitational acceleration. However, as the measured values of L_c did not depend on the placement of the sheet on the top, bottom, or side of the droplet, we conclude that gravitational effects can safely be ignored, although this would likely not be the case for substantially larger values of L_c relative to λ_c.

4.3.2 Elasto-capillary bending of photo-crosslinkable polymer sheets

A topic of considerable recent interest has been the patterning of small-scale 3-dimensional structures by buckling of micro-patterned 2-dimensional sheets due to in-plane or through-thickness variations in stress.[2-4, 34, 36-45] Although the contrast in modulus of the constituent materials plays an important role in determining the shapes formed in these ways, independent measurements of the elastic properties in such systems can often be challenging, and thus new methods for quantitatively measuring the properties of micro-scale polymer sheets would be valuable. To demonstrate the utility of elasto-capillary bending measurements in this context, we next studied two different photo-crosslinkable polymers that have recently been used by our group[46, 47] and others[48, 49] to fabricate sub-millimeter-scale buckled and self-folding sheets.

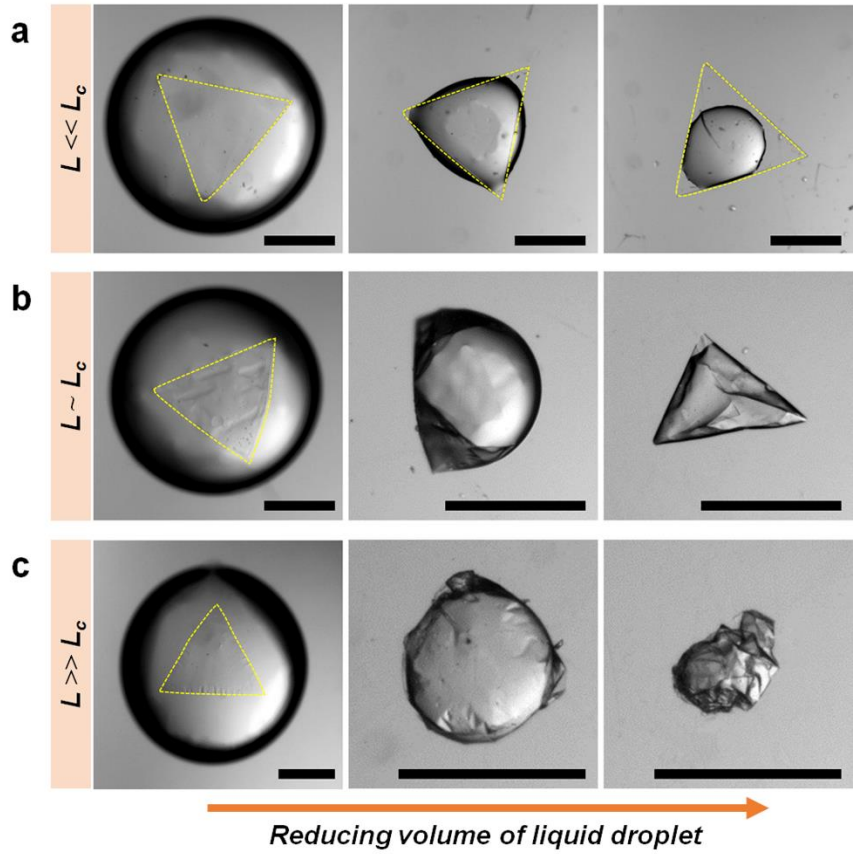

Figure 4.3 Elasto-capillary bending measurements of glassy PpMS sheets. Optical micrographs of PpMS sheets with side lengths L = 1 mm and different thicknesses h at the PFO/aqueous medium interface. Upon reducing the volume of the PFO droplet, PpMS sheets with (a) h = 2 µm remain nearly flat, while (b) those with h = 0.67 µm wrap the droplet and (c) those with h = 0.12 µm crumple. All scale bars are 500 µm.

We first consider a rigid glassy copolymer of *para*-methyl styrene (PpMS) containing pendent benzophenone (BP) photo-crosslinkers. As our approach for patterning these materials involves releasing the sheet into an aqueous medium as the final step, we chose perfluorooctane (PFO) as a water-immiscible droplet phase that would not swell or plasticize the PpMS sheets. Based on a literature value of 3.8 GPa for the plane-strain modulus of polystyrene[50] (which presumably has similar elastic properties to PpMS), and a value of γ = 0.058 N/m for the PFO/aqueous solution interface (measured by pendent

drop tensiometry), we estimated that a film thickness of $h \approx 1$ μm should yield values of L_c ~ 1 mm, matching the sizes that can be conveniently photo-patterned. However, to test this prediction, we first prepared sheets with several different thicknesses, as summarized in Figure 4.3. For a thickness of h = 2.0 μm, interfacial tension was insufficient to bend 1-mm-sized sheets, corresponding to $L << L_c$, while for a thickness of h = 0.12 μm, sheets became highly crumpled[51] upon removing PFO, corresponding to $L >> L_c$. An intermediate thickness of h = 0.67 μm, however, yielded wrapping of droplets in a manner consistent with $L \sim L_c$.

Having identified an appropriate film thickness for elasto-capillary bending measurements, we fixed h = 0.67 μm, and prepared a series of square and equilateral triangle shapes with side lengths varying from 0.2 – 1.0 mm in 0.1 mm increments. Using a micro-capillary to remove PFO from droplets with interfacially adsorbed PpMS sheets, and an optical microscope to visualize the deformation, we determined values of L_c = 450 ± 50 μm for triangles and 250 ± 50 μm for squares. The corresponding values of plane strain modulus estimated from

$$\overline{E} = \frac{12\gamma}{h^3}\left(\frac{L_c}{A}\right)^2 \quad (1)$$

were 4.6 ± 1.0 and 3.8 ± 1.4 GPa, in good agreement with expectations based on the literature value for polystyrene.

To compare these values with those from an established technique on the same materials, nanoindentation experiments were also performed on PpMS sheets prepared with a much greater thickness ($h \sim 100$ μm) to minimize the influence of the underlying rigid substrate. The measured value of $\bar{E}$ = 9.3 ± 0.2 GPa is two-fold higher than the result

from elasto-capillary bending. However, in light of the tendency of nanoindentation to over-estimate the modulus of polymer materials by a factor of 2-3 times due to viscoelastic effects,[9] this discrepancy is not unexpected. Thus, in addition to being simpler to perform from the perspective of instrumentation and analysis, we suggest that capillary bending may even be a more reliable alternative to nanoindentation for the characterization of glassy polymer films in the appropriate thickness range.

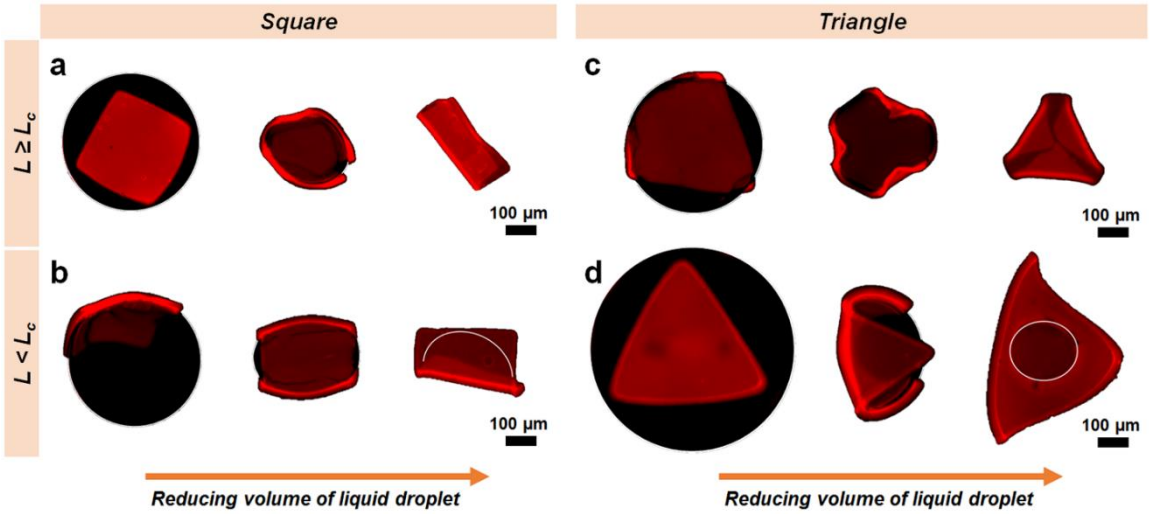

Figure 4.4 Elasto-capillary bending of measurements of PNIPAM hydrogel sheets. Fluorescence micrographs of crosslinked hydrogels at the interface of a PFO droplet (black in color or denoted by a white line) and the aqueous medium. Square and triangle sheets (a,c) wrapping the droplet for $L \geq L_c$, and (b,d) unbending for $L < L_c$, during micro-capillary suction of PFO droplets.

Next, to demonstrate the applicability of the method for soft materials, we characterized films of a photo-crosslinkable poly(*N*-isopropyl acrylamide-*co*-acrylic acid) (PNIPAM) copolymer crosslinked to different extents. Based on the content of photo-crosslinker expected moduli in the range of 100 kPa – 1 MPa, we estimated from Equation (1) that sheets with $h \approx 20$ - 30 μm and $L \sim 1$ mm would be appropriate. Films with dry thicknesses of $h_0 = 8$ - 13 μm were prepared by solution casting and photo-patterned into

square or equilateral triangular shapes with dry side lengths of L_0 = 0.2 – 0.6 mm using a UV dose sufficient to convert only a fraction of the benzophenone units. The sheets were then allowed to swell to equilibrium in a low ionic-strength aqueous buffer (1 mM NaCl and 1 mM phosphate buffer, pH 7.2) at room temperature, and the volumetric swelling $Q = (L/L_0)^3$ was determined using an optical microscope to measure the change in size (where we separately verified that the swelling is isotropic by also measuring the change in thickness for selected samples). Doses ranging from 3 – 30 mJ/cm^2 were employed, resulting in values of Q from 15.8 – 3.5. As summarized in Figure 4.4, PNIPAM sheets were placed at the interface between a PFO droplet and the aqueous medium, and the droplet volume was reduced using microcapillary suction (see Supporting Information Movies S3 and S4). After determining the value of L_c necessary for folding, $\bar{E}$ of the swelled hydrogel sheets, ranging from 200 – 800 kPa, were determined via Equation (1).

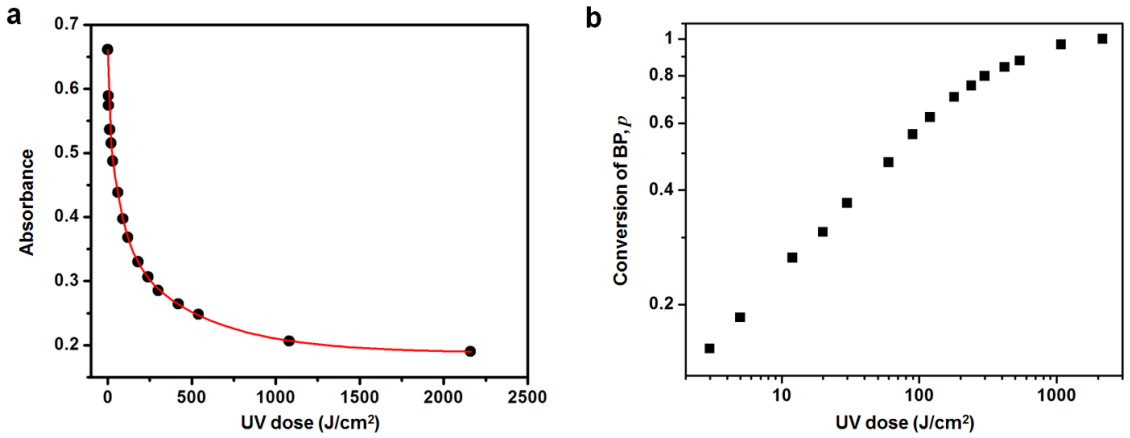

Figure 4.5 (a) Acrylamidobenzophenone (AAmBP) conversion is monitored via UV/vis absorption of the decay of the π-π* peak (300 nm) with increasing UV dose. Absorbance data are well described by a tri-exponential decay (red line) suggesting the presence of three different characteristic populations of AAmBP. (b) The conversion p of BP as a function of dose, determined from the normalized difference between the absorbance of the π-π* peak before and after UV exposure. While the origin of the three populations of BP is not well understood, over the range of crosslinking considered in the current report (corresponding to $p \approx 0.2 - 0.7$) the population with intermediate characteristic dose dominates the behavior.

To better understand how the modulus and swelling ratio of the gel sheets depend on crosslinking, we used UV-vis spectroscopy to characterize how the conversion p of benzophenone units increased as a function of UV dose. Specifically we monitored the decay of the π–π* absorption peak at 300 nm after normalization at the isosbestic point (Supporting Information Figure 4.5), using a previously described procedure[46]. Assuming that each benzophenone unit has an equal probability of forming a crosslink, p should be inversely proportional to the length N of polymer strands in the crosslinked network. In Figure 4.6, we plot both $\bar{E}$ and Q as functions of p. The relationship between Q and p can be well-described by a power law dependence $Q \sim p^a$ with a best-fit exponent of a = -1.6 ± 0.1, which is in good agreement with the theoretically predicted exponent of -1.5 for polyelectrolyte gels at low salt concentration[52]. The modulus values measured by elasto-capillary bending are also consistent with power-law behavior $\bar{E} \sim p^b$ with a best-fit exponent of b = 1.7 ± 0.1 that is slightly larger than the predicted exponent for the shear modulus of 1.5, although this agreement is reasonable in light of the modest range of p studied, and the likelihood that Poisson's ratio v, where $\bar{E} = 2G/(1 - v)$, also increases slightly with increasing crosslink density. While the dependence of $\bar{E}$ and Q separately on crosslink density has not previously been widely studied, the prediction $G \sim Q^{-1}$ has been verified in several previous reports,[52-54] and within uncertainty, the data reported here also support the dependence $\bar{E} \sim Q^{-1}$.

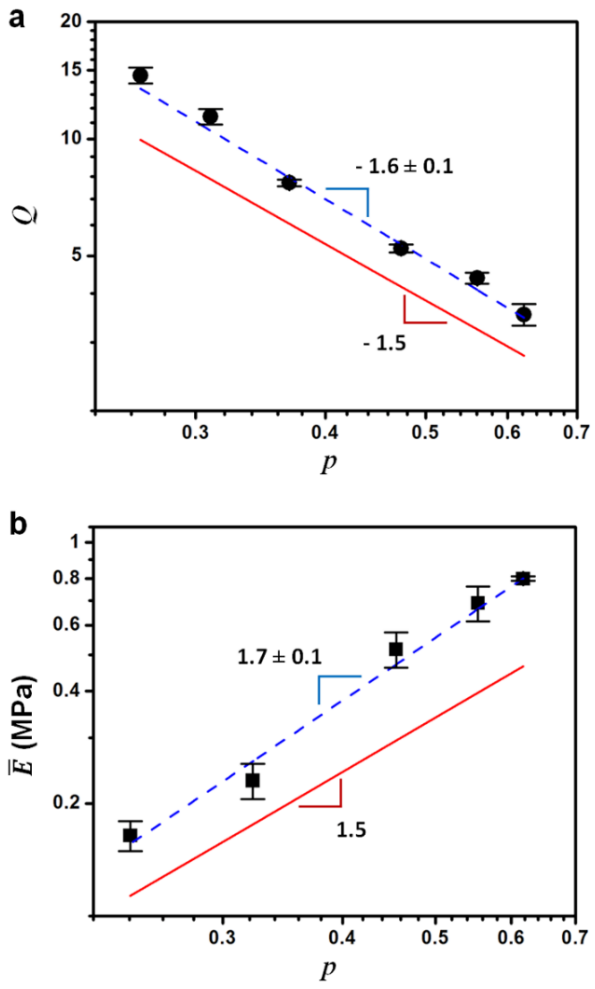

Figure 4.6 Swelling ratios and moduli of hydrogels as a function of crosslinking. Logarithmic scales are used for both axes for the plots in (a) and (b), and predicted scaling exponents are drawn as solid lines. (a) Plotting the volumetric swelling ratio (Q) against the conversion of photo-crosslinker (p) reveals a best-fit slope (dashed line) of -1.6 ± 0.1 close to the predicted power law of -1.5. (b) Plotting the plane strain modulus ($\bar{E}$) against the relative conversion of photo-crosslinker (p) reveals a best-fit slope of 1.7 ± 0.1 (dashed line) close to the predicted power law of 1.5 for the shear modulus.

4.3.3 Elasto-capillary bending of soft neutral hydrogel sheets

To prove the suitability of elasto-capillary bending to characterize very soft elastic materials ($\bar{E} \sim 10^3$ Pa), polyacrylamide (PAAm) hydrogel films were prepared by photo-initiated polymerization in aqueous solution. The technique allows for a very simple

measurement of the elastic modulus in the fully swelled state, which can be challenging using conventional shear rheology due to the possibility for slip between the hydrated gel surface and the rheometer plate. Swelled PAAm gel sheets (volumetric swelling ratio 1.3) were placed at the interface of a water droplet and silicone oil medium, and the water droplet volume reduced by pipetting (Figure 4.7) to determine a value of L_c = 21.5 ± 0.5 mm for squares with h = 1 mm (once again, the measured value did not depend on the orientation of the drop, indicating that gravity can safely be ignored). Consequently, from Equation (1), we estimate $\bar{E}$ = 5.6 ± 0.3 kPa, in very good agreement with the shear modulus G = 2.5 ± 0.4 kPa determined from shear rheology on PAAm gels in the unswelled state.

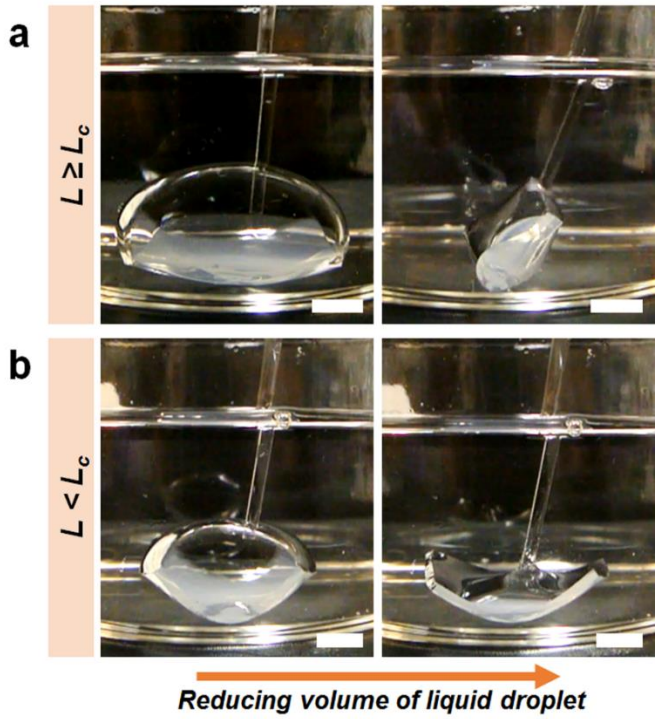

Figure 4.7 Elasto-capillary bending of measurements of swelled polyacrylamide (PAAm) hydrogel sheets. Photographs of PAAm hydrogels at the interface of a water droplet and the silicone oil medium. A square sheet (a) wrapping the droplet for $L \geq L_c$, and (b) unbending for $L < L_c$, as the droplet volume is reduced by pipetting. All scale bars are 5 mm.

4.4 Conclusions

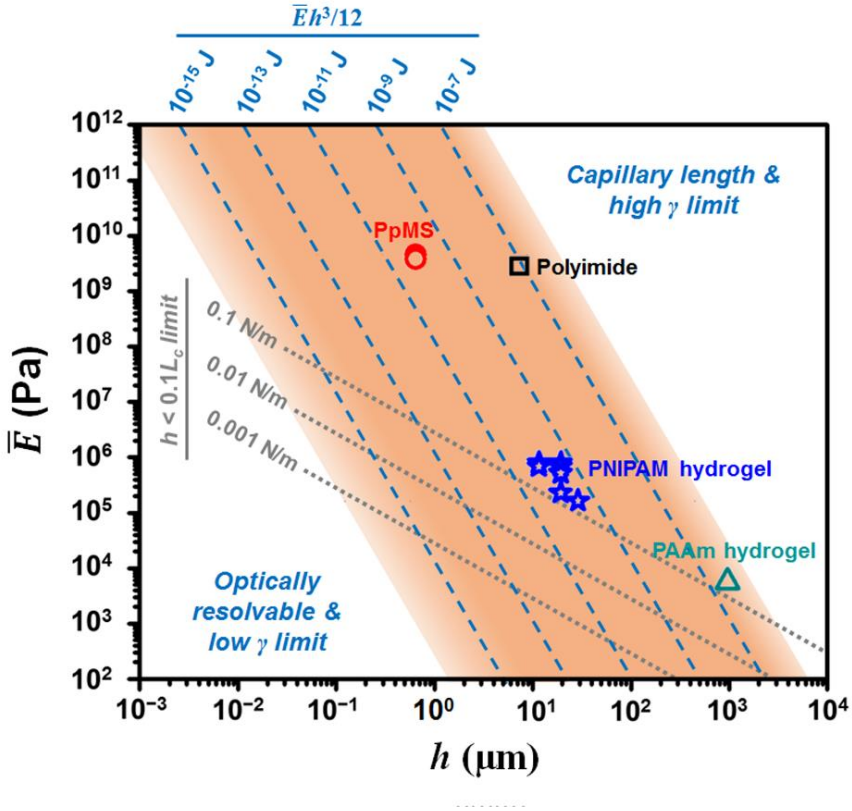

Figure 4.8 Accessible regions for elasto-capillary bending measurements. Logarithmic scales are used for the plane strain modulus ($\bar{E}$) and thickness (h) axes. The lines of slope -3 (dashed lines) correspond to constant values of bending modulus ($\bar{E}h^3/12$), and the shaded region represents the region accessible for square geometries using realistic values of critical sheet dimensions L_c and surface tension γ. The gray dotted lines of slope -1 correspond to constant values of $\bar{E}h$ corresponding to the thin film limit $h < 0.1\ L_c$ for the indicated values of γ. The samples characterized here are plotted as symbols.

We have developed an elasto-capillary bending approach to measure elastic moduli in the range of kPa - GPa for polymer films, including those with sub-millimeter scale dimensions, and immersed in liquid media. The method requires only separate measurements of the liquid/air or liquid/liquid interfacial tension and the sheet thickness, and involves simple and rapid measurements not requiring any special equipment. In Figure 4.8, we illustrate the broad range of applicability of this technique via a log-log plot

denoting the range of accessible values (shaded in gray) of $\bar{E}$ and h for sheets of square geometry. The dashed lines of slope -3 correspond to constant values of bending modulus $\bar{E}h^3/12$ (or equivalently, $\gamma L_c^2/A^2$). The upper end of the shaded regime corresponds to a maximum sheet size of $L_c \approx 10$ mm dictated by the capillary length, along with a surface tension of $\gamma \approx 0.1$ N/m achievable using typical liquids in contact with air. Similarly, the lower end is determined from the in-plane dimensions easily observable by optical techniques $L_c \approx 10$ μm, and a minimum surface tension of $\gamma \approx 1$ mN/m that can be achieved for weakly immiscible fluids, or via the use of surfactants. These values of L_c and γ represent a range of *8 orders of magnitude* in bending modulus (from ~ 10^{-15} – 10^{-7} J) that can be reasonably accessed by the technique. Presumably, the use of alternative sheet geometries, density matched liquids, very high- or low-interfacial tension fluids, and/or high resolution imaging methods could extend this range further in both directions, as denoted by the gradient regions surrounding the shaded region in Figure 4.8. However, even based on currently feasible experiments, the technique can be applied to characterize films of the stiffest known materials ($\bar{E}$ ~ 1 TPa) with thicknesses in the range of ~ 3 nm – 3 μm, as well as the softest solids ($\bar{E}$ ~ 100 Pa) with thicknesses near 1 mm.

Another important constraint on the method is that the film must be thin, i.e., $h << L_c$, so that the strains induced by bending are small, and linear elasticity can reasonably be applied. Using $h = 0.1L_c$ as a maximum tolerable thickness, Equation (1) becomes $\bar{E}\,h > 1200\gamma/A^2$, a constraint denoted by the dotted gray lines of slope -1 in Figure 4.8. For each line (corresponding to values of $\gamma = 0.001$, 0.01, and 0.1 N/m), the region above and to the right is accessible, while that below and to the left is not. This consideration dictates that for soft materials ($\bar{E}$ ~ 100 Pa – 1 MPa), the combination of a relatively low surface tension

fluid and a large thickness will be necessary to ensure that the strains induced by surface tension remain modest.

In light of the simplicity of these measurements, the broad range of moduli that can be accessed, and the applicability for samples with small dimensions in liquid environments, we expect that elasto-capillary bending will prove to be a valuable and versatile method for measuring the elastic modulus of flexible thin films. While we have investigated only homogeneous elastic films here, the method should be more broadly applicable for determining the bending stiffness of composites, laminates, and (with suitable choices of film geometry) materials with in-plane anisotropy.

4.5 References

1. Sharon, E. & Efrati, E. The mechanics of non-euclidean plates. *Soft Matter* **6**, 5693-5704 (2010).

2. Chen, D., Yoon, J., Chandra, D., Crosby, A. J. & Hayward, R. C. Stimuli-responsive buckling mechanics of polymer films. *Journal of Polymer Science Part B: Polymer Physics* **52**, 1441-1461 (2014).

3. Ionov, L. Biomimetic hydrogel-based actuating systems. *Adv. Funct. Mater.* **23**, 4555-4570 (2013).

4. Gracias, D. H. Stimuli responsive self-folding using thin polymer films. *Current Opinion in Chemical Engineering* **2**, 112-119 (2013).

5. Mitragotri, S. & Lahann, J. Physical approaches to biomaterial design. *Nat. Mater.* **8**, 15-23 (2009).

6. Stuart, M. A. C. *et al.* Emerging applications of stimuli-responsive polymer materials. *Nat. Mater.* **9**, 101-113 (2010).

7. Chen, X. & Yin, J. Buckling patterns of thin films on curved compliant substrates with applications to morphogenesis and three-dimensional micro-fabrication. *Soft Matter* **6**, 5667-5680 (2010).

8. Studart, A. R. & Erb, R. M. Bioinspired materials that self-shape through programmed microstructures. *Soft Matter* **10**, 1284-1294 (2014).

9. VanLandingham, M. R., Villarrubia, J. S., Guthrie, W. F. & Meyers, G. F. Nanoindentation of polymers: An overview. *Macromol Symp* **167**, 15-43 (2001).

10. Geng, K. B., Yang, F. Q., Druffel, T. & Grulke, E. A. Nanoindentation behavior of ultrathin polymeric films. *Polymer* **46**, 11768-11772 (2005).

11. Du, B., Tsui, O. K. C., Zhang, Q. & He, T. Study of elastic modulus and yield strength of polymer thin films using atomic force microscopy. *Langmuir* **17**, 3286-3291 (2001).

12. Hu, Y. H., You, J. O., Auguste, D. T., Suo, Z. G. & Vlassak, J. J. Indentation: A simple, nondestructive method for characterizing the mechanical and transport properties of ph-sensitive hydrogels. *J Mater Res* **27**, 152-160 (2012).

13. Drira, Z. & Yadavalli, V. K. Nanomechanical measurements of polyethylene glycol hydrogels using atomic force microscopy. *J Mech Behav Biomed* **18**, 20-28 (2013).

14. Gupta, S., Greeshma, T., Basu, B., Goswami, S. & Sinha, A. Stiffness- and wettability-dependent myoblast cell compatibility of transparent poly(vinyl alcohol) hydrogels. *J Biomed Mater Res B* **101B**, 346-354 (2013).

15. Alonso, J. L. & Goldmann, W. H. Feeling the forces: Atomic force microscopy in cell biology. *Life Sci.* **72**, 2553-2560 (2003).

16. Ren, J. & Zou, Q. Z. A control-based approach to accurate nanoindentation quantification in broadband nanomechanical measurement using scanning probe microscope. *Ieee T Nanotechnol* **13**, 46-54 (2014).

17. Rettler, E., Hoeppener, S., Sigusch, B. W. & Schubert, U. S. Mapping the mechanical properties of biomaterials on different length scales: Depth-sensing indentation and afm based nanoindentation. *J Mater Chem B* **1**, 2789-2806 (2013).

18. Demichelis, A., Pavarelli, S., Mortati, L., Sassi, G. & Sassi, M. Study on the afm force spectroscopy method for elastic modulus measurement of living cells. *J Phys Conf Ser* **459**, (2013).

19. Vinckier, A. & Semenza, G. Measuring elasticity of biological materials by atomic force microscopy. *FEBS Lett.* **430**, 12-16 (1998).

20. Ebenstein, D. M. & Pruitt, L. A. Nanoindentation of biological materials. *Nano Today* **1**, 26-33 (2006).

21. Kaufman, J. D. & Klapperich, C. M. Surface detection errors cause overestimation of the modulus in nanoindentation on soft materials. *J Mech Behav Biomed* **2**, 312-317 (2009).

22. Evans, E. A., Waugh, R. & Melnik, L. Elastic area compressibility modulus of red-cell membrane. *Biophys. J.* **16**, 585-595 (1976).

23. Mabrouk, E. *et al.* Formation and material properties of giant liquid crystal polymersomes. *Soft Matter* **5**, 1870-1878 (2009).

24. Wyss, H. M., Franke, T., Mele, E. & Weitz, D. A. Capillary micromechanics: Measuring the elasticity of microscopic soft objects. *Soft Matter* **6**, 4550-4555 (2010).

25. Wyss, H. M. *et al.* Biophysical properties of normal and diseased renal glomeruli. *Am J Physiol-Cell Ph* **300**, C397-C405 (2011).

26. Luo, Y. N. *et al.* A constriction channel based microfluidic system enabling continuous characterization of cellular instantaneous young's modulus. *Sensors and Actuators B: Chemical* **202**, 1183-1189 (2014).

27. Zimberlin, J. A., Sanabria-DeLong, N., Tew, G. N. & Crosby, A. J. Cavitation rheology for soft materials. *Soft Matter* **3**, 763-767 (2007).

28. Chin, M. S., Freniere, B. B., Fakhouri, S., Harris, J. E., Lalikos, J. F. & Crosby, A. J. Cavitation rheology as a potential method for in vivo assessment of skin biomechanics. *Plast. Reconstr. Surg.* **131**, 303e-305e (2013).

29. Cui, J., Lee, C. H., Delbos, A., McManus, J. J. & Crosby, A. J. Cavitation rheology of the eye lens. *Soft Matter* **7**, 7827-7831 (2011).

30. Stafford, C. M. *et al.* A buckling-based metrology for measuring the elastic moduli of polymeric thin films. *Nat. Mater.* **3**, 545-550 (2004).

31. Huang, J. *et al.* Capillary wrinkling of floating thin polymer films. *Science* **317**, 650-653 (2007).

32. Kim, J.-H. *et al.* Tensile testing of ultra-thin films on water surface. *Nat Commun* **4**, (2013).

33. Py, C., Reverdy, P., Doppler, L., Bico, J., Roman, B. & Baroud, C. N. Capillary origami: Spontaneous wrapping of a droplet with an elastic sheet. *Phys. Rev. Lett.* **98**, 156103 (2007).

34. Kim, J., Hanna, J. A., Byun, M., Santangelo, C. D. & Hayward, R. C. Designing responsive buckled surfaces by halftone gel lithography. *Science* **335**, 1201-1205 (2012).

35. Linder, V., Gates, B. D., Ryan, D., Parviz, B. A. & Whitesides, G. M. Water-soluble sacrificial layers for surface micromachining. *Small* **1**, 730-736 (2005).

36. Kim, J., Hanna, J. A., Hayward, R. C. & Santangelo, C. D. Thermally responsive rolling of thin gel strips with discrete variations in swelling. *Soft Matter* **8**, 2375-2381 (2012).

37. Byun, M., Santangelo, C. D. & Hayward, R. C. Swelling-driven rolling and anisotropic expansion of striped gel sheets. *Soft Matter* **9**, 8264-8273 (2013).

38. Wu, Z. L. *et al.* Three-dimensional shape transformations of hydrogel sheets induced by small-scale modulation of internal stresses. *Nat Commun* **4**, 1586 (2013).

39. Therien-Aubin, H., Wu, Z. L., Nie, Z. H. & Kumacheva, E. Multiple shape transformations of composite hydrogel sheets. *J Am Chem Soc* **135**, 4834-4839 (2013).

40. Ionov, L. 3d microfabrication using stimuli-responsive self-folding polymer films. *Polym Rev* **53**, 92-107 (2013).

41. Stoychev, G., Zakharchenko, S., Turcaud, S., Dunlop, J. W. C. & Ionov, L. Shape-programmed folding of stimuli-responsive polymer bilayers. *ACS Nano* **6**, 3925-3934 (2012).

42. Alben, S., Balakrisnan, B. & Smela, E. Edge effects determine the direction of bilayer bending. *Nano Letters* **11**, 2280-2285 (2011).

43. Malachowski, K. *et al.* Stimuli-responsive theragrippers for chemomechanical controlled release. *Angew. Chem. Int. Ed.*, n/a-n/a (2014).

44. Fernandes, R. & Gracias, D. H. Self-folding polymeric containers for encapsulation and delivery of drugs. *Adv Drug Deliver Rev* **64**, 1579-1589 (2012).

45. Malachowski, K. *et al.* Stimuli-responsive theragrippers for chemomechanical controlled release. *Angew. Chem. Int. Ed.* **53**, 8045-8049 (2014).

46. Christensen, S. K., Chiappelli, M. C. & Hayward, R. C. Gelation of copolymers with pendent benzophenone photo-cross-linkers. *Macromolecules* **45**, 5237-5246 (2012).

47. Chiappelli, M. C. & Hayward, R. C. Photonic multilayer sensors from photo-crosslinkable polymer films. *Adv. Mater.* **24**, 6100-+ (2012).

48. Zakharchenko, S., Puretskiy, N., Stoychev, G., Stamm, M. & Ionov, L. Temperature controlled encapsulation and release using partially biodegradable thermo-magneto-sensitive self-rolling tubes. *Soft Matter* **6**, 2633-2636 (2010).

49. Stoychev, G., Puretskiy, N. & Ionov, L. Self-folding all-polymer thermoresponsive microcapsules. *Soft Matter* **7**, 3277-3279 (2011).

50. Brandrup, J. I. E. H. *Polymer handbook*. Wiley (1989).

51. King, H., Schroll, R. D., Davidovitch, B. & Menon, N. Elastic sheet on a liquid drop reveals wrinkling and crumpling as distinct symmetry-breaking instabilities. *Proc. Natl. Acad. Sci. USA* **109**, 9716-9720 (2012).

52. Rubinstein, M., Colby, R. H., Dobrynin, A. V. & Joanny, J.-F. Elastic modulus and equilibrium swelling of polyelectrolyte gels. *Macromolecules* **29**, 398-406 (1996).

53. Dubrovskii, S. A. & Rakova, G. V. Elastic and osmotic behavior and network imperfections of nonionic and weakly ionized acrylamide-based hydrogels. *Macromolecules* **30**, 7478-7486 (1997).

54. Skouri, R., Schosseler, F., Munch, J. P. & Candau, S. J. Swelling and elastic properties of polyelectrolyte gels. *Macromolecules* **28**, 197-210 (1995).

CHAPTER 5

EDGE-DEFINED METRIC BUCKLING OF TEMPERATURE-RESPONSIVE HYDROGEL RIBBONS AND RINGS[§]

5.1 Introduction

Recent years have seen great interest, and rapid advances, in the development of stimuli-responsive polymer networks for the fabrication of actuating and shape-reconfigurable materials.[1-7] A key strategy that has emerged from this work is the programming of thin sheets with in-plane non-uniformities in shrinkage, growth, or shape distortion, a principle that is also frequently found in natural morphogenetic processes.[8-14] Such patterns of deformation define a set of equilibrium distances between neighboring points (called the 'target metric' of the sheet) that are incompatible with the initially planar geometry of the film, thereby driving buckling into 3D shapes possessing distributions of Gaussian curvature that are defined by the pattern of distortion.[15] While considerable progress has been made in understanding and predicting the deformation of these 'non-Euclidean plates',[16-25] and in fabricating buckled structures by patterning the swelling/shrinking of hydrogels[26-31], and the director orientation in liquid crystalline polymers,[32-37] many open questions remain.

One area that remains incompletely understood is the importance of the sheet boundaries. Even for an idealized process that would yield a perfectly controlled metric,

[§] Reproduced and modified with permission from J. Bae, J.-H. Na, C. D. Santangelo and R. C. Hayward, "Edge-defined metric buckling of temperature-Responsive hydrogel ribbons and rings", *Polymer*, **55**, 5908-5914 (2014). Copyright © 2014 Elsevier

the presence of free boundaries can distort the shape of a finite thickness sheet, due to incompatibility of the curvature defined by the metric with the preferred (zero) mean curvature of the plate.[21, 38] Further, in any real process to fabricate non-Euclidean plates, the boundary is a natural location where non-idealities may occur that give rise to imperfections in the metric. However, the sensitivity of the metric to such edge defects remains largely unexplored.

One case in which boundaries are likely to play a particularly important role is that of ribbons, where the width of the sheet is greatly reduced compared to its length. Marder and Papanicolaou found that ribbons patterned with linear variations in growth across their widths will adopt helical configurations,[16] while Efrati et al. showed that hyperbolic metrics—exhibiting more extensive growth at both edges than in the center—would yield either helicoid- or catenoid-like shapes, depending on the form of the metric.[39] Chen et al. and Efrati et al. studied hyperbolic metrics on closed (annular) ribbons, and found that when the target Gaussian curvature and ring dimensions were commensurate, the system would adopt a 'resonant' state consisting of an integer number of wrinkle periods around the ring.[38-40] The complementary problem of 'overcurved' rings, i.e., with preferred *mean* curvature that does not match the geometric dimensions of the ring was studied by Mouthuy et al.; in this case, increasing overcurvature was shown to cause buckling first into a saddle-like shape, and then into multiply looped structures.[41]

In this chapter, we consider the importance of edge-induced 'metric imperfections' in driving the buckling of hydrogel strips and rings. Specifically, we employ a photo-crosslinkable hydrogel material that our groups have recently used to pattern discontinuous,[27, 28] or effectively continuous,[26] variations in the swelling of thin gel sheets

through a dual-mask photo-lithographic approach. Here, we show that as the width of the patterned gel objects is reduced to only several times their thickness, the lightly crosslinked regions at the sample edges that result from lithographic patterning give rise to a metric curvature even in nominally homogeneous gels. This provides a very simple, single-mask lithographic route to prepare temperature-responsive coiled strips, overcurved rings, and structures that tighten themselves around other object due to changes in temperature, which we dub 'self-cinching unknots'.

5.2 Experimental

5.2.1 Materials and methods

A photo-crosslinkable, fluorescent, and temperature responsive polymer was synthesized by free-radical polymerization at 80 °C in 1,4-dioxane for 15 h, following three freeze-pump-thaw cycles and a nitrogen purge, with re-crystallized azobisisobutyronitrile (AIBN, Aldrich) as an initiator, as reported previously [26]. The monomer, solvent and initiator concentrations were used as follows: *N*-isopropylacrylamide (NIPAm; 3 g, Tokyo Chemical Industry Co., Ltd), acrylamidobenzophenone (AAmBP; 533 mg), acrylic acid (AAc; 114.5 μL), rhodamine B-labeled methacrylate (RhBMA; 47.6 mg), and AIBN (5 mg), in 30 mL of 1,4-dioxane, resulting in a copolymer with 87.2 mol% NIPAm, 7 mol% AAmBP, 5.5 mol% AAc, and 0.3 mol% RhBMA, as confirmed by ^{1}H NMR (Bruker DPX300). This PNIPAM copolymer was purified by precipitation into stirring diethyl ether, washed by filtration, and dried in a vacuum oven overnight.

We employ a single mask lithographic patterning of photo-crosslinkable copolymer films. To prepare copolymer films, 3 wt% poly(sodium acrylate) (Sigma-Aldrich, M_w = 30

kg/mol) was spin-coated onto a pre-cleaned 1 x 1 cm^2 silicon substrate, yielding a ~ 100-nm-thick film. The residual solvent was evaporated on a 150 °C hot plate for 2 h, then the film was soaked in 1.35 M $CaCl_2$ solution for 20 s to form a Ca^{2+}-crosslinked sacrificial layer.[42] A 100 µL drop of copolymer solution in chloroform (1 wt %) was spread on the sacrificial layer, and the solvent was slowly evaporated for 5 h at 50 °C in a closed glass bottle (0.13 oz capacity glass jar, Freund Container) to yield 7-14 µm thick films, as measured using a stylus profilometer (Dektak, Veeco).

We designed mask patterns in AutoCAD (AutoDesk), and the designed patterns were printed on transparent photomasks (Front Range PhotoMask). The PNIPAM copolymer films were crosslinked by using an epi-fluorescence microscope (Zeiss Axiovert 200) and a homemade mask aligner. The film was exposed to 30 J cm^{-2} of UV light (excitation filter: 365 nm) through the photomask, using a 10x objective of an epi-fluorescence microscope, with the sample plane much closer to the objective than the focal plane, to improve the uniformity of illumination. This dose was found to be sufficient to fully convert the benzophenone crosslinkers within the exposed region of the film. The film was submerged in a mixture of water and ethanol (1 : 2 by volume) to dissolve uncrosslinked portions, then immersed in an aqueous medium (containing 1 mM NaCl, and 1 mM phosphate buffer, pH 7.2) to dissolve the sacrificial layer and induce swelling of the patterned gel films.

To demonstrate self-cinching behavior, a cylindrical glass capillary (1 mm outer and 0.6 mm inner diameters, World Precision Instruments) was tapered to a sharp tip (~ 10 µm diameter) using a Narishige PC-10 micropipette puller and MF-900 microforge.

5.2.2 Characterization

Fluorescence and bright field optical micrographs and movies were obtained using a Zeiss Axiovert 200 inverted optical microscope with either a 2.5x or a 100x oil-immersion objective, and a QImaging camera (Retiga-2000R). A swelled hydrogel reference disk was characterized using laser scanning confocal fluorescence microscopy (LSCM) (Zeiss LSM 510 META, 10x objective), wherein a HeNe laser (wavelength: 543 nm) was used to excite rhodamine B (detection filter: 560 nm), and the 3D reconstruction performed ImageJ software. The radius of curvature R_e of swelled strips, measured as the distance from the coil axis to the midplane of the gel, was determined from fluorescence images. The thermal response of rings was measured over the range of 22-55 °C using a microscope heat stage (Tempcontrol 37-2 digital, PeCon GmbH).

5.3 Results and discussion

5.3.1 Edge-induced metric curvature of hydrogel strips

Our approach to prepare photo-patterned gel films, as illustrated in Figure 5.1, involves illumination of a photo-crosslinkable poly(*N*-isopropyl acrylamide) (PNIPAM) copolymer film of thickness *h* with UV light (365 nm), through a photo-mask. Within the illuminated regions, the film is crosslinked into a network due to grafting of pendent benzophenone units onto neighboring chains.[43] The degree of crosslinking of the network controls its swelling when immersed in an aqueous medium—which we quantify in terms of Ω, the ratio of the area in the swelled state to that in the dry state—thereby providing a simple route to pattern the target metric of the gel film.[26, 27]

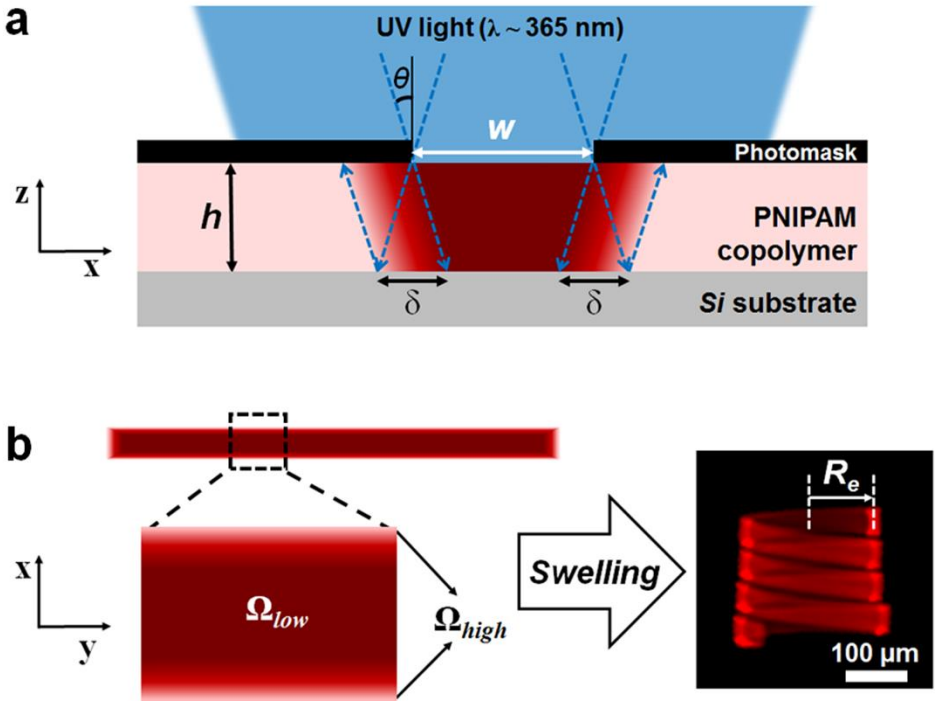

Figure 5.1 (a) A schematic illustration of the photolithographic patterning of a PNIPAM copolymer film supported on a silicon substrate, exposed using defocused UV light from an optical microscope. The convergence of the UV light leads to a gradient edge region of width δ with a lesser degree of crosslinking than the bulk. (b) These lightly crosslinked edges give rise to a larger degree of swelling (Ω) compared to the center region, which upon swelling drives the sufficiently narrow strips to coil with a constant radius of curvature R_e.

However, as with any lithographic process, the technique has a limited spatial resolution, meaning that even a perfectly sharp feature on the mask becomes blurred out over a finite length-scale δ within the polymer film. At a minimum, δ would be set by the diffraction of light. Here, however, the resolution is dominated by the convergence of the illuminating light, which is provided by the fluorescence excitation lamp on an inverted microscope. The microscope objective used gives a convergence angle of 11.6° (accounting for refraction in the polymer film), meaning that $\delta \approx 2h \tan\theta = 0.41h$, where the factor of 2 accounts for reflection from the silicon substrate underlying the polymer

film (Figure 5.1). Thus, even if the regions of the film in the interior of an illuminated region receive a sufficient dose of UV light to completely convert the benzophenone photo-crosslinkers, defining an areal swelling ratio Ω_{low} (here, $\Omega_{low} = 2.4$), there is a region of size δ at each edge where the crosslinking decreases continuously to zero, and therefore over which the swelling increases to some maximum value Ω_{high}, beyond which point the dose is insufficient to form a gel, and the material is removed during the developing step.

For large gel plates, with lateral dimensions $w >> h$, the influence of this edge region can be ignored in most respects, since it makes up only a small fraction of the area of the sheet. However, we find that relatively narrow strips ($w \approx 5h$ or below) with nominally uniform crosslinking always roll with a well-defined radius of curvature R_e, as shown in Figure 5.1b. As we establish in more detail below, this curvature arises because the edge regions of greater swelling define a hyperbolic metric. Since the variation in swelling is symmetric across the width of the strip, the preferred configuration should be an axisymmetric catenoid-like shape.[39, 40] All of the negative Gaussian curvature resides at the edges of the strip, and therefore the (metrically flat) central region of the strip seeks to adopt essentially a cylindrical configuration. For the sample in Figure 5.1b, the length of the strip is several times $2\pi R_e$, and therefore it coils into a tightly wound helical configuration to avoid self-intersection.

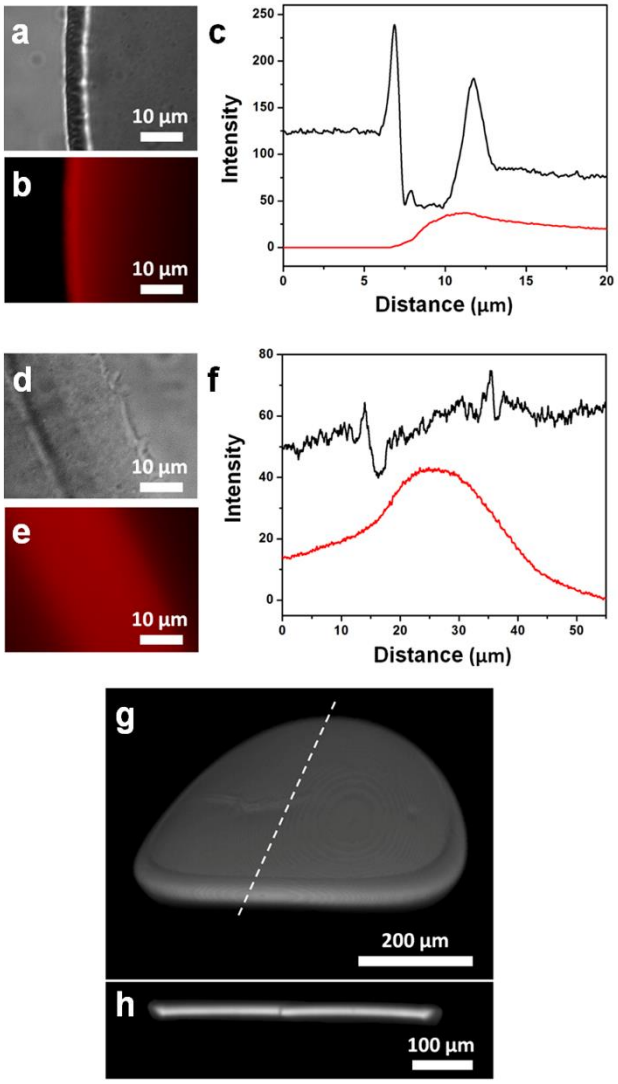

Figure 5.2 (a) Bright field optical micrograph, (b) fluorescence micrograph, and (c) extracted intensity profiles along the radial direction for a thin reference disk (diameter = 400 µm) of PNIPAM with nominally homogeneous crosslinking in the dry state; (d-f) corresponding images and profiles for the reference disk in the room-temperature swelled state. The black lines in (c,f) correspond to the bright-field images (a,d), while the red lines correspond to the fluorescence images (b,e). (g) A 3D reconstructed LSCM image of the crosslinked hydrogel disk in the room-temperature swelled state revealing the regions of greater swelling at the disk edge. (h) A cross-sectional profile taken along the dotted line in (g) reveals slanting of the edges.

To verify that the observed rolling behavior is indeed induced by edge effects, we first characterized the behavior of a large (400 µm diameter in the dry state, h = 7 µm)

'reference' disk with nominally uniform crosslinking, as summarized in Figure 5.2. In the dry state, a bright field optical micrograph (Figure 5.2a), and corresponding grayscale profile (Figure 5.2c), reveal two sharp features separated by 4.9 μm, which correspond to the top and bottom corners of the gel sheet. These corners are laterally offset from each other due to the convergence of the light source, as illustrated in Figure 5.1a. Similarly, fluorescence microscopy (Figure 5.2b) reveals a region of locally enhanced intensity at the edge, with a full width at half maximum of 4.5 ± 0.4 μm. As established previously,[26] the UV light used for photo-crosslinking also bleaches the rhodamine-B fluorophore, thus the higher fluorescence intensity corresponds to a smaller dose of UV, and therefore a lesser degree of crosslinking. Notably, both measures of the width of the edge region are in reasonable agreement with our estimate of $\delta \approx 0.41h = 2.9$ μm based on the convergence of the light source.

When immersed in an aqueous buffer at room temperature, the free-standing reference disk swells almost uniformly in size, to a value of $\Omega = 2.4$. Once again, bright field and fluorescence microscopies (Figure 5.2d-f) are used to characterize the edge region, which now has a width of 20.6 ± 0.7 μm. Were the edge region to undergo the same degree of swelling as the bulk of the plate, its width should increase by only a factor of $\Omega^{1/2} = 1.5$, i.e., to 7.0 μm. Thus, the radial swelling of the edge region is nearly *three-fold* as large as in the homogeneous central region of the disk. Importantly, the edge region experiences significant compressive stress along the azimuthal direction, since its connectivity to the rest of the plate restricts swelling in this dimension. However, this compression is not sufficient to drive buckling of the disk, since the edge region is so small in size compared to overall disk size. Indeed, as shown by the 3D laser scanning confocal

fluorescence microscopy (LSCM) reconstruction in Figure 5.2g, the disk remains almost flat in the swelled state. A small amount of curvature can indeed be seen (1.33 mm^{-1} for this sample)—as we have described previously,[27] such a 'background' level of curvature in the range of ~ 1 mm^{-1} or below is typically present due to gradients in residual stresses developed during casting of the film. In the LSCM image of Figure 5.2g, the higher swelling edge region lining the perimeter of the disk can also clearly be resolved.

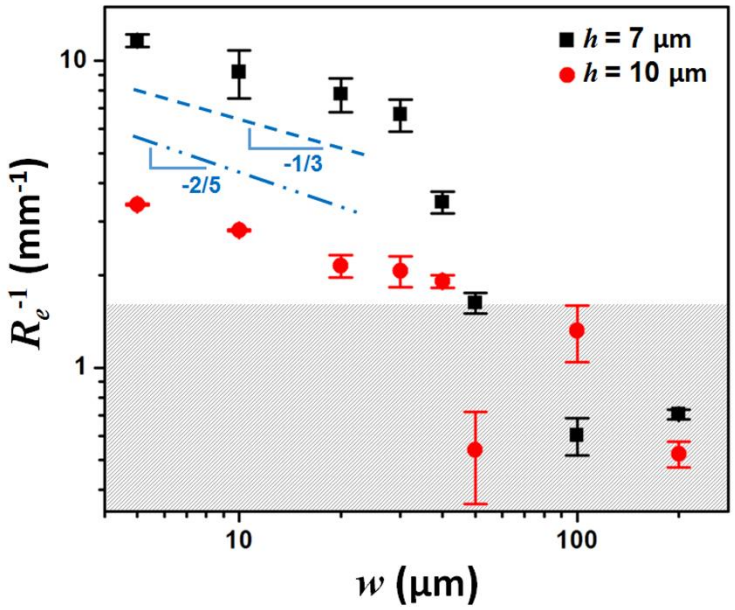

Figure 5.3 A plot of the curvature (R_e^{-1})adopted by strips of width w, for dry film thickness of h = 7 and 10 µm reveals power-law behaviors for small w with slopes similar to the range of -1/3 – -2/5 expected for swelling of symmetric 'tri-strips'. The shaded region represents the range of background curvatures observed for reference disks.

Next, we consider how the edge-defined metric curvature of gel strips depends on their dimensions. As shown in Figure 5.3, we quantified the curvature R_e^{-1} adopted by swelled linear strips similar to that in Figure 5.1b, as a function of their width w and thickness h (both measured in the dry state). In all cases, the strips are nominally crosslinked to completion, and uniformly, such that $\Omega = 2.4$ everywhere except in the edge

regions. Two important features should be noted. First, the curvature adopted by the thinner strips is considerably larger than even the upper end of the range of background curvatures seen for reference disks (denoted by the gray shaded region). Second, for the two thicknesses studied (h = 7 and 10 μm), R_e^{-1} is found to decrease consistently with increasing width, until $w \approx 50$ μm, beyond which point the curvatures are found to scatter in the typical range of background values. The observed dependence on w is a clear signature that buckling of thin strips is dominated by *in plane* variations in swelling, since a through-thickness gradient that was homogeneous in the film plane would drive buckling with a curvature that is independent to the lateral dimensions of the sheet. We note that the dependence of curvature on width w seems to follow a power-law dependence, i.e., $R_e \sim w^a$. Interestingly, the behavior is consistent with a value of a in the range of 1/3 – 2/5, which correspond to the large- and small-swelling contrast limits for a 'tri-strip" geometry consisting of a metrically flat central region bordered by two metrically flat edges with a different degree of swelling than the center.[26, 28, 44] In the current system, the edges are not metrically flat, but as a similar balance between bending of the entire ribbon and stretching of the regions near the edges determines the behavior in both cases, it is reasonable that a similar power-law dependence would be observed. Finally, we note that R_e^{-1} is also larger for the films with smaller h, which is qualitatively consistent with the behavior of tri-strips,[26, 28, 44] although in the current case an increase in film thickness should also give rise to an increase in the width of the edge regions, thus we would not expect a quantitative correspondence.

5.3.2 Overcurved hydrogel rings

Having established that the incompletely crosslinked edges surrounding gel strips give rise to a curvature R_e^{-1} that depends on the both the film thickness and strip width, we now consider the opportunities presented by this effect for the fabrication of actuating and self-shaping gel structures. Since only a single exposure of UV light is needed to define the patterned strips, there is no need for a mask alignment step as required in our previous work,[26-28] thus making the current process extremely simple. Correspondingly, however, the range of structures that can be programmed in this manner is somewhat restricted.

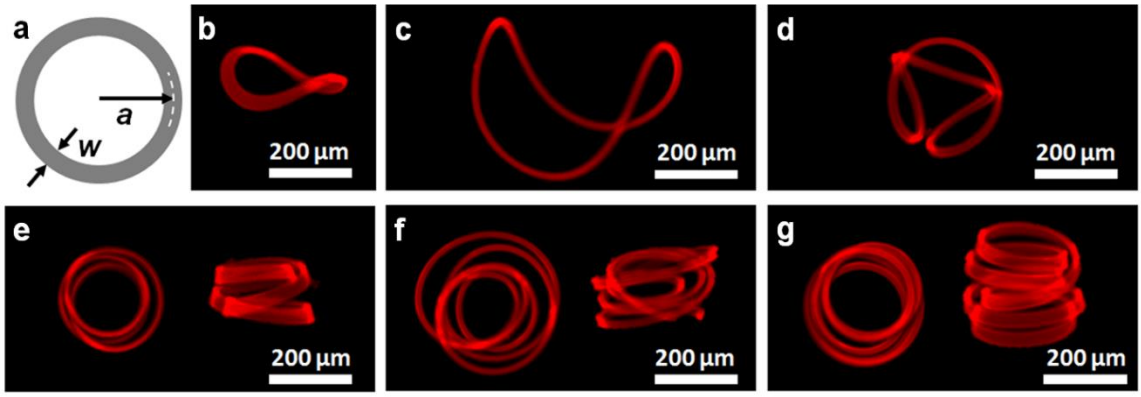

Figure 5.4 (a) A schematic illustration of the photo-patterned circular hydrogel rings of dry width *w* and radius *a*. (b-g) Fluorescence micrographs of circular rings in the room-temperature swelled state with different values of overcurvature O = (b) 1.2, (c) 1.8, (d) 2.1, (e) 2.4, (f) 4.2, and (g) 5.0.

One case for which the current method is well suited is the fabrication of overcurved hydrogel rings. Following Mouthuy et al.,[41] we define overcurvature O in terms of the preferred curvature of a local segment of a ring, in this case R_e^{-1}, and the geometric perimeter of the ring in the swelled state P, i.e., $O = P/(2\pi R_e)$. For a circular gel ring with radius a in the dry state, as illustrated in Figure 5.4a, $P = 2\pi a\Omega^{1/2}$, and therefore O =

$a\Omega^{1/2}/R_e$. In our case, R_e can be tuned by adjusting the width w or thickness h of the ring, as described above.

For $O > 1$, the preferred curvature of the gel ring is greater than allowed by its planar geometric shape, and therefore the ring will buckle out of plane to lower its elastic energy. As shown in Figure 5.4 for a series of rings with different dimensions, with increasing O from 1.2 – 5.0, the rings first adopt a saddle-like shape with 2-fold rotational symmetry, followed by multiply-coiled structures with first 3, and then 5 loops. These shapes are in excellent agreement with those reported by Mouthuy et al.,[41] for overcurved rings spanning a wide range of length-scales and material properties. When $O = 3$ and $O = 5$, the formation of these multiply-coiled structures can be easily rationalized, since this configuration allows the gel strip to take on an essentially constant curvature equal to its preferred value. At these values of O, therefore, the system is essentially unfrustrated, in that the elastic energy of the ring is not substantially increased by its closed topology. However, the formation of a saddle shape for rings with O close to 2, rather than a doubly-coiled ring, and the lack of a quadruply-coiled ring near $O = 4$, are the result of geometric constraints, a point to which we return below.

Figure 5.5 Thermal actuation of a circular ring (a = 190 µm) of photo-patterned PNIPAM hydrogel. Upon swelling as the temperature is reduced from 50 to 22 °C, the ring adopts characteristic shapes corresponding to values of O increasing from 1 to ≈ 3.

As the gel objects considered here are prepared from a PNIPAM copolymer, they exhibit temperature responsive swelling, and therefore metric curvature. While PNIPAM represents a well-studied[45, 46] and convenient model system to demonstrate the actuation of structures with edge-defined curvature, we emphasize that the same basic principles should apply to a wide variety of responsive materials, and to any patterning approach that yields a variation in metric at the edges. At a temperature of 50 ºC, the gels de-swell to nearly their dry dimensions, with a value of Ω that becomes nearly independent of crosslink density.[26, 27] This means that the edge-defined metric can be reversible 'erased' and regenerated by heating and cooling, respectively. As shown in Figure 5.5, a ring heated to 50 ºC adopts a nearly planar shape, but in the process of cooling to 22 ºC (where $O = 2.4$), the ring first progresses through the saddle-like configuration, and then to the triply coiled state. Notably, the progression of shapes adopted through several cycles of heating and cooling was nearly identical (as shown in the Supporting Movie for three cycles of swelling and deswelling of a circular ring with a maximum value of $O = 3$), demonstrating the ability to consistently form and retain a well-defined shape at each temperature. Such a stimulus-responsive overcurved ring functions as a very simple type of deployable structure; despite the fact that the gel is locally increasing in volume upon cooling from 50 to 22 ºC, the ring actually shrinks in in-plane dimension by forming a multiply-coiled ring, to an extent that can be specified by the ring geometry.

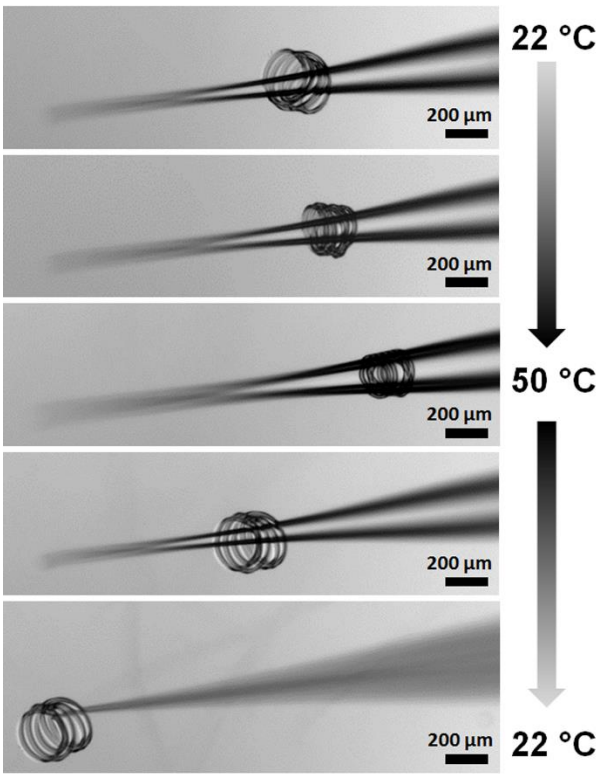

Figure 5.6 Thermally-triggered 'self-cinching' of a circular gel ring. A patterned ring (dry radius: 390 µm) at room temperature in an aqueous medium is initially swelled in a quintuply-coiled state ($O \approx 5$), but fastens itself around a glass pipette tip inserted through the center of the coil as de-swelling is induced by increasing the temperature to 50 °C. A subsequent decrease in temperature releases the ring and allows it to slide along the pipette due to gravity.

Another capacity in which such structures may find application is in 'self-cinching unknots', as shown in Figure 5.6. Here, a thin glass pipette tip is passed through a quintuply-coiled overcurved ring with $O = 5$ at 22 ºC. Upon de-swelling by heating to 50 ºC, the ring seeks to revert to its planar state, but is topologically restricted from doing so by the presence of the pipette tip. Instead, deswelling causes the ring to clamp down tightly around the pipette. Subsequently cooling back to 22 ºC causes the ring to re-swell into the quintuply-coiled state, thereby releasing its grip on the pipette. This motif is qualitatively similar to the 'slip knot' commonly employed in knitting and crocheting, in that neither are

actually topological knots, but both allow for latching onto a rod with an accessible end. We anticipate that the overcurved gel ring may have applications in biomedical and micro-robotic contexts as a simple route to fabricate a reversibly self-cinching fastener.

Finally, we consider a generalization of overcurvature to an n-sided regular polygon with side length a in the dry state, where $O = P/(2\pi R_e) = na\Omega^{1/2}/(2\pi R_e)$. We note that a gel strip will achieve a low-energy unfrustrated state whenever it can adopt a constant curvature equal to R_e^{-1}. Beyond this, the dominance of stretching over bending energy suggests that an idealized ribbon favors retaining the zero geodesic curvature of the center line – since this is a metric property – while allowing its normal curvature to change. The result is that, neglecting self-contact, a gel strip will tend to wrap the surface of a sphere of radius R_e. This is, indeed, what we see when the ribbon lengths are sufficiently short as to prevent self-contact.

Since a strip wrapping a sphere with zero geodesic curvature implies that the centerline itself should lie on a great circle, there are "special" values for the perimeter of an n-sided polygon $P = 2\pi R_e kn$, where k is any integer, such that each side wraps exactly k times around the sphere. This means that all vertices of the polygon lie on the same space point of the sphere and, moreover, that the polygon can retain its original vertex angles without modification. By contrast, if any of the side lengths P/n fail to be commensurate with the length of a great circle, the Gaussian curvature of the sphere would require the sum of the interior angles of the polygon to deviate from their value of 2π in the planar state. Alternatively, if the interior angles of the polygon are unable to deviate from their planar values (as is likely the case for gel strips with w substantially greater than h), this

means that the strip cannot satisfy its desired curvature everywhere. Thus, we may expect a special 'unfrustrated' configuration of an n-sided polygon whenever $O = P/(2\pi R_e) = kn$.

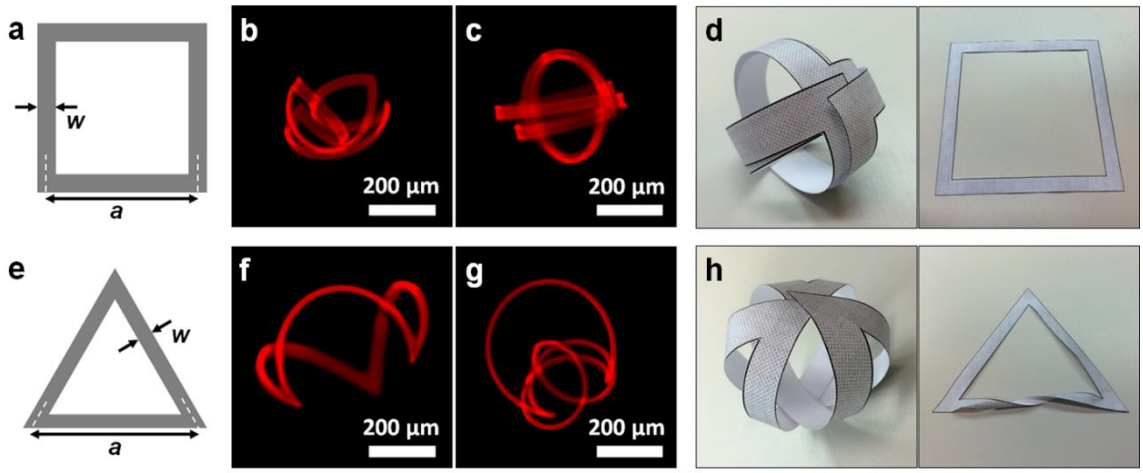

Figure 5.7 A schematic illustration of the photo-patterned (a) square and (e) triangular rings with dry width w and side length a. Fluorescence micrographs of square ring hydrogels in the room-temperature swelled state with overcurvatures O = (b) 3.1, (c) 4.7. (d) A paper model of the $O = 4$ wrapping of a sphere (left) by the square ring with no net twist (right). Fluorescence micrographs of triangular ring hydrogels in the room-temperature swelled state with overcurvatures O = (f) 2.2, (g) 3.0. (h) A paper model of an $O = 3$ triangle; to achieve wrapping around a sphere (left), a full twist has to be introduced (right). The dimensions of both paper models are a = 11.7 cm and w = 1 cm.

To test this picture, we prepared square and triangular rings with dry side length a, and width w, as summarized in Figure 5.7. As expected, for a value of O close to 4, square samples do indeed adopt an unfrustrated configuration in which each side adopts a full loop that follows a great circle of a sphere with radius R_e. The same behavior is also easily reproduced using a paper model of the square ring (Figure 5.7d). By contrast, however, triangles with $O \approx 3$ do not attain an unfrustrated shape, but instead exhibit significant deviations from the preferred curvature, as shown in Figure 5.7g. Here, a paper model is again informative—while the naively expected configuration can be attained (Figure 5.7h),

doing so requires that the triangle be prepared with a *full twist* included in its structure, as shown in Figure 5.7h.

Apparently, the local construction regarding the location and interior angles of vertices is not sufficient to ensure the existence of an unfrustrated value of *O*. The ribbon can also be viewed as a knot subject to the Călugăreanu–White–Fuller theorem,[47-49]

$$Tw + Wr = Lk,$$

where *Lk* is the linking number, associated with whether the two boundaries of the strip are linked, *Wr* is the writhe, or the number of positive crossings less the number of negative crossings, and *Tw* is known as the twist, which measures the rotation of a vector perpendicular to the centerline but lying on the ribbon. Therefore, it contains both the *intrinsic* twist as well as a component arising from the non-planarity of the ribbon.

This theorem makes manifest the intuition that the twist in a computer cable can be relieved in part by buckling out of the plane. In this case, we have $Tw = Lk = \pm 1$ in the twisted state; indeed, *Lk* is a topological invariant and therefore provides a more natural encoding of our intuitive notion of "twist" than *Tw*. For the gel rings discussed here, $Lk = 0$ in the as-patterned state, and therefore non-zero values of *Lk* cannot be attained (at least not without cutting and re-fastening the rings).

In our construction of spherically wrapped ribbons, the ribbon must cross itself as it traverses the sphere. These crossings can be chosen as either right- or left-handed crossings subject to the constraint that the ribbon remains unknotted. Since $Lk = 0$, we conclude that $Tw = - Wr$. A triangle with $O = 3$ has a minimum number of 3 crossings, corresponding to $Wr = \pm 1$. Consequently, $Tw = - Wr = \mp 1$, and the ribbon must have

made one full twist to accommodate the writhe. Additional crossings can be made, but must occur in pairs, and thus $Wr \neq 0$ for any wrapping of the $O = 3$ triangle on a sphere.

Conversely, when $O = 4$ for a square, the minimum number of crossings is 4. If these are chosen as two left- and two right-handed crossings, then $Wr = 0$, and therefore $Tw = 0$, and thus the untwisted square wraps the sphere with each side making one full revolution. The same picture applies for the case of the circular ring described previously; when $O = 3$, the minimum number of crossings is 2, while $O = 5$ must have at least 4 crossings, thus giving rise to the unfrustrated triply and quintuply-looped states, respectively. A doubly-looped state for $O = 2$ would require a full twist, as would a quadruply-looped state for $O = 4$, thus the untwisted ribbon is highly frustrated in both cases. Similarly, triangles or hexagons with $O = 6$ have an even number of crossings and can therefore also have $Tw = Wr = Lk = 0$, corresponding to unfrustrated states. It is perhaps surprising that such a rich geometrical landscape emerges from the simple process of patterning nominally homogeneous hydrogel rings, but it suggests that further study to understand the influence of both topological constraints and metric imperfections on the deformation of patterned gel sheets is likely to be rewarding.

5.4 Conclusions

In conclusion, we have established that the incompletely crosslinked edges surrounding photo-crosslinked hydrogels ribbons and rings serve as metric imperfections that drive buckling of sufficiently narrow strips. The target curvature at the mid-line of the ribbon is set by its width and thickness, in a fashion that is consistent with prior work on gel films intentionally patterned with higher swelling edges. This means that ribbons with

constant dimensions seek to follow great circles on a sphere, leading to buckling of 'overcurved' rings into multiply-coiled configurations that represent a simple experimental approach to shape-morphing structures, with possible applications in deployable gel structures and self-cinching fasteners. As patterning these structures requires only a single masked photo-lithographic exposure step, the investigation of other ribbon geometries is straightforward. In particular, we have considered the case of regular *k*-sided polygons and discovered that to adopt an unfrustrated state corresponding to a smooth wrapping of a sphere, not only must the overcurvature be an integer multiple of *k*, but the shape must make an even number of crossings as it traverses the sphere.

5.5 References

1. Geryak, R. & Tsukruk, V. V. Reconfigurable and actuating structures from soft materials. *Soft Matter* **10**, 1246-1263 (2014).

2. Lendlein, A. & Kelch, S. Shape-memory polymers. *Angewandte Chemie International Edition* **41**, 2034-2057 (2002).

3. Liu, C., Qin, H. & Mather, P. T. Review of progress in shape-memory polymers. *J Mater Chem* **17**, 1543-1558 (2007).

4. Ionov, L. Biomimetic hydrogel-based actuating systems. *Advanced Functional Materials* **23**, 4555-4570 (2013).

5. Ionov, L. 3d microfabrication using stimuli-responsive self-folding polymer films. *Polym Rev* **53**, 92-107 (2013).

6. Gracias, D. H. Stimuli responsive self-folding using thin polymer films. *Current Opinion in Chemical Engineering* **2**, 112-119 (2013).

7. White, E. M., Yatvin, J., Grubbs, J. B., Bilbrey, J. A. & Locklin, J. Advances in smart materials: Stimuli-responsive hydrogel thin films. *J Polym Sci Pol Phys* **51**, 1084-1099 (2013).

8. Kempaiah, R. & Nie, Z. H. From nature to synthetic systems: Shape transformation in soft materials. *J Mater Chem B* **2**, 2357-2368 (2014).

9. Studart, A. R. & Erb, R. M. Bioinspired materials that self-shape through programmed microstructures. *Soft Matter* **10**, 1284-1294 (2014).

10. Erb, R. M., Sander, J. S., Grisch, R. & Studart, A. R. Self-shaping composites with programmable bioinspired microstructures. *Nat Commun* **4**, 1712 (2013).

11. Li, B., Cao, Y. P., Feng, X. Q. & Gao, H. J. Mechanics of morphological instabilities and surface wrinkling in soft materials: A review. *Soft Matter* **8**, 5728-5745 (2012).

12. Liang, H. Y. & Mahadevan, L. Growth, geometry, and mechanics of a blooming lily. *P Natl Acad Sci USA* **108**, 5516-5521 (2011).

13. Armon, S., Efrati, E., Kupferman, R. & Sharon, E. Geometry and mechanics in the opening of chiral seed pods. *Science* **333**, 1726-1730 (2011).

14. Dunlop, J. W. C., Weinkamer, R. & Fratzl, P. Artful interfaces within biological materials. *Mater Today* **14**, 70-78 (2011).

15. Sharon, E. & Efrati, E. The mechanics of non-euclidean plates. *Soft Matter* **6**, 5693-5704 (2010).

16. Marder, M. & Papanicolaou, N. Geometry and elasticity of strips and flowers. *J Stat Phys* **125**, 1069-1096 (2006).

17. Dervaux, J. & Ben Amar, M. Morphogenesis of growing soft tissues. *Physical Review Letters* **101**, (2008).

18. Efrati, E., Sharon, E. & Kupferman, R. Elastic theory of unconstrained non-euclidean plates. *Journal of the Mechanics and Physics of Solids* **57**, 762-775 (2009).

19. Muller, M. M., Ben Amar, M. & Guven, J. Conical defects in growing sheets. *Physical Review Letters* **101**, (2008).

20. Lewicka, M., Mahadevan, L. & Pakzad, M. R. The foppl-von karman equations for plates with incompatible strains. *P R Soc A* **467**, 402-426 (2011).

21. Liang, H. Y. & Mahadevan, L. The shape of a long leaf. *P Natl Acad Sci USA* **106**, 22049-22054 (2009).

22. Dias, M. A., Hanna, J. A. & Santangelo, C. D. Programmed buckling by controlled lateral swelling in a thin elastic sheet. *Phys Rev E* **84**, (2011).

23. Modes, C. D., Bhattacharya, K. & Warner, M. Gaussian curvature from flat elastica sheets. *P R Soc A* **467**, 1121-1140 (2011).

24. Gemmer, J. & Venkataramani, S. C. Shape transitions in hyperbolic non-euclidean plates. *Soft Matter* **9**, 8151-8161 (2013).

25. Bende, N. P., Hayward, R. C. & Santangelo, C. D. Nonuniform growth and topological defects in the shaping of elastic sheets. *Soft Matter* **In press** (2014).

26. Kim, J., Hanna, J. A., Byun, M., Santangelo, C. D. & Hayward, R. C. Designing responsive buckled surfaces by halftone gel lithography. *Science* **335**, 1201-1205 (2012).

27. Kim, J., Hanna, J. A., Hayward, R. C. & Santangelo, C. D. Thermally responsive rolling of thin gel strips with discrete variations in swelling. *Soft Matter* **8**, 2375-2381 (2012).

28. Byun, M., Santangelo, C. D. & Hayward, R. C. Swelling-driven rolling and anisotropic expansion of striped gel sheets. *Soft Matter* **9**, 8264-8273 (2013).

29. Klein, Y., Efrati, E. & Sharon, E. Shaping of elastic sheets by prescription of non-euclidean metrics. *Science* **315**, 1116-1120 (2007).

30. Wu, Z. L. *et al.* Three-dimensional shape transformations of hydrogel sheets induced by small-scale modulation of internal stresses. *Nat Commun* **4**, 1586 (2013).

31. Therien-Aubin, H., Wu, Z. L., Nie, Z. H. & Kumacheva, E. Multiple shape transformations of composite hydrogel sheets. *J Am Chem Soc* **135**, 4834-4839 (2013).

32. van Oosten, C. L., Bastiaansen, C. W. M. & Broer, D. J. Printed artificial cilia from liquid-crystal network actuators modularly driven by light. *Nat Mater* **8**, 677-682 (2009).

33. de Haan, L. T. *et al.* Accordion-like actuators of multiple 3d patterned liquid crystal polymer films. *Advanced Functional Materials* **24**, 1251-1258 (2014).

34. de Haan, L. T., Sanchez-Somolinos, C., Bastiaansen, C. M. W., Schenning, A. P. H. J. & Broer, D. J. Engineering of complex order and the macroscopic deformation of liquid crystal polymer networks. *Angew Chem Int Edit* **51**, 12469-12472 (2012).

35. Lee, K. M., Bunning, T. J. & White, T. J. Autonomous, hands-free shape memory in glassy, liquid crystalline polymer networks. *Advanced Materials* **24**, 2839-2843 (2012).

36. Iamsaard, S. *et al.* Conversion of light into macroscopic helical motion. *Nat Chem* **6**, 229-235 (2014).

37. Yu, Y. L., Nakano, M. & Ikeda, T. Directed bending of a polymer film by light - miniaturizing a simple photomechanical system could expand its range of applications. *Nature* **425**, 145-145 (2003).

38. Efrati, E., Sharon, E. & Kupferman, R. Buckling transition and boundary layer in non-euclidean plates. *Phys Rev E* **80**, (2009).

39. Efrati, E., Sharon, E. & Kupferman, R. Hyperbolic non-euclidean elastic strips and almost minimal surfaces. *Phys Rev E* **83**, (2011).

40. Chen, B. G. G. & Santangelo, C. D. Minimal resonances in annular non-euclidean strips. *Phys Rev E* **82**, (2010).

41. Mouthuy, P.-O., Coulombier, M., Pardoen, T., Raskin, J.-P. & Jonas, A. M. Overcurvature describes the buckling and folding of rings from curved origami to foldable tents. *Nat Commun* **3**, 1290 (2012).

42. Linder, V., Gates, B. D., Ryan, D., Parviz, B. A. & Whitesides, G. M. Water-soluble sacrificial layers for surface micromachining. *Small* **1**, 730-736 (2005).

43. Toomey, R., Freidank, D. & Ruhe, J. Swelling behavior of thin, surface-attached polymer networks. *Macromolecules* **37**, 882-887 (2004).

44. Moshe, M., Sharon, E. & Kupferman, R. Pattern selection and multiscale behaviour in metrically discontinuous non-euclidean plates. *Nonlinearity* **26**, 3247-3258 (2013).

45. Scarpa, J. S., Mueller, D. D. & Klotz, I. M. Slow hydrogen-deuterium exchange in a non-alpha-helical polyamide. *J Am Chem Soc* **89**, 6024-& (1967).

46. Roy, D., Brooks, W. L. A. & Sumerlin, B. S. New directions in thermoresponsive polymers. *Chem Soc Rev* **42**, 7214-7243 (2013).

47. Călugăreanu, G. L'int´egral de gauss et l'analyse des noeuds tridimensionnels. *Rev. Math. Pures Appl.* **4**, 5-20 (1959).

48. White, J. H. Self-linking and the gauss integral in higher dimensions. *Am. J. Math.* **91**, 693-728 (1969).

49. Fuller, F. B. The writhing number of a space curve. *Proc Natl Acad Sci U S A* **68**, 815-819 (1971).

CHAPTER 6

INTERFACIAL ASSEMBLIES OF PATTERNED GEL SHEETS BY CAPILLARY INTERACTIONS

6.1 Introduction

The interfacial behavior of solid particles at fluid interfaces has been actively studied for many scientific and industrial applications including stabilizers or dispersants in emulsions,[1, 2] coatings[3-5] and flocculants or coagulants in separations.[6] Research in this area has been focused on capillary forces originated from a free energy change owing to the overlap of curved menisci formed around separate particles attached to a fluid interface.[7, 8] While initial studies largely involved interfacial deformation due to buoyancy,[9-11] recent work has focused primarily on the effects of particle geometries and wetting properties.[4, 12-14]

Previous studies have dealt with the assembly of geometrically anisotropic but chemically homogeneous particles at the fluid interfaces.[15-19] The impossibility to satisfy contact angle boundary condition simultaneously with a planar interface results in interfacial deformation; since a particle must be force- and torque-free, the lowest order deformation is quadrupolar. In addition, both chemically and geometrically heterogeneous particles have shown that their orientation strongly depends on the particle surface chemistry, which can dominate the wetting properties at the fluid interface.[20-23] For instance, amphiphilic Janus cylinders adopt a tilted configuration and induce a quasi-quadrupolar or hexapolar interfacial deformation.[21, 22] To date, most reports on the interfacial assembly of anisotropic particles have focused on capillary attraction in the far-

field for microparticles at the fluid interface. Stebe and co-workers have reported capillary interactions between micron-sized corrugated sheets.[24] When the particles were placed at the interface with an undulated contact line with a wavelength smaller than the characteristic dimension of particle, they created capillary repulsion in the near-field. These interactions lead to a strong dependence of assembly behavior on particle shape and interfacial curvature, offering potentially great flexibility in tailoring interfacial particle assemblies.

This chapter focuses on the interfacial assemblies of soft objects due to fluid interface distortions by buckled gel sheets. In chapter 1, we explained the relationship between the elasticity of soft material systems and the interfacial tension of fluid via two dimensionless numbers, C_b and C_s, for micro-scale thin gel sheets. When $C_b \leq 1$ and $C_s >> 1$, it tells us that the surface tension of a fluid can easily bend, but hardly stretch the gel sheets. Kim et al. have previously introduced a method to photolithographically pattern soft hydrogel sheets, and this specifies the Gaussian curvature upon swelling.[25] Here, we choose Enneper's minimal surfaces with zero mean curvature and negative Gaussian curvature to study the interfacial behavior at a fluid interface, and use a modified method employing a digital micromirror device (DMD) for maskless lithography.[26] For the case of photo-patterned gel sheets with zero mean curvature, we expect that interfacial adsorption can hardly make changes in their Gaussian curvature since stretching is more energetically costly than bending for thin sheets.[27, 28] Hence, the interface is deformed according to the Gaussian curvature of the gel sheet, since their swollen shape adopted in water will be maintained at the fluid interface. We utilize this approach to generate multipolar interfacial

deformations and to subsequently fabricate various assembled structures with preferred orientations rather than densely packed or random aggregated structures.

6.2 Experimental

6.2.1 Materials

A photo-crosslinkable, fluorescent, and temperature responsive polymer was synthesized by free-radical polymerization at 80 °C in 1,4-dioxane for 15 h, following three freeze-pump-thaw cycles and a nitrogen purge, with re-crystallized azobisisobutyronitrile (AIBN, Aldrich) as an initiator, as reported previously [25]. The monomer, solvent and initiator concentrations were used as follows: *N*-isopropylacrylamide (NIPAm; 3 g, Tokyo Chemical Industry Co., Ltd), acrylamidobenzophenone (AAmBP; 533 mg), acrylic acid (AAc; 114.5 μL), rhodamine B-labeled methacrylate (RhBMA; 47.6 mg), and AIBN (5 mg), in 30 mL of 1,4-dioxane, resulting in a copolymer with 87.2 mol% NIPAm, 7 mol% AAmBP, 5.5 mol% AAc, and 0.3 mol% RhBMA, as confirmed by ^{1}H NMR (Bruker DPX300). This PNIPAM copolymer was purified by precipitation into stirring diethyl ether, washed by filtration, and dried in a vacuum oven overnight.

6.2.2 Grayscale lithography

To prepare copolymer films, 3 wt% poly(sodium acrylate) (Sigma-Aldrich, M_w = 30 kg/mol) was spin-coated onto a pre-cleaned 1 x 1 cm^2 silicon substrate, yielding a ~ 100 nm thick film. The residual solvent was evaporated on a 150 °C hot plate for 2 h, then the film was soaked in 1.35 M $CaCl_2$ solution for 20 s to form a Ca^{2+}-crosslinked sacrificial layer.[29] A 100 μL drop of copolymer solution in chloroform (1 wt %) was spread on the

sacrificial layer, and the solvent was slowly evaporated for 5 h at 50 °C in a closed glass bottle (0.13 oz capacity glass jar, Freund Container) to yield 8 μm thick films, as measured using a stylus profilometer (Dektak, Veeco).

We employ a maskless grayscale lithographic patterning by using DMD of photo-cross-linkable copolymer films to prepare Enneper's minimal surfaces. To pattern the surfaces, the sample was illuminated with a pattern of UV light (365 nm, pE-100, CoolLED) generated using a DMD (DLP Discovery 4100, 0.7 XGA, Texas Instruments) attached to an inverted optical microscope (Nikon ECLIPSE Ti) with a 10X objective lens (S Fluor, Nikon). We divided the entire range of areal swelling ratio (Ω = 2.1 – 8.4) by 0.42 to generate 16 steps for UV exposure according to the metric of

$$\Omega(r) = c[1 + (r / R)^{2(n-1)}]^2$$

where c is the lowest swelling ratio, 2.1; and R is the outermost radius, 125 μm. To achieve the programmed swelling ratio at certain r, UV exposure time were varied based on the intensity of the UV light source (49 mW/cm^2) measured at 365 nm using Power Meter (PM100USB, Thorlab) and Sensor(S120, Thorlab). After crosslinking the patterns, the film was submerged in a mixture of water and ethanol (1 : 2 by volume) to dissolve uncrosslinked regions, then immersed in an aqueous medium (containing 1 mM NaCl, and 1 mM phosphate buffer, pH 7.2) to dissolve the sacrificial layer and induce swelling of the patterned surfaces.

6.2.3 Characterization

Fluorescence micrographs of Enneper's minimal surfaces were imaged using a laser scanning confocal fluorescence microscope (LSCM) (Zeiss LSM 510 META, 10x objective) or an epi-fluorescence microscope (Nikon ECLIPSE Ti, 4x objective). For LSCM, a HeNe laser (wavelength 543 nm) was used to excite rhodamine B (detection filter: 560 nm), and three-dimensional images were reconstructed from confocal image stacks using ImageJ. Bright field optical micrographs and movies were obtained using a Zeiss Axiovert 200 inverted optical microscope with a 2.5x objective, and a QImaging camera (Retiga-2000R). The height profile of fluid interface was monitored by optical profilometer with a 10x objective (Zygo).

6.3 Results and discussion

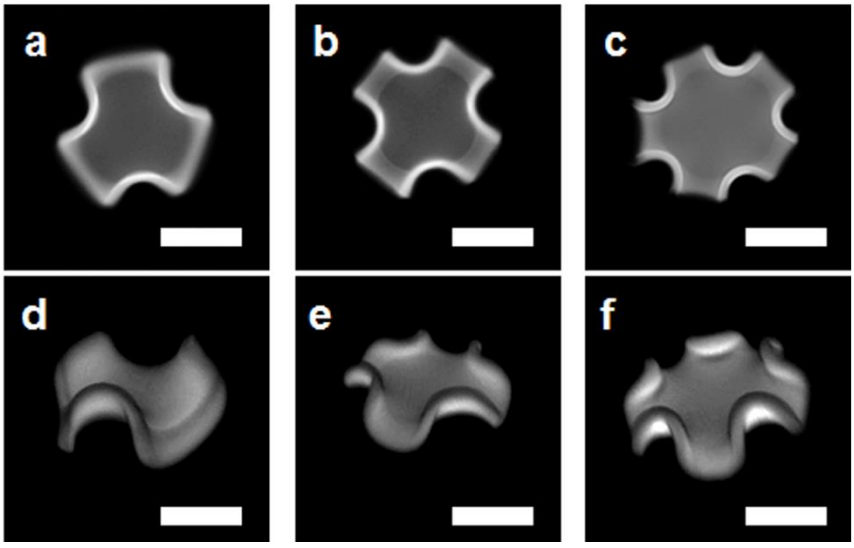

Figure 6.1 (a-c) Fluorescence micrographs and (d-f) three-dimensional LSCM reconstructions of Enneper's minimal surfaces with n = (a, d) 3, (d, e) 4, and (e, f) 5 nodes in swelled state in the aqueous medium. All scale bars are 200 µm.

Patterned gel sheets of Enneper's minimal surfaces buckled into the programmed node number after swelling in an aqueous medium at room temperature. As shown in Figure 6.1, the prepared surfaces have negative Gaussian curvature. During cycles of heating and cooling, these surfaces re-swelled into a consistent number of nodes. The surfaces are nominally programmed to zero mean curvature, but a small mean curvature could be present due to residual stresses from PNIPAM film casting.[30, 31] For the gel sheets with $h \approx 8$ μm, we found that the number of observed nodes saturates after a certain limit in the patterned metric, for instance, for instance, a metric with $n \geq 6$ yields a 6-node configuration for R = 250 um. The number of nodes in the saturation is also strongly dependent on R for Enneper's minimal surfaces.[26]

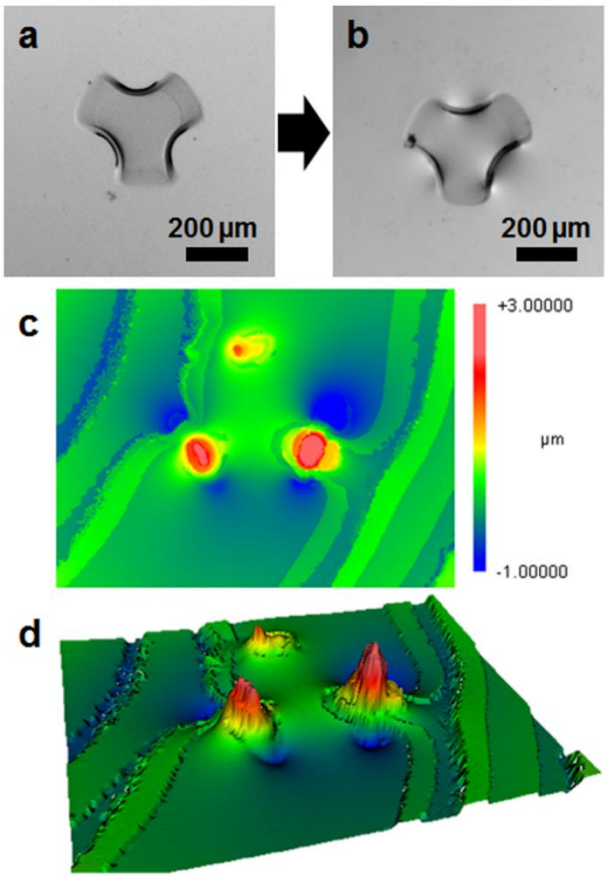

Figure 6.2 Bright field optical micrographs of a swelled Enneper's minimal surface with 3 nodes (a) in the aqueous medium and (b) at the air/aqueous medium interface. (c) Optical profilometry image of interface deformation due to a single Enneper's minimal surface with 3 nodes at the interface of air/aqueous medium, and (d) three-dimensional interface profile.

We first study Enneper's 3-node surface and its capillary assembly of at the fluid interface. As mentioned in Introduction (chapter 6.1), by considering a characteristic fluid surface tension $\gamma \sim 10$ mN/m, we can estimate the two elasto-capillary numbers $C_s \sim 10^2$, and $C_b \sim 1$ for $E \sim 10^5$ Pa, $h \sim 10$ µm and $R \sim 100$ µm. The two dimensionless numbers demonstrate that these buckled hydrogel thin sheets cannot be stretched by surface tension ($C_s >> 1$), but they can be bent ($C_b \sim 1$). Hence, when the fully swelled 3-nodes surface is placed at the interface between air and an aqueous medium, the buckled surface effectively

deforms the interfacial profile depending on its curved shape (i.e., Gaussian curvature) rather than flattening. Therefore, deformed menisci give rise to long-range capillary interactions between the surfaces (Figure 6.2a-b).

Optical profilometry images show interesting interfacial deformations by a single 3-node surface (Figure 6.2c-d). The interfacial profiles indicate that one node induces one positive (i.e., crest) and two smaller negative deformations (i.e., troughs). Thus, a 3-node surface gives rise to quasi-hexapolar interface deformation, and the magnitude of the positive deformations are approximately 3-4 times larger than the negative deformations. We note that some irregular lines on the surface of aqueous medium come from small but inevitable fluctuations of fluid surface owing to fluid evaporations and external vibrations during the imaging. To obtain a clean image from profilometry, the fluid medium should be solidified or changed to more viscous fluids; however, that causes changes in surface tension, viscosity of the fluid, and swelling conditions of gel sheets.

Capillary assembly between 3-node surfaces shows crest-to-crest alignment dominantly rather than trough-to-trough orientation as seen in Figure 6.3a. Profilometry image analysis proves the strong capillary interactions arise from the positive deformations, and this preferred crest-to-crest orientation can be explained by the magnitude differences of induced deformation (Figure 6.3b-c). When 3-node surfaces approach each other in directions of non-positive interface deformation, they initially have negative-to-negative alignment, but quickly rotate and rearrange themselves due to the stronger crest-to-crest interactions (Figure 6.4). Notably, by comparing Figure 6.3b with Figure 6.2c, profilometry images show no significant changes in magnitudes of negative and positive interfacial deformations after assembly. This fact allows us to extend the

assembled structure by capillary interactions by using multiple gel sheets with consistent preferred alignment. For example, the interfacial deformation of 3-node surfaces produce quasi-hexapolar configuration, wherein each 3-node surface could have three neighbors with crest-to-crest orientation. We expect that this alignment on a large number of 3-nodes surfaces can form a two-dimensional open hexagonal structure owing to strong lateral capillary interactions.

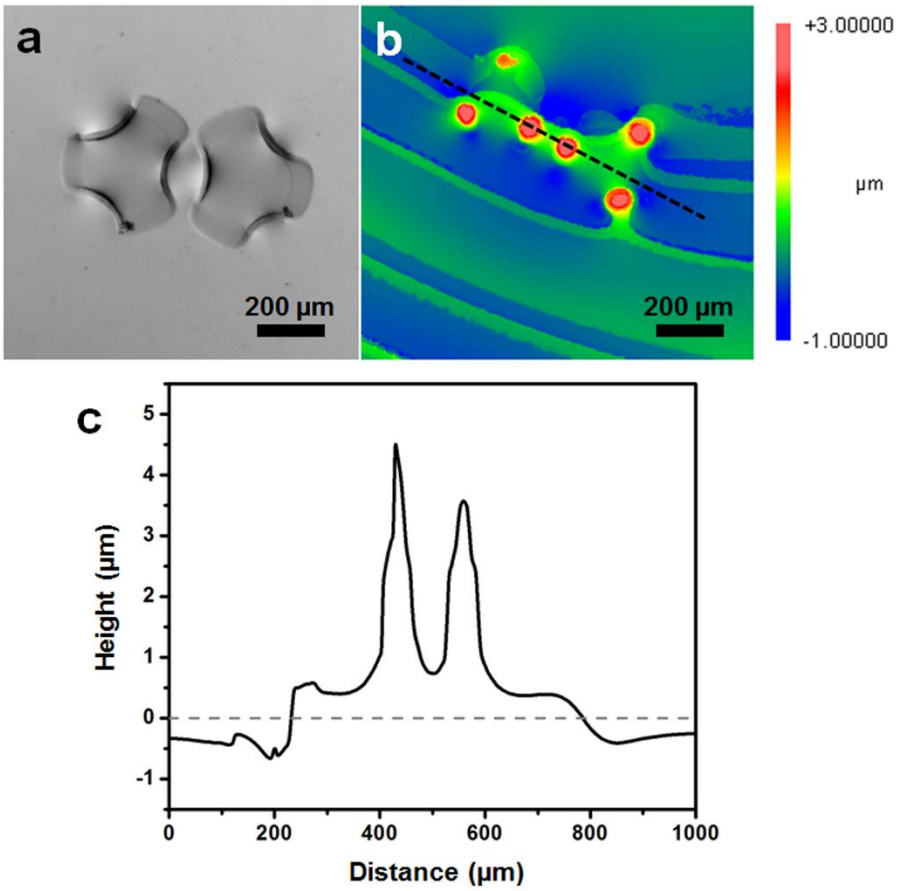

Figure 6.3 Capillary interaction and interface deformation between patterned hydrogel sheets. (a) Bright field optical micrograph and (b) optical profilometry image of assembled two of 3-nodes Enneper's minimal surfaces at the air/aqueous medium interface due to capillary interactions. (c) Cross-sectional height profile of the interface deformation corresponding to the black dashed line in (b).

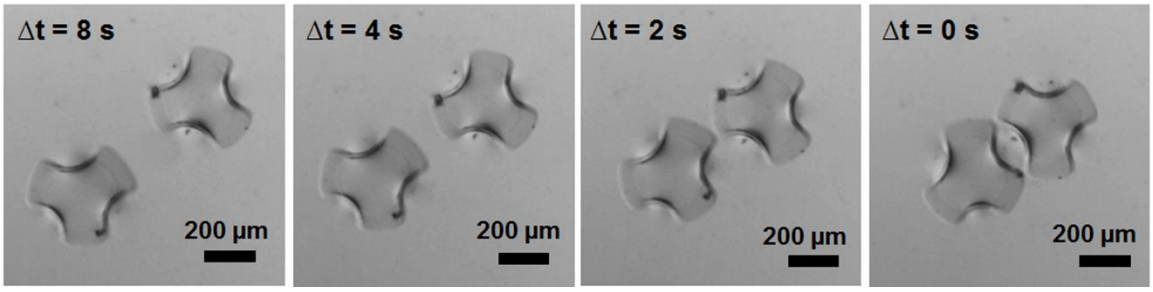

Figure 6.4 Bright field optical micrograph images of capillary interactions between two of 3-nodes Enneper's minimal surfaces at the air/aqueous medium interface. When the gel sheets initially approach in trough-to trough alignment then rearrange themselves to crest-to-crest alignment.

Here, by assuming negligible thermal and inertial forces in the low Reynolds number limit, the approach velocity of two surfaces can be used to directly infer the distance dependence of the interaction potential. Thus, the lateral capillary interaction force (F) and Stokes' drag force (F_{drag}) are in a linear relationship ($F \sim - F_{drag}$), and the pair potential can be described as a function of the separation distance, $U \sim r^{\beta}$ with $\beta = 2 - 1/\alpha < 0$.[20]

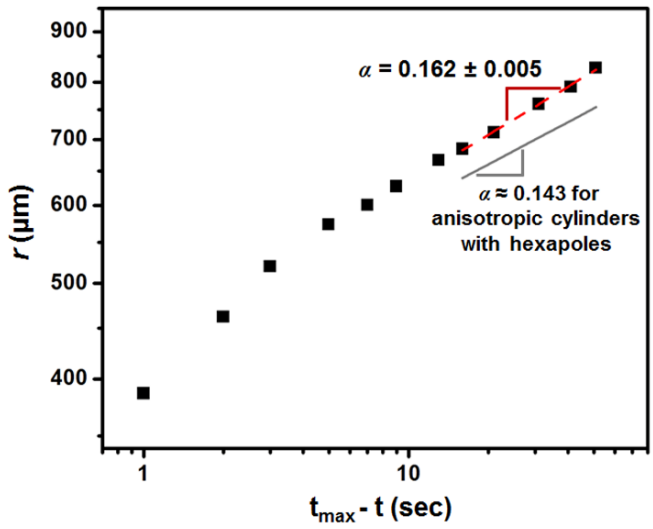

Figure 6.5 Center-to-center separation distance, r, between two 3-nodes Enneper's minimal surfaces at the air/aqueous medium interface as a function of time, $t_{max} - t$. Logarithmic scales are used for both axes, and a best-fit slope of 0.162 ± 0.005 of the plot is drawn as a dashed line. As a comparison, the interfacial behavior of hexapolar interface deformation with geometrically and chemically anisotropic solid cylinders is described by the smaller exponent $\alpha \approx 0.143$.

To understand the attractive capillary interaction between 3-node surfaces of soft objects, we observed their interfacial behaviors by optical microscopy as a direct measurement of interactions. We recorded the motion of two interacting 3-node surfaces in real time. From this series of images, we characterized the center-to-center separation (r) between two approaching objects as a function of time (t). We plot r against (t_{max} - t) on a log-log scale, where t_{max} is the time the objects come into contact. This data set exhibits a power law behavior $r = (t_{max} - t)^{\alpha}$ with a best-fit slope of 0.162 ± 0.005 in the long distance asymptotic regime,[32] corresponding to $r / 2R_{swell} > 1.5$, where the swelled radius of Enneper's minimal surface, R_{swell}, is 200 μm (Figure 6.5). Consequently, the pair interaction potential for 3-node surfaces is explained by $U \sim r^{-4}$. Recently, Park et al. reported that hexapolar interface deformations induced by tilted amphiphilic cylinders

exhibit the scaling behavior for end-to-end interactions $U \sim r^{-5}$.[21, 33] Our observed power law ($\beta \approx$ - 4) for quasi-hexapolar interface deformation between soft objects is much slower than the cases of hexapolar capillary interactions between anisotropic rigid particles ($U \sim r^{-5}$) as well as spherical particles ($U \sim r^{-6}$).[32] Interestingly, the $U \sim r^{-4}$ dependence is in good agreement with the power law behavior of quadrupolar capillary interactions between homogeneous ellipsoids: $\beta \approx$ - 3 for side-to-side alignment and $\beta \approx$ – 4 for tip-to-tip alignment.[17, 20] This result suggest that the capillary interaction between objects is dictated by local interfacial deformation around the approach direction rather than interfacial deformation of the entire object.[34] As shown in Figure 6.2c and 6.3b, one node in a 3 node Enneper's minimal surface generates one positive deformation and two smaller negative deformations that closely resemble one tip of quadrupolar interface deformation.

6.4 Conclusions

In conclusion, we have investigated the interfacial behavior of sub-millimeter soft objects with non-zero Gaussian curvature and zero mean curvature that are able to deform the fluid interface to conform to their curvature based on a balance between elastic and surface energies. By using the prepared Enneper's surfaces with 3-nodes via gray scale lithography, we have explored how the programmed Gaussian curvature generates the deformation of a flat interfacial profile, and how the induced interfacial deformation can drive their assembly. Notably, a 3 node Enneper's minimal surface can effectively deform the fluid interface, and this result is in excellent agreement with our calculation for dimensionless numbers, C_b~1 and C_s ~100, for the given conditions. Buckled gel sheets

with a 3-node induced quasi-hexapolar interfacial deformation, and generated strong lateral capillary interactions between them. However, the power law behavior of the pair interaction potential is consistent with the case of quadrupolar interfacial deformation. In future work, we will utilize Enneper's minimal surfaces with different nodes to generate multi-polar interface deformation, and study their interfacial behavior. Furthermore, the temperature-responsiveness of our PNIPAM based surfaces can be harnessed for thermally switchable capillary assembly.

6.5 References

1. Pickering, S. U. Cxcvi.-emulsions. *Journal of the Chemical Society, Transactions* **91**, 2001-2021 (1907).

2. Binks, B. P. Particles as surfactants—similarities and differences. *Curr Opin Colloid In* **7**, 21-41 (2002).

3. Park, J. & Moon, J. Control of colloidal particle deposit patterns within picoliter droplets ejected by ink-jet printing. *Langmuir* **22**, 3506-3513 (2006).

4. Yunker, P. J., Still, T., Lohr, M. A. & Yodh, A. G. Suppression of the coffee-ring effect by shape-dependent capillary interactions. *Nature* **476**, 308-311 (2011).

5. Shmuylovich, L., Shen, A. Q. & Stone, H. A. Surface morphology of drying latex films: Multiple ring formation. *Langmuir* **18**, 3441-3445 (2002).

6. Ramsden, W. Separation of solids in the surface-layers of solutions and 'suspensions' (observations on surface-membranes, bubbles, emulsions, and mechanical coagulation). -- preliminary account. *Proceedings of the Royal Society of London* **72**, 156-164 (1903).

7. Kralchevsky, P. A. & Nagayama, K. Capillary interactions between particles bound to interfaces, liquid films and biomembranes. *Adv Colloid Interfac* **85**, 145-192 (2000).

8. Kralchevsky, P. A. & Denkov, N. D. Capillary forces and structuring in layers of colloid particles. *Curr Opin Colloid In* **6**, 383-401 (2001).

9. Bowden, N., Choi, I. S., Grzybowski, B. A. & Whitesides, G. M. Mesoscale self-assembly of hexagonal plates using lateral capillary forces: Synthesis using the "capillary bond". *Journal of the American Chemical Society* **121**, 5373-5391 (1999).

10. Petkov, J. T., Gurkov, T. D. & Campbell, B. E. Measurement of the yield stress of gellike protein layers on liquid surfaces by means of an attached particle. *Langmuir* **17**, 4556-4563 (2001).

11. Nicolson, M. M. The interaction between floating particles. *P Camb Philos Soc* **45**, 288-295 (1949).

12. Botto, L., Lewandowski, E. P., Cavallaro, M. & Stebe, K. J. Capillary interactions between anisotropic particles. *Soft Matter* **8**, 9957-9971 (2012).

13. Brown, A. B. D., Smith, C. G. & Rennie, A. R. Fabricating colloidal particles with photolithography and their interactions at an air-water interface. *Physical Review E* **62**, 951-960 (2000).

14. Bowden, N., Arias, F., Deng, T. & Whitesides, G. M. Self-assembly of microscale objects at a liquid/liquid interface through lateral capillary forces. *Langmuir* **17**, 1757-1765 (2001).

15. Cavallaro, M., Botto, L., Lewandowski, E. P., Wang, M. & Stebe, K. J. Curvature-driven capillary migration and assembly of rod-like particles. *P Natl Acad Sci USA* **108**, 20923-20928 (2011).

16. Lewandowski, E. P., Bernate, J. A., Tseng, A., Searson, P. C. & Stebe, K. J. Oriented assembly of anisotropic particles by capillary interactions. *Soft Matter* **5**, 886-890 (2009).

17. Lewandowski, E. P., Cavallaro, M., Botto, L., Bernate, J. C., Garbin, V. & Stebe, K. J. Orientation and self-assembly of cylindrical particles by anisotropic capillary interactions. *Langmuir* **26**, 15142-15154 (2010).

18. Lewandowski, E. P., Searson, P. C. & Stebe, K. J. Orientation of a nanocylinder at a fluid interface. *J Phys Chem B* **110**, 4283-4290 (2006).

19. Stebe, K. J. & Lewandowski, E. P. Coll 66-oriented assembly of anisotropic particles by capillary interactions. *Abstr Pap Am Chem S* **238**, (2009).

20. Loudet, J. C., Alsayed, A. M., Zhang, J. & Yodh, A. G. Capillary interactions between anisotropic colloidal particles. *Phys Rev Lett* **94**, (2005).

21. Park, B. J., Choi, C.-H., Kang, S.-M., Tettey, K. E., Lee, C.-S. & Lee, D. Geometrically and chemically anisotropic particles at an oil-water interface. *Soft Matter* **9**, 3383-3388 (2013).

22. Park, B. J., Choi, C.-H., Kang, S.-M., Tettey, K. E., Lee, C.-S. & Lee, D. Double hydrophilic janus cylinders at an air–water interface. *Langmuir* **29**, 1841-1849 (2013).

23. Rezvantalab, H. & Shojaei-Zadeh, S. Role of geometry and amphiphilicity on capillary-induced interactions between anisotropic janus particles. *Langmuir* **29**, 14962-14970 (2013).

24. Yao, L., Botto, L., Cavallaro, J. M., Bleier, B. J., Garbin, V. & Stebe, K. J. Near field capillary repulsion. *Soft Matter* **9**, 779-786 (2013).

25. Kim, J., Hanna, J. A., Byun, M., Santangelo, C. D. & Hayward, R. C. Designing responsive buckled surfaces by halftone gel lithography. *Science* **335**, 1201-1205 (2012).

26. Na, J.-H. & Hayward, R. C. *in preparation*.

27. Sharon, E. & Efrati, E. The mechanics of non-euclidean plates. *Soft Matter* **6**, 5693-5704 (2010).

28. Efrati, E., Sharon, E. & Kupferman, R. Buckling transition and boundary layer in non-euclidean plates. *Phys Rev E* **80**, (2009).

29. Linder, V., Gates, B. D., Ryan, D., Parviz, B. A. & Whitesides, G. M. Water-soluble sacrificial layers for surface micromachining. *Small* **1**, 730-736 (2005).

30. Kim, S. H. *et al.* Synthesis and assembly of colloidal particles with sticky dimples. *Journal of the American Chemical Society* **134**, 16115-16118 (2012).

31. Bae, J., Na, J.-H., Santangelo, C. D. & Hayward, R. C. Edge-defined metric buckling of temperature-responsive hydrogel ribbons and rings. *Polymer* **55**, 5908-5914 (2014).

32. Danov, K. D., Kralchevsky, P. A., Naydenov, B. N. & Brenn, G. Interactions between particles with an undulated contact line at a fluid interface: Capillary multipoles of arbitrary order. *Journal of Colloid and Interface Science* **287**, 121-134 (2005).

33. Park, B. J., Choi, C.-H., Kang, S.-M., Tettey, K. E., Lee, C.-S. & Lee, D. Double hydrophilic janus cylinders at an air–water interface. *Langmuir*, (2013).

34. Kang, S.-M. *et al*. Triblock cylinders at fluid–fluid interfaces. *Langmuir* **30**, 13199-13204 (2014).

CHAPTER 7

CONCLUSIONS

The aim of this dissertation is to investigate aspects of the assembly and deformation of amphiphilic copolymers and copolymer networks as nanometer and micrometer length-scale objects at fluid interfaces, respectively. When sub-millimeter sized objects adsorb at the fluid interface, the surface energy is dominant over both gravitational and thermal energies. Moreover, surface energy of the fluid is comparable to bending energy of micron-sized elastic gel sheets. Therefore, the surface tension can provide a new means to assemble and deform soft elastic objects in sub-millimeter scales as well as to characterize their elastic properties.

Utilizing amphiphilic block copolymers, we have introduced emulsion processing—evaporation-triggered instabilities at the interface of an organic solvent droplet and water—to efficiently co-encapsulate pre-synthesized hydrophobic nano-spheres and –rods into different morphologies of amphiphilic block copolymer assemblies. This work provides a simple but powerful route to prepare multifunctional polymer micelles with no sensitivity to size, shape, and chemistry of nanoparticles.

Next, a novel one-step method for the formation of water-in-oil-in-water double emulsions with excellent stability has been developed. This phenomenon is based on spontaneously formed micron-sized water droplets near the interface between the organic solvent containing polymer-salt aggregates and water due to the osmotic driving force. We have tuned the structure and size of the double emulsions by manipulating the osmotic pressure against Laplace pressure. Furthermore, these highly stable double emulsions were

converted to multi-compartment polymer capsules with encapsulated species, and a similar effect was also used to obtain hierarchically structured porous polymer films.

We have taken advantage of photo-crosslinkable and temperature-responsive copolymer networks—simple patterning to desired shape and size, mechanical property tuning by degree of crosslinking, and temperature—to understand correlations between fluid surface energy and elastic energy to bend or stretch thin gel sheets. To better understand the given soft material system, we have developed an elasto-capillary bending approach to quantitatively measure elastic moduli of micron sized thin samples in liquid media based on the balance between bending rigidity and surface tension. Using this method, we successfully characterized stiff glassy polymer films (elastic modulus ~ GPa) and soft hydrogels (kPa – MPa). Moreover, this method allowed us to characterize the power law dependence of swelling ratio of and elastic modulus for a polyelectrolyte gel.

Surface tension has been harnessed as a probe for edge metric imperfections by observation of interfacial deformation of fully and homogeneously crosslinked gel ribbons at the fluid interface. The deformed shape at the fluid interface implies that there are differences in swelling ratio through the width of ribbons. Edge-metric imperfections occur due to a limited spatial resolution of the photo-lithographic patterning. These imperfections were utilized to drive buckling of narrow strips and rings, and eventually used as a simple experimental approach to fabricate shape-morphing structures.

Lastly, we have investigated the interfacial assembly behaviors of micron sized soft objects with non-zero Gaussian curvature and zero mean curvature that are able to deform the fluid interface to conform to their curvature based on the balance between elastic and surface energies. We have shown that Enneper's minimal surfaces with 3-nodes induce

multi-polar interface deformation and that gives rise to strong capillary interactions between them. Interestingly, their capillary interaction potential exhibits a scaling behavior similar with chemically homogeneous ellipsoids. For further study, we are interested in interfacial assemblies by utilizing Enneper's minimal surfaces with different nodes ($n > 3$), and a switchable interfacial assembly system by turning-off and -on the strong capillary interactions by heating and cooling, respectively.

This thesis could trigger deeper studies about the important role of surface tension to assemble and deform soft materials at small scales. The fluid interface can effectively deform the shape of sub-millimeter sized soft materials; or inversely, the interface can be deformed by the shape of soft objects depending on their dimensions and elastic modulus. Thus, this field has many remaining questions surrounding the interfacial behaviors of soft-objects at the interface, since previous studies have mostly focused on the interfacial behaviors of rigid objects. We expect that strong capillary interactions will be a promising means for the assembly of open structures, orienting and positioning of soft objects.

Last but not least, we address the promising and interesting directions of related studies. The former part of this thesis has shown that the amphiphilic block copolymer assemblies via an emulsification process can be a very promising way to prepare exotic and hierarchical structures, because emulsions serve as a powerful template for copolymer assembly. While this field has been studied for several decades, the research about *non-classical* behaviors needs further exploration. Here, we have utilized the interfacial instabilities and osmotic stresses to induce new phenomenon; these non-classical pathways may be able to solve the remaining issues. Future works could be: 1) formation of non-spherical shape (i.e., low curvature) of emulsions via extremely low interfacial tension

between organic solvent including block copolymer droplets in an aqueous phase, and 2) the use of stimuli-responsive block copolymers as surface active agents could actuate emulsification or de-emulsification by external stimuli such as temperature, pH, ionic strength and light.

This elasto-capillary bending method has successfully characterized the elastic modulus of stiff to soft materials on the micrometer scale. Here, the interesting but unexplored parts are 1) the use of various geometries of polymer sheets including ribbons (rectangular shape) with different aspect ratios and circles, 2) characterization of anisotropic properties of a polymer sheet by elasto-capillary bending behaviors, 3) characterization of modulus of stimuli-responsive materials under different conditions of external stimuli, and 4) extension to characterization of other types of materials including 2D sheets such as graphene or transition metal dichalcogenides.

In chapter 6, we introduced interfacial assembly of a buckled soft sheet (i.e., 3-node Enneper's minimal surfaces) and that capillary interactions stem from interface deformation according to the buckled configuration. In addition to the mentioned future directions, control over capillary flattening of bendable structures (e.g., self-folded origami) by adjusting the effective surface tension could be a promising method to characterize mechanical properties of such structures.

BIBLIOGRAPHY

Alben, S., B. Balakrisnan and E. Smela (2011). "Edge Effects Determine the Direction of Bilayer Bending." Nano Lett **11**(6): 2280-2285.

Alonso, J. L. and W. H. Goldmann (2003). "Feeling the forces: atomic force microscopy in cell biology." Life Sci **72**(23): 2553-2560.

Armon, S., E. Efrati, R. Kupferman and E. Sharon (2011). "Geometry and Mechanics in the Opening of Chiral Seed Pods." Science **333**(6050): 1726-1730.

Aserin, A. (2008). Multiple Emulsion: Technology and Applications, Wiley.

Bae, J., J.-H. Na, C. D. Santangelo and R. C. Hayward (2014). "Edge-defined metric buckling of temperature-responsive hydrogel ribbons and rings." Polymer **55**(23): 5908-5914.

Bae, Y. and K. Kataoka (2009). "Intelligent polymeric micelles from functional poly(ethylene glycol)-poly(amino acid) block copolymers." Adv Drug Deliver Rev **61**(10): 768-784.

Bende, N. P., R. C. Hayward and C. D. Santangelo (2014). "Nonuniform growth and topological defects in the shaping of elastic sheets." Soft Matter **In press**

Besnard, L., F. Marchal, J. F. Paredes, J. Daillant, N. Pantoustier, P. Perrin and P. Guenoun (2013). "Multiple Emulsions Controlled by Stimuli-Responsive Polymers." Advanced Materials **25**(20): 2844-2848.

Bibette, J., F. L. Calderon and P. Poulin (1999). "Emulsions: basic principles." Rep Prog Phys **62**(6): 969-1033.

Bico, J., B. Roman, L. Moulin and A. Boudaoud (2004). "Elastocapillary coalescence in wet hair." Nature **432**(7018): 690-690.

Binks, B. P. (2002). "Particles as surfactants—similarities and differences." Current Opinion in Colloid & Interface Science **7**(1–2): 21-41.

Blanazs, A., S. P. Armes and A. J. Ryan (2009). "Self-Assembled Block Copolymer Aggregates: From Micelles to Vesicles and their Biological Applications." Macromolecular Rapid Communications **30**(4-5): 267-277.

Bonnet, M., M. Cansell, F. Placin, E. David-Briand, M. Anton and F. Leal-Calderon (2010). "Influence of Ionic Complexation on Release Rate Profiles from Multiple Water-in-Oil-in-Water (W/O/W) Emulsions." J Agr Food Chem **58**(13): 7762-7769.

Bose, S. and S. K. Saha (2003). "Synthesis and Characterization of Hydroxyapatite Nanopowders by Emulsion Technique." Chemistry of Materials **15**(23): 4464-4469.

Botto, L., E. P. Lewandowski, M. Cavallaro and K. J. Stebe (2012). "Capillary interactions between anisotropic particles." Soft Matter **8**(39): 9957-9971.

Bowden, N., F. Arias, T. Deng and G. M. Whitesides (2001). "Self-assembly of microscale objects at a liquid/liquid interface through lateral capillary forces." Langmuir **17**(5): 1757-1765.

Bowden, N., I. S. Choi, B. A. Grzybowski and G. M. Whitesides (1999). "Mesoscale Self-Assembly of Hexagonal Plates Using Lateral Capillary Forces: Synthesis Using the "Capillary Bond"." J Am Chem Soc **121**(23): 5373-5391.

Brandrup, J. I. E. H. (1989). Polymer handbook. New York, Wiley.

Brown, A. B. D., C. G. Smith and A. R. Rennie (2000). "Fabricating colloidal particles with photolithography and their interactions at an air-water interface." Phys Rev E **62**(1): 951-960.

Browning, N. D., M. F. Chisholm and S. J. Pennycook (1993). "Atomic-Resolution Chemical-Analysis Using a Scanning-Transmission Electron-Microscope." Nature **366**(6451): 143-146.

Bunz, U. H. F. (2006). "Breath figures as a dynamic templating method for polymers and nanomaterials." Advanced Materials **18**(8): 973-989.

Byun, M., C. D. Santangelo and R. C. Hayward (2013). "Swelling-driven rolling and anisotropic expansion of striped gel sheets." Soft Matter **9**(34): 8264-8273.

Cai, S. S., K. Vijayan, D. Cheng, E. M. Lima and D. E. Discher (2007). "Micelles of different morphologies - Advantages of worm-like filomicelles of PEO-PCL in paclitaxel delivery." Pharm Res **24**(11): 2099-2109.

Călugăreanu, G. (1959). "L'int´egral de Gauss et l'analyse des noeuds tridimensionnels." Rev. Math. Pures Appl. **4**: 5-20.

Cavallaro, M., L. Botto, E. P. Lewandowski, M. Wang and K. J. Stebe (2011). "Curvature-driven capillary migration and assembly of rod-like particles." P Natl Acad Sci USA **108**(52): 20923-20928.

Chakrapani, N., B. Q. Wei, A. Carrillo, P. M. Ajayan and R. S. Kane (2004). "Capillarity-driven assembly of two-dimensional cellular carbon nanotube foams." P Natl Acad Sci USA **101**(12): 4009-4012.

Chakravarti, A. K., S. B. Chowdhury, S. Chakrabarty, T. Chakrabarty and D. C. Mukherjee (1995). "Liquid membrane multiple emulsion process of chromium(VI) separation from waste waters." Colloids and Surfaces A: Physicochemical and Engineering Aspects **103**(1–2): 59-71.

Chen, B. G. G. and C. D. Santangelo (2010). "Minimal resonances in annular non-Euclidean strips." Phys Rev E **82**(5).

Chen, D., J. Yoon, D. Chandra, A. J. Crosby and R. C. Hayward (2014). "Stimuli-responsive buckling mechanics of polymer films." Journal of Polymer Science Part B: Polymer Physics **52**(22): 1441-1461.

Chen, X. and J. Yin (2010). "Buckling patterns of thin films on curved compliant substrates with applications to morphogenesis and three-dimensional micro-fabrication." Soft Matter **6**(22): 5667-5680.

Chiappelli, M. C. and R. C. Hayward (2012). "Photonic Multilayer Sensors from Photo-Crosslinkable Polymer Films." Advanced Materials **24**(45): 6100-+.

Chin, M. S., B. B. Freniere, S. Fakhouri, J. E. Harris, J. F. Lalikos and A. J. Crosby (2013). "Cavitation Rheology as a Potential Method for In Vivo Assessment of Skin Biomechanics." Plast Reconstr Surg **131**(2): 303e-305e.

Choi, S.-W., Y. Zhang and Y. Xia (2009). "Fabrication of Microbeads with a Controllable Hollow Interior and Porous Wall Using a Capillary Fluidic Device." Advanced Functional Materials **19**(18): 2943-2949.

Christensen, S. K., M. C. Chiappelli and R. C. Hayward (2012). "Gelation of Copolymers with Pendent Benzophenone Photo-Cross-Linkers." Macromolecules **45**(12): 5237-5246.

Chu, L. Y., A. S. Utada, R. K. Shah, J. W. Kim and D. A. Weitz (2007). "Controllable monodisperse multiple emulsions." Angew Chem Int Edit **46**(47): 8970-8974.

Cozzoli, P. D., T. Pellegrino and L. Manna (2006). "Synthesis, properties and perspectives of hybrid nanocrystal structures." Chem Soc Rev **35**(11): 1195-1208.

Cui, J., C. H. Lee, A. Delbos, J. J. McManus and A. J. Crosby (2011). "Cavitation rheology of the eye lens." Soft Matter **7**(17): 7827-7831.

Dams, S. S. and I. M. Walker (1987). [5] Multiple emulsions as targetable delivery systems. Methods in Enzymology. K. J. W. Ralph Green, Academic Press. **Volume 149:** 51-64.

Danov, K. D., P. A. Kralchevsky, B. N. Naydenov and G. Brenn (2005). "Interactions between particles with an undulated contact line at a fluid interface: Capillary multipoles of arbitrary order." Journal of Colloid and Interface Science **287**(1): 121-134.

de Gennes, P. G., F. Brochard-Wyart and D. Quere (2003). Capillarity and Wetting Phenomena: Drops, Bubbles, Pearls, Waves, Springer.

de Haan, L. T., V. Gimenez-Pinto, A. Konya, T.-S. Nguyen, J. M. N. Verjans, C. Sánchez-Somolinos, J. V. Selinger, R. L. B. Selinger, D. J. Broer and A. P. H. J. Schenning (2014). "Accordion-like Actuators of Multiple 3D Patterned Liquid Crystal Polymer Films." Advanced Functional Materials **24**(9): 1251-1258.

de Haan, L. T., C. Sanchez-Somolinos, C. M. W. Bastiaansen, A. P. H. J. Schenning and D. J. Broer (2012). "Engineering of Complex Order and the Macroscopic Deformation of Liquid Crystal Polymer Networks." Angew Chem Int Edit **51**(50): 12469-12472.

de Langre, E., C. N. Baroud and P. Reverdy (2010). "Energy criteria for elasto-capillary wrapping." J Fluid Struct **26**(2): 205-217.

Demichelis, A., S. Pavarelli, L. Mortati, G. Sassi and M. Sassi (2013). "Study on the AFM Force Spectroscopy method for elastic modulus measurement of living cells." J Phys Conf Ser **459**.

Dervaux, J. and M. Ben Amar (2008). "Morphogenesis of growing soft tissues." Physical Review Letters **101**(6).

Di Corato, R., N. C. Bigall, A. Ragusa, D. Dorfs, A. Genovese, R. Marotta, L. Manna and T. Pellegrino (2011). "Multifunctional Nanobeads Based on Quantum Dots and Magnetic Nanoparticles: Synthesis and Cancer Cell Targeting and Sorting." Acs Nano **5**(2): 1109-1121.

Dias, M. A., J. A. Hanna and C. D. Santangelo (2011). "Programmed buckling by controlled lateral swelling in a thin elastic sheet." Phys Rev E **84**(3).

Djalali, R., S. Y. Li and M. Schmidt (2002). "Amphipolar core-shell cylindrical brushes as templates for the formation of gold clusters and nanowires." Macromolecules **35**(11): 4282-4288.

Drira, Z. and V. K. Yadavalli (2013). "Nanomechanical measurements of polyethylene glycol hydrogels using atomic force microscopy." Journal of the Mechanical Behavior of Biomedical Materials **18**(0): 20-28.

Du, B., O. K. C. Tsui, Q. Zhang and T. He (2001). "Study of Elastic Modulus and Yield Strength of Polymer Thin Films Using Atomic Force Microscopy." Langmuir **17**(11): 3286-3291.

Dubrovskii, S. A. and G. V. Rakova (1997). "Elastic and osmotic behavior and network imperfections of nonionic and weakly ionized acrylamide-based hydrogels." Macromolecules **30**(24): 7478-7486.

Dunlop, J. W. C., R. Weinkamer and P. Fratzl (2011). "Artful interfaces within biological materials." Mater Today **14**(3): 70-78.

Ebenstein, D. M. and L. A. Pruitt (2006). "Nanoindentation of biological materials." Nano Today **1**(3): 26-33.

Efrati, E., E. Sharon and R. Kupferman (2009). "Buckling transition and boundary layer in non-Euclidean plates." Phys Rev E **80**(1).

Efrati, E., E. Sharon and R. Kupferman (2009). "Elastic theory of unconstrained non-Euclidean plates." J Mech Phys Solids **57**(4): 762-775.

Efrati, E., E. Sharon and R. Kupferman (2011). "Hyperbolic non-Euclidean elastic strips and almost minimal surfaces." Phys Rev E **83**(4).

Erb, R. M., J. S. Sander, R. Grisch and A. R. Studart (2013). "Self-shaping composites with programmable bioinspired microstructures." Nat Commun **4**: 1712.

Evans, E. A., R. Waugh and L. Melnik (1976). "Elastic Area Compressibility Modulus of Red-Cell Membrane." Biophys J **16**(6): 585-595.

Fernandes, R. and D. H. Gracias (2012). "Self-folding polymeric containers for encapsulation and delivery of drugs." Advanced Drug Delivery Reviews **64**(14): 1579-1589.

Ficheux, M. F., L. Bonakdar, F. Leal-Calderon and J. Bibette (1998). "Some stability criteria for double emulsions." Langmuir **14**(10): 2702-2706.

Florence, A. T. and D. Whitehill (1982). "The Formulation and Stability of Multiple Emulsions." International Journal of Pharmaceutics **11**(4): 277-308.

Fuks, G., R. M. Talom and F. Gauffre (2011). "Biohybrid block copolymers: towards functional micelles and vesicles." Chem Soc Rev **40**(5): 2475-2493.

Fuller, F. B. (1971). "The writhing number of a space curve." Proc Natl Acad Sci U S A **68**(4): 815-819.

Gallarate, M., M. E. Carlotti, M. Trotta and S. Bovo (1999). "On the stability of ascorbic acid in emulsified systems for topical and cosmetic use." International Journal of Pharmaceutics **188**(2): 233-241.

Garamszegi, L., C. Donzel, G. Carrot, T. Q. Nguyen and J. Hilborn (2003). "Synthesis of thiol end-functional polystyrene via atom transfer radical polymerization." React Funct Polym **55**(2): 179-183.

Garti, N. (1997). "Double emulsions - Scope, limitations and new achievements." Colloid Surface A **123**: 233-246.

Gemmer, J. and S. C. Venkataramani (2013). "Shape transitions in hyperbolic non-Euclidean plates." Soft Matter **9**(34): 8151-8161.

Geng, K. B., F. Q. Yang, T. Druffel and E. A. Grulke (2005). "Nanoindentation behavior of ultrathin polymeric films." Polymer **46**(25): 11768-11772.

Geng, Y., P. Dalhaimer, S. S. Cai, R. Tsai, M. Tewari, T. Minko and D. E. Discher (2007). "Shape effects of filaments versus spherical particles in flow and drug delivery." Nat Nanotechnol **2**(4): 249-255.

Geryak, R. and V. V. Tsukruk (2014). "Reconfigurable and actuating structures from soft materials." Soft Matter **10**(9): 1246-1263.

Gohy, J. F. (2005). "Block copolymer micelles." Adv Polym Sci **190**: 65-136.

Gracias, D. H. (2013). "Stimuli responsive self-folding using thin polymer films." Current Opinion in Chemical Engineering **2**(1): 112-119.

Gu, H. W., R. K. Zheng, X. X. Zhang and B. Xu (2004). "Facile one-pot synthesis of bifunctional heterodimers of nanoparticles: A conjugate of quantum dot and magnetic nanoparticles." J Am Chem Soc **126**(18): 5664-5665.

Gu, Z., A. Biswas, M. X. Zhao and Y. Tang (2011). "Tailoring nanocarriers for intracellular protein delivery." Chem Soc Rev **40**(7): 3638-3655.

Guo, X. Y., H. Li, B. Y. Ahn, E. B. Duoss, K. J. Hsia, J. A. Lewis and R. G. Nuzzo (2009). "Two- and three-dimensional folding of thin film single-crystalline silicon for photovoltaic power applications." P Natl Acad Sci USA **106**(48): 20149-20154.

Gupta, S., T. Greeshma, B. Basu, S. Goswami and A. Sinha (2013). "Stiffness- and wettability-dependent myoblast cell compatibility of transparent poly(vinyl alcohol) hydrogels." J Biomed Mater Res B **101B**(2): 346-354.

Hager, W. H. (2012). "Wilfrid Noel Bond and the Bond number." Journal of Hydraulic Research **50**(1): 3-9.

Hammond, P. T. (2011). "Virtual Issue on Nanomaterials for Drug Delivery." Acs Nano **5**(2): 681-684.

Hayward, R. C. and D. J. Pochan (2010). "Tailored Assemblies of Block Copolymers in Solution: It Is All about the Process." Macromolecules **43**(8): 3577-3584.

Hayward, R. C., A. S. Utada, N. Dan and D. A. Weitz (2006). "Dewetting instability during the formation of polymersomes from block-copolymer-stabilized double emulsions." Langmuir **22**(10): 4457-4461.

Hong, L., G. Sun, J. Cai and T. Ngai (2012). "One-Step Formation of W/O/W Multiple Emulsions Stabilized by Single Amphiphilic Block Copolymers." Langmuir **28**(5): 2332-2336.

Hruby, M., C. Konak, J. Kucka, M. Vetrik, S. K. Filippov, D. Vetvicka, H. Mackova, G. Karlsson, K. Edwards, B. Rihova and K. Ulbrich (2009). "Thermoresponsive, Hydrolytically Degradable Polymer Micelles Intended for Radionuclide Delivery." Macromol Biosci **9**(10): 1016-1027.

Hu, Y. H., J. O. You, D. T. Auguste, Z. G. Suo and J. J. Vlassak (2012). "Indentation: A simple, nondestructive method for characterizing the mechanical and transport properties of pH-sensitive hydrogels." J Mater Res **27**(1): 152-160.

Huang, J., M. Juszkiewicz, W. H. de Jeu, E. Cerda, T. Emrick, N. Menon and T. P. Russell (2007). "Capillary wrinkling of floating thin polymer films." Science **317**(5838): 650-653.

Huang, W., W. Wang, P. Wang, C. N. Zhang, Q. Tian, Y. Zhang, X. H. Wang, R. T. Cha, C. H. Wang and Z. Yuan (2011). "Glycyrrhetinic acid-functionalized degradable micelles as liver-targeted drug carrier." J Mater Sci-Mater M **22**(4): 853-863.

Iamsaard, S., S. J. Asshoff, B. Matt, T. Kudernac, J. J. L. M. Cornelissen, S. P. Fletcher and N. Katsonis (2014). "Conversion of light into macroscopic helical motion." Nat Chem **6**(3): 229-235.

Insin, N., J. B. Tracy, H. Lee, J. P. Zimmer, R. M. Westervelt and M. G. Bawendi (2008). "Incorporation of iron oxide nanoplarticles and quantum dots into silica microspheres." Acs Nano **2**(2): 197-202.

Ionov, L. (2013). "3D Microfabrication using Stimuli-Responsive Self-Folding Polymer Films." Polym Rev **53**(1): 92-107.

Ionov, L. (2013). "Biomimetic Hydrogel-Based Actuating Systems." Advanced Functional Materials **23**(36): 4555-4570.

Jager-Lezer, N., I. Terrisse, F. Bruneau, S. Tokgoz, L. Ferreira, D. Clausse, M. Seiller and J. L. Grossiord (1997). "Influence of lipophilic surfactant on the release kinetics of water-soluble molecules entrapped in a W/O/W multiple emulsion." Journal of Controlled Release **45**(1): 1-13.

Jain, S. and F. S. Bates (2003). "On the origins of morphological complexity in block copolymer surfactants." Science **300**(5618): 460-464.

Jana, N. R., L. Gearheart and C. J. Murphy (2001). "Seeding growth for size control of 5-40 nm diameter gold nanoparticles." Langmuir **17**(22): 6782-6786.

Jiao, J. and D. J. Burgess (2003). "Rheology and stability of water-in-oil-in-water multiple emulsions containing Span 83 and Tween 80." Aaps Pharmsci **5**(1).

Jiao, J., D. G. Rhodes and D. J. Burgess (2002). "Multiple emulsion stability: Pressure balance and interfacial film strength." Journal of Colloid and Interface Science **250**(2): 444-450.

Kamps, A. C., B. L. Sanchez-Gaytan, R. J. Hickey, N. Clarke, M. Fryd and S. J. Park (2010). "Nanoparticle-Directed Self-Assembly of Amphiphilic Block Copolymers." Langmuir **26**(17): 14345-14350.

Kang, S.-M., A. Kumar, C.-H. Choi, K. E. Tettey, C.-S. Lee, D. Lee and B. J. Park (2014). "Triblock Cylinders at Fluid–Fluid Interfaces." Langmuir **30**(44): 13199-13204.

Kanouni, M., H. L. Rosano and N. Naouli (2002). "Preparation of a stable double emulsion (W1/O/W2): role of the interfacial films on the stability of the system." Advances in Colloid and Interface Science **99**(3): 229-254.

Karthaus, O., N. Maruyama, X. Cieren, M. Shimomura, H. Hasegawa and T. Hashimoto (2000). "Water-Assisted Formation of Micrometer-Size Honeycomb Patterns of Polymers." Langmuir **16**(15): 6071-6076.

Kaufman, J. D. and C. M. Klapperich (2009). "Surface detection errors cause overestimation of the modulus in nanoindentation on soft materials." Journal of the Mechanical Behavior of Biomedical Materials **2**(4): 312-317.

Kempaiah, R. and Z. H. Nie (2014). "From nature to synthetic systems: shape transformation in soft materials." J Mater Chem B **2**(17): 2357-2368.

Khon, E., A. Mereshchenko, A. N. Tarnovsky, K. Acharya, A. Klinkova, N. N. Hewa-Kasakarage, I. Nemitz and M. Zamkov (2011). "Suppression of the Plasmon Resonance in Au/CdS Colloidal Nanocomposites." Nano Lett **11**(4): 1792-1799.

Kim, B.-S. and T. A. Taton (2007). "Multicomponent Nanoparticles via Self-Assembly with Cross-Linked Block Copolymer Surfactants." Langmuir **23**(4): 2198-2202.

Kim, C. S. and S. M. Oh (2000). "Importance of donor number in determining solvating ability of polymers and transport properties in gel-type polymer electrolytes." Electrochimica Acta **45**(13): 2101-2109.

Kim, H. Y. and L. Mahadevan (2006). "Capillary rise between elastic sheets." J Fluid Mech **548**: 141-150.

Kim, J.-H., A. Nizami, Y. Hwangbo, B. Jang, H.-J. Lee, C.-S. Woo, S. Hyun and T.-S. Kim (2013). "Tensile testing of ultra-thin films on water surface." Nat Commun **4**.

Kim, J., J. A. Hanna, M. Byun, C. D. Santangelo and R. C. Hayward (2012). "Designing Responsive Buckled Surfaces by Halftone Gel Lithography." Science **335**(6073): 1201-1205.

Kim, J., J. A. Hanna, R. C. Hayward and C. D. Santangelo (2012). "Thermally responsive rolling of thin gel strips with discrete variations in swelling." Soft Matter **8**(8): 2375-2381.

Kim, S. H., A. D. Hollingsworth, S. Sacanna, S. J. Chang, G. Lee, D. J. Pine and G. R. Yi (2012). "Synthesis and Assembly of Colloidal Particles with Sticky Dimples." J Am Chem Soc **134**(39): 16115-16118.

Kim, S. H., H. C. Shum, J. W. Kim, J. C. Cho and D. A. Weitz (2011). "Multiple Polymersomes for Programmed Release of Multiple Components." J Am Chem Soc **133**(38): 15165-15171.

Kim, S. H. and D. A. Weitz (2011). "One-Step Emulsification of Multiple Concentric Shells with Capillary Microfluidic Devices." Angew Chem Int Edit **50**(37): 8731-8734.

King, H., R. D. Schroll, B. Davidovitch and N. Menon (2012). "Elastic sheet on a liquid drop reveals wrinkling and crumpling as distinct symmetry-breaking instabilities." P Natl Acad Sci USA **109**(25): 9716-9720.

Klein, Y., E. Efrati and E. Sharon (2007). "Shaping of elastic sheets by prescription of non-Euclidean metrics." Science **315**(5815): 1116-1120.

Koo, H., M. S. Huh, J. H. Ryu, D. E. Lee, I. C. Sun, K. Choi, K. Kim and I. C. Kwon (2011). "Nanoprobes for biomedical imaging in living systems." Nano Today **6**(2): 204-220.

Kralchevsky, P. A. and N. D. Denkov (2001). "Capillary forces and structuring in layers of colloid particles." Current Opinion in Colloid & Interface Science **6**(4): 383-401.

Kralchevsky, P. A. and K. Nagayama (2000). "Capillary interactions between particles bound to interfaces, liquid films and biomembranes." Advances in Colloid and Interface Science **85**(2-3): 145-192.

Langevin, D. (1992). "Micelles and Microemulsions." Annu Rev Phys Chem **43**: 341-369.

Lee, K. M., T. J. Bunning and T. J. White (2012). "Autonomous, Hands-Free Shape Memory in Glassy, Liquid Crystalline Polymer Networks." Advanced Materials **24**(21): 2839-2843.

Lee, M. H., K. C. Hribar, T. Brugarolas, N. P. Kamat, J. A. Burdick and D. Lee (2012). "Harnessing Interfacial Phenomena to Program the Release Properties of Hollow Microcapsules." Advanced Functional Materials **22**(1): 131-138.

Lendlein, A. and S. Kelch (2002). "Shape-Memory Polymers." Angewandte Chemie International Edition **41**(12): 2034-2057.

Lewandowski, E. P., J. A. Bernate, A. Tseng, P. C. Searson and K. J. Stebe (2009). "Oriented assembly of anisotropic particles by capillary interactions." Soft Matter **5**(4): 886-890.

Lewandowski, E. P., M. Cavallaro, L. Botto, J. C. Bernate, V. Garbin and K. J. Stebe (2010). "Orientation and Self-Assembly of Cylindrical Particles by Anisotropic Capillary Interactions." Langmuir **26**(19): 15142-15154.

Lewandowski, E. P., P. C. Searson and K. J. Stebe (2006). "Orientation of a nanocylinder at a fluid interface." J Phys Chem B **110**(9): 4283-4290.

Lewicka, M., L. Mahadevan and M. R. Pakzad (2011). "The Foppl-von Karman equations for plates with incompatible strains." P Roy Soc a-Math Phy **467**(2126): 402-426.

Li, B., Y. P. Cao, X. Q. Feng and H. J. Gao (2012). "Mechanics of morphological instabilities and surface wrinkling in soft materials: a review." Soft Matter **8**(21): 5728-5745.

Li, H. A., X. Y. Guo, R. G. Nuzzo and K. J. Hsia (2010). "Capillary induced self-assembly of thin foils into 3D structures." J Mech Phys Solids **58**(12): 2033-2042.

Li, W., J. F. Li, J. Gao, B. H. Li, Y. Xia, Y. C. Meng, Y. S. Yu, H. W. Chen, J. X. Dai, H. Wang and Y. J. Guo (2011). "The fine-tuning of thermosensitive and degradable polymer micelles for enhancing intracellular uptake and drug release in tumors." Biomaterials **32**(15): 3832-3844.

Li, W., S. Liu, R. Deng and J. Zhu (2011). "Encapsulation of Nanoparticles in Block Copolymer Micellar Aggregates by Directed Supramolecular Assembly." Angewandte Chemie, International Edition **50**(26): 5865-5868.

Li, Z. Y., J. Yuan, Y. Chen, R. E. Palmer and J. P. Wilcoxon (2005). "Local three-dimensional visualization of nanoparticle assemblies." Adv Mater **17**(23): 2885-2888.

Liang, H. Y. and L. Mahadevan (2009). "The shape of a long leaf." P Natl Acad Sci USA **106**(52): 22049-22054.

Liang, H. Y. and L. Mahadevan (2011). "Growth, geometry, and mechanics of a blooming lily." P Natl Acad Sci USA **108**(14): 5516-5521.

Lindenstruth, K. and B. W. Müller (2004). "W/O/W multiple emulsions with diclofenac sodium." European Journal of Pharmaceutics and Biopharmaceutics **58**(3): 621-627.

Linder, V., B. D. Gates, D. Ryan, B. A. Parviz and G. M. Whitesides (2005). "Water-Soluble Sacrificial Layers for Surface Micromachining." Small **1**(7): 730-736.

Liu, C., H. Qin and P. T. Mather (2007). "Review of progress in shape-memory polymers." J Mater Chem **17**(16): 1543-1558.

Liu, L., W. Wang, X.-J. Ju, R. Xie and L.-Y. Chu (2010). "Smart thermo-triggered squirting capsules for nanoparticle delivery." Soft Matter **6**(16): 3759-3763.

Lopez-Lorente, A. I., B. M. Simonet and M. Valcarcel (2011). "Analytical potential of hybrid nanoparticles." Anal Bioanal Chem **399**(1): 43-54.

Lopez-Montilla, J. C., P. E. Herrera-Morales, S. Pandey and D. O. Shah (2002). "Spontaneous emulsification: Mechanisms, physicochemical aspects, modeling, and applications." J Disper Sci Technol **23**(1-3): 219-268.

Loudet, J. C., A. M. Alsayed, J. Zhang and A. G. Yodh (2005). "Capillary interactions between anisotropic colloidal particles." Physical Review Letters **94**(1).

Luo, Y. N., D. Y. Chen, Y. Zhao, C. Wei, X. T. Zhao, W. T. Yue, R. Long, J. B. Wang and J. Chen (2014). "A constriction channel based microfluidic system enabling continuous characterization of cellular instantaneous Young's modulus." Sensors and Actuators B: Chemical **202**(0): 1183-1189.

Mabrouk, E., D. Cuvelier, L.-L. Pontani, B. Xu, D. Levy, P. Keller, F. Brochard-Wyart, P. Nassoy and M.-H. Li (2009). "Formation and material properties of giant liquid crystal polymersomes." Soft Matter **5**(9): 1870-1878.

Mai, Y. Y. and A. Eisenberg (2011). "Controlled Incorporation of Particles into the Central Portion of Block Copolymer Rods and Micelles." Macromolecules **44**(8): 3179-3183.

Malachowski, K., J. Breger, H. R. Kwag, M. O. Wang, J. P. Fisher, F. M. Selaru and D. H. Gracias (2014). "Stimuli-Responsive Theragrippers for Chemomechanical Controlled Release." Angewandte Chemie International Edition: n/a-n/a.

Marder, M. and N. Papanicolaou (2006). "Geometry and elasticity of strips and flowers." J Stat Phys **125**(5-6): 1069-1096.

Mark, J. E. (2007). Physical properties of polymers handbook. New York, Springer.

Mastrangelo, C. H. and C. H. Hsu (1993). "Mechanical stability and adhesion of microstructures under capillary forces. I. Basic theory." Microelectromechanical Systems, Journal of **2**(1): 33-43.

Mezzenga, R., B. M. Folmer and E. Hughes (2004). "Design of Double Emulsions by Osmotic Pressure Tailoring." Langmuir **20**(9): 3574-3582.

Mitragotri, S. and J. Lahann (2009). "Physical approaches to biomaterial design." Nat Mater **8**(1): 15-23.

Miyazawa, K., I. Yajima, I. Kaneda and T. Yanaki (2000). "Preparation of a new soft capsule for cosmetics." J Cosmet Sci **51**(4): 239-252.

Modes, C. D., K. Bhattacharya and M. Warner (2011). "Gaussian curvature from flat elastica sheets." P Roy Soc a-Math Phy **467**(2128): 1121-1140.

Moshe, M., E. Sharon and R. Kupferman (2013). "Pattern selection and multiscale behaviour in metrically discontinuous non-Euclidean plates." Nonlinearity **26**(12): 3247-3258.

Mouthuy, P.-O., M. Coulombier, T. Pardoen, J.-P. Raskin and A. M. Jonas (2012). "Overcurvature describes the buckling and folding of rings from curved origami to foldable tents." Nat Commun **3**: 1290.

Muller, M. M., M. Ben Amar and J. Guven (2008). "Conical Defects in Growing Sheets." Physical Review Letters **101**(15).

Na, J.-H. and R. C. Hayward in preparation.

Narang, A. S., D. Delmarre and D. Gao (2007). "Stable drug encapsulation in micelles and microemulsions." International Journal of Pharmaceutics **345**(1-2): 9-25.

Nicolson, M. M. (1949). "The Interaction between Floating Particles." P Camb Philos Soc **45**(2): 288-295.

Nishiyama, N. (2007). "Nanomedicine - Nanocarriers shape up for long life." Nat Nanotechnol **2**(4): 203-204.

Norton, J., K. R. Malik, J. A. Darr and I. Rehman (2006). "Recent developments in processing and surface modification of hydroxyapatite." Adv Appl Ceram **105**(3): 113-139.

O'Reilly, R. K., C. J. Hawker and K. L. Wooley (2006). "Cross-linked block copolymer micelles: functional nanostructures of great potential and versatility." Chem Soc Rev **35**(11): 1068-1083.

Ogawa, Y., M. Yamamoto, H. Okada, T. Yashiki and T. Shimamoto (1988). "A New Technique to Efficiently Entrap Leuprolide Acetate into Microcapsules of Polylactic Acid or Copoly(Lactic/Glycolic) Acid." Chemical & Pharmaceutical Bulletin **36**(3): 1095-1103.

Ouchi, T., A. Hamada and Y. Ohya (1999). "Biodegradable microspheres having reactive groups prepared from L-lactic acid-depsipeptide copolymers." Macromolecular Chemistry and Physics **200**(2): 436-441.

Palencia, M. and B. L. Rivas (2011). "Metal-ion retention properties of water-soluble amphiphilic block copolymer in double emulsion systems (w/o/w) stabilized by non-ionic surfactants." Journal of Colloid and Interface Science **363**(2): 682-689.

Park, B. J., C.-H. Choi, S.-M. Kang, K. E. Tettey, C.-S. Lee and D. Lee (2013). "Double Hydrophilic Janus Cylinders at an Air–Water Interface." Langmuir **29**(6): 1841-1849.

Park, B. J., C.-H. Choi, S.-M. Kang, K. E. Tettey, C.-S. Lee and D. Lee (2013). "Geometrically and chemically anisotropic particles at an oil-water interface." Soft Matter **9**(12): 3383-3388.

Park, J.-H., G. von Maltzahn, E. Ruoslahti, S. N. Bhatia and M. J. Sailor (2008). "Micellar Hybrid Nanoparticles for Simultaneous Magnetofluorescent Imaging and Drug Delivery." Angewandte Chemie, International Edition **47**(38): 7284-7288.

Park, J. and J. Moon (2006). "Control of Colloidal Particle Deposit Patterns within Picoliter Droplets Ejected by Ink-Jet Printing." Langmuir **22**(8): 3506-3513.

Peng, X. G. and Z. A. Peng (2001). "Formation of high-quality CdTe, CdSe, and CdS nanocrystals using CdO as precursor." J Am Chem Soc **123**(1): 183-184.

Peng, Z. A. and X. G. Peng (2002). "Nearly monodisperse and shape-controlled CdSe nanocrystals via alternative routes: Nucleation and growth." J Am Chem Soc **124**(13): 3343-3353.

Petkov, J. T., T. D. Gurkov and B. E. Campbell (2001). "Measurement of the Yield Stress of Gellike Protein Layers on Liquid Surfaces by Means of an Attached Particle." Langmuir **17**(15): 4556-4563.

Pickering, S. U. (1907). "CXCVI.-Emulsions." Journal of the Chemical Society, Transactions **91**(0): 2001-2021.

Py, C., P. Reverdy, L. Doppler, J. Bico, B. Roman and C. N. Baroud (2007). "Capillary Origami: Spontaneous Wrapping of a Droplet with an Elastic Sheet." Physical Review Letters **98**(15): 156103.

Quarta, A., R. Di Corato, L. Manna, A. Ragusa and T. Pellegrino (2007). "Fluorescent-magnetic hybrid nanostructures: Preparation, properties, and applications in biology." Ieee T Nanobiosci **6**(4): 298-308.

Raccurt, O., F. Tardif, F. A. d'Avitaya and T. Vareine (2004). "Influence of liquid surface tension on stiction of SOI MEMS." J Micromech Microeng **14**(7): 1083-1090.

Ramsden, W. (1903). "Separation of Solids in the Surface-Layers of Solutions and 'Suspensions' (Observations on Surface-Membranes, Bubbles, Emulsions, and Mechanical Coagulation). -- Preliminary Account." Proceedings of the Royal Society of London **72**(477-486): 156-164.

Ren, J. and Q. Z. Zou (2014). "A Control-Based Approach to Accurate Nanoindentation Quantification in Broadband Nanomechanical Measurement Using Scanning Probe Microscope." Ieee T Nanotechnol **13**(1): 46-54.

Rettler, E., S. Hoeppener, B. W. Sigusch and U. S. Schubert (2013). "Mapping the mechanical properties of biomaterials on different length scales: depth-sensing indentation and AFM based nanoindentation." J Mater Chem B **1**(22): 2789-2806.

Rezvantalab, H. and S. Shojaei-Zadeh (2013). "Role of Geometry and Amphiphilicity on Capillary-Induced Interactions between Anisotropic Janus Particles." Langmuir **29**(48): 14962-14970.

Rodríguez-Hernández, J., F. Chécot, Y. Gnanou and S. Lecommandoux (2005). "Toward 'smart' nano-objects by self-assembly of block copolymers in solution." Progress in Polymer Science **30**(7): 691-724.

Roman, B. and J. Bico (2010). "Elasto-capillarity: deforming an elastic structure with a liquid droplet." J Phys-Condens Mat **22**(49).

Rother, G. and G. H. Findenegg (1998). "Monolayer firms of PS-b-PEO diblock copolymers at the air/water- and an oil/water-interface." Colloid Polym Sci **276**(6): 496-502.

Roy, D., W. L. A. Brooks and B. S. Sumerlin (2013). "New directions in thermoresponsive polymers." Chem Soc Rev **42**(17): 7214-7243.

Ruan, G., D. Thakur, S. Deng, S. Hawkins and J. O. Winter (2010). "Fluorescent-magnetic nanoparticles for imaging and cell manipulation." Proc. Inst. Mech. Eng., Part N: J. Nanoengineering and Nanosystems **223**(3): 81-86.

Ruan, G., G. Vieira, T. Henighan, A. Chen, D. Thakur, R. Sooryakumar and J. O. Winter (2010). "Simultaneous Magnetic Manipulation and Fluorescent Tracking of Multiple Individual Hybrid Nanostructures." Nano Lett **10**(6): 2220-2224.

Ruan, G. and J. O. Winter (2011). "Alternating-Color Quantum Dot Nanocomposites for Particle Tracking." Nano Lett **11**(3): 941-945.

Rubinstein, M., R. H. Colby, A. V. Dobrynin and J.-F. Joanny (1996). "Elastic Modulus and Equilibrium Swelling of Polyelectrolyte Gels." Macromolecules **29**(1): 398-406.

Sadasivan, S., D. Khushalani and S. Mann (2005). "Synthesis of calcium phosphate nanofilaments in reverse micelles." Chemistry of Materials **17**(10): 2765-2770.

Sameh, H., E. Wafa, B. Sihem and L.-C. Fernando (2012). "Influence of Diffusive Transport on the Structural Evolution of W/O/W Emulsions." Langmuir **28**(51): 17597-17608.

Scarpa, J. S., D. D. Mueller and I. M. Klotz (1967). "Slow Hydrogen-Deuterium Exchange in a Non-Alpha-Helical Polyamide." J Am Chem Soc **89**(24): 6024-&.

Seifriz, W. (1925). "Studies in emulsions." J Phys Chem-Us **29**: 834-841.

Sharon, E. and E. Efrati (2010). "The mechanics of non-Euclidean plates." Soft Matter **6**(22): 5693-5704.

Shevchenko, E. V., M. I. Bodnarchuk, M. V. Kovalenko, D. V. Talapin, R. K. Smith, S. Aloni, W. Heiss and A. P. Alivisatos (2008). "Gold/Iron Oxide Core/Hollow-Shell Nanoparticles." Adv Mater **20**(22): 4323-4329.

Shi, J. J., A. R. Votruba, O. C. Farokhzad and R. Langer (2010). "Nanotechnology in Drug Delivery and Tissue Engineering: From Discovery to Applications." Nano Lett **10**(9): 3223-3230.

Shi, W. L., H. Zeng, Y. Sahoo, T. Y. Ohulchanskyy, Y. Ding, Z. L. Wang, M. Swihart and P. N. Prasad (2006). "A general approach to binary and ternary hybrid nanocrystals." Nano Lett **6**(4): 875-881.

Shmuylovich, L., A. Q. Shen and H. A. Stone (2002). "Surface morphology of drying latex films: Multiple ring formation." Langmuir **18**(9): 3441-3445.

Shum, H. C., A. Bandyopadhyay, S. Bose and D. A. Weitz (2009). "Double Emulsion Droplets as Microreactors for Synthesis of Mesoporous Hydroxyapatite." Chemistry of Materials **21**(22): 5548-5555.

Shum, H. C., Y. J. Zhao, S. H. Kim and D. A. Weitz (2011). "Multicompartment Polymersomes from Double Emulsions." Angew Chem Int Edit **50**(7): 1648-1651.

Sitt, A., A. Salant, G. Menagen and U. Banin (2011). "Highly Emissive Nano Rod-in-Rod Heterostructures with Strong Linear Polarization." Nano Lett **11**(5): 2054-2060.

Skouri, R., F. Schosseler, J. P. Munch and S. J. Candau (1995). "Swelling and Elastic Properties of Polyelectrolyte Gels." Macromolecules **28**(1): 197-210.

Srinivasarao, M., D. Collings, A. Philips and S. Patel (2001). "Three-dimensionally ordered array of air bubbles in a polymer film." Science **292**(5514): 79-83.

Stafford, C. M., C. Harrison, K. L. Beers, A. Karim, E. J. Amis, M. R. VanLandingham, H.-C. Kim, W. Volksen, R. D. Miller and E. E. Simonyi (2004). "A buckling-based metrology for measuring the elastic moduli of polymeric thin films." Nat Mater **3**(8): 545-550.

Stebe, K. J. and E. P. Lewandowski (2009). "COLL 66-Oriented assembly of anisotropic particles by capillary interactions." Abstr Pap Am Chem S **238**.

Stenzel, M. H. (2008). "RAFT polymerization: an avenue to functional polymeric micelles for drug delivery." Chem Commun(30): 3486-3503.

Stoychev, G., N. Puretskiy and L. Ionov (2011). "Self-folding all-polymer thermoresponsive microcapsules." Soft Matter **7**(7): 3277-3279.

Stoychev, G., S. Zakharchenko, S. Turcaud, J. W. C. Dunlop and L. Ionov (2012). "Shape-Programmed Folding of Stimuli-Responsive Polymer Bilayers." Acs Nano **6**(5): 3925-3934.

Stuart, M. A. C., W. T. S. Huck, J. Genzer, M. Muller, C. Ober, M. Stamm, G. B. Sukhorukov, I. Szleifer, V. V. Tsukruk, M. Urban, F. Winnik, S. Zauscher, I. Luzinov and S. Minko (2010). "Emerging applications of stimuli-responsive polymer materials." Nature Materials **9**(2): 101-113.

Studart, A. R. and R. M. Erb (2014). "Bioinspired materials that self-shape through programmed microstructures." Soft Matter **10**(9): 1284-1294.

Sudeep, P. K. and T. Emrick (2009). "Pearls of Wisdom: Stringing Nanoparticles and Polymers into New Assemblies and Materials." Acs Nano **3**(10): 2870-2875.

Sun, S. H., H. Zeng, D. B. Robinson, S. Raoux, P. M. Rice, S. X. Wang and G. X. Li (2004). "Monodisperse MFe2O4 (M = Fe, Co, Mn) nanoparticles." J Am Chem Soc **126**(1): 273-279.

Syms, R. R. A., E. M. Yeatman, V. M. Bright and G. M. Whitesides (2003). "Surface tension-powered self-assembly of microstructures - the state-of-the-art." Microelectromechanical Systems, Journal of **12**(4): 387-417.

Tanaka, T., M. Morigami and N. Atoda (1993). "Mechanism of Resist Pattern Collapse during Development Process." Jpn J Appl Phys 1 **32**(12B): 6059-6064.

Therien-Aubin, H., Z. L. Wu, Z. H. Nie and E. Kumacheva (2013). "Multiple Shape Transformations of Composite Hydrogel Sheets." J Am Chem Soc **135**(12): 4834-4839.

Toomey, R., D. Freidank and J. Ruhe (2004). "Swelling behavior of thin, surface-attached polymer networks." Macromolecules **37**(3): 882-887.

Utada, A. S., E. Lorenceau, D. R. Link, P. D. Kaplan, H. A. Stone and D. A. Weitz (2005). "Monodisperse Double Emulsions Generated from a Microcapillary Device." Science **308**(5721): 537-541.

van Honschoten, J. W., J. W. Berenschot, T. Ondarçuhu, R. G. P. Sanders, J. Sundaram, M. Elwenspoek and N. R. Tas (2010). "Elastocapillary fabrication of three-dimensional microstructures." Applied Physics Letters **97**(1): -.

van Oosten, C. L., C. W. M. Bastiaansen and D. J. Broer (2009). "Printed artificial cilia from liquid-crystal network actuators modularly driven by light." Nature Materials **8**(8): 677-682.

van Dongen, S. F. M., W. P. R. Verdurmen, R. J. R. W. Peters, R. J. M. Nolte, R. Brock and J. C. M. van Hest (2010). "Cellular Integration of an Enzyme-Loaded Polymersome Nanoreactor." Angewandte Chemie International Edition **49**(40): 7213-7216.

VanLandingham, M. R., J. S. Villarrubia, W. F. Guthrie and G. F. Meyers (2001). "Nanoindentation of polymers: An overview." Macromol Symp **167**: 15-43.

Vinckier, A. and G. Semenza (1998). "Measuring elasticity of biological materials by atomic force microscopy." Febs Lett **430**(1-2): 12-16.

Walther, A., J. Yuan, V. Abetz and A. H. E. Muller (2009). "Structure-Tunable Bidirectional Hybrid Nanowires via Multicompartment Cylinders." Nano Lett **9**(5): 2026-2030.

Wang, H., X. S. Wang, M. A. Winnik and I. Manners (2008). "Redox-mediated synthesis and encapsulation of inorganic nanoparticles in shell-cross-linked cylindrical polyferrocenylsilane block copolymer micelles." J Am Chem Soc **130**(39): 12921-12930.

Wang, J. Y., T. Xu, J. M. Leiston-Belanger, S. Gupta and T. P. Russell (2006). "Ion complexation: A route to enhanced block copolymer alignment with electric fields." Physical Review Letters **96**(12): 128301.

Wang, M. F., M. Zhang, J. Li, S. Kumar, G. C. Walker, G. D. Scholes and M. A. Winnik (2010). "Self-Assembly of Colloidal Quantum Dots on the Scaffold of Triblock Copolymer Micelles." Acs Appl Mater Inter **2**(11): 3160-3169.

Wang, X. S., H. Wang, N. Coombs, M. A. Winnik and I. Manners (2005). "Redox-induced synthesis and encapsulation of metal nanoparticles in shell-cross-linked organometallic nanotubes." J Am Chem Soc **127**(25): 8924-8925.

White, E. M., J. Yatvin, J. B. Grubbs, J. A. Bilbrey and J. Locklin (2013). "Advances in smart materials: Stimuli-responsive hydrogel thin films." J Polym Sci Pol Phys **51**(14): 1084-1099.

White, J. H. (1969). "Self-Linking and the Gauss Integral in Higher Dimensions." Am. J. Math. **91**: 693-728.

Widawski, G., M. Rawiso and B. Francois (1994). "Self-Organized Honeycomb Morphology of Star-Polymer Polystyrene Films." Nature **369**(6479): 387-389.

Wu, Z. L., M. Moshe, J. Greener, H. Therien-Aubin, Z. Nie, E. Sharon and E. Kumacheva (2013). "Three-dimensional shape transformations of hydrogel sheets induced by small-scale modulation of internal stresses." Nat Commun **4**: 1586.

Wyman, I., G. Njikang and G. Liu (2011). "When emulsification meets self-assembly: The role of emulsification in directing block copolymer assembly." Progress in Polymer Science **36**(9): 1152-1183.

Wyss, H. M., T. Franke, E. Mele and D. A. Weitz (2010). "Capillary micromechanics: Measuring the elasticity of microscopic soft objects." Soft Matter **6**(18): 4550-4555.

Wyss, H. M., J. M. Henderson, F. J. Byfield, L. A. Bruggeman, Y. X. Ding, C. F. Huang, J. H. Suh, T. Franke, E. Mele, M. R. Pollak, J. H. Miner, P. A. Janmey, D. A. Weitz

and R. T. Miller (2011). "Biophysical properties of normal and diseased renal glomeruli." Am J Physiol-Cell Ph **300**(3): C397-C405.

Xu, T., J. T. Goldbach, J. Leiston-Belanger and T. P. Russell (2004). "Effect of ionic impurities on the electric field alignment of diblock copolymer thin films." Colloid Polym Sci **282**(8): 927-931.

Yafei, W., Z. Tao and H. Gang (2005). "Structural Evolution of Polymer-Stabilized Double Emulsions." Langmuir **22**(1): 67-73.

Yao, L., L. Botto, J. M. Cavallaro, B. J. Bleier, V. Garbin and K. J. Stebe (2013). "Near field capillary repulsion." Soft Matter **9**(3): 779-786.

Yi, D. K., S. T. Selvan, S. S. Lee, G. C. Papaefthymiou, D. Kundaliya and J. Y. Ying (2005). "Silica-coated nanocomposites of magnetic nanoparticles and quantum dots." J Am Chem Soc **127**(14): 4990-4991.

Yu, H., M. Chen, P. M. Rice, S. X. Wang, R. L. White and S. H. Sun (2005). "Dumbbell-like bifunctional Au-Fe3O4 nanoparticles." Nano Lett **5**(2): 379-382.

Yu, Y. L., M. Nakano and T. Ikeda (2003). "Directed bending of a polymer film by light - Miniaturizing a simple photomechanical system could expand its range of applications." Nature **425**(6954): 145-145.

Yunker, P. J., T. Still, M. A. Lohr and A. G. Yodh (2011). "Suppression of the coffee-ring effect by shape-dependent capillary interactions." Nature **476**(7360): 308-311.

Zakharchenko, S., N. Puretskiy, G. Stoychev, M. Stamm and L. Ionov (2010). "Temperature controlled encapsulation and release using partially biodegradable thermo-magneto-sensitive self-rolling tubes." Soft Matter **6**(12): 2633-2636.

Zhang, L., W. G. Liu, L. Lin, D. Y. Chen and M. H. Stenze (2008). "Degradable Disulfide Core-Cross-Linked Micelles as a Drug Delivery System Prepared from Vinyl Functionalized Nucleosides via the RAFT Process." Biomacromolecules **9**(11): 3321-3331.

Zhang, M., L. Rene-Boisneuf, Y. W. Hu, K. Moozeh, Y. Hassan, G. Scholes and M. A. Winnik (2011). "Preparation and photo/chemical-activation of wormlike network micelles of core-shell quantum dots and block copolymer hybrids." J Mater Chem **21**(26): 9692-9701.

Zhang, M., M. F. Wang, S. He, J. S. Qian, A. Saffari, A. Lee, S. Kumar, Y. Hassan, A. Guenther, G. Scholes and M. A. Winnik (2010). "Sphere-to-Wormlike Network Transition of Block Copolymer Micelles Containing CdSe Quantum Dots in the Corona." Macromolecules **43**(11): 5066-5074.

Zhu, J. and R. C. Hayward (2008). "Hierarchically Structured Microparticles Formed by Interfacial Instabilities of Emulsion Droplets Containing Amphiphilic Block Copolymers." Angewandte Chemie International Edition **47**(11): 2113-2116.

Zhu, J. and R. C. Hayward (2008). "Spontaneous Generation of Amphiphilic Block Copolymer Micelles with Multiple Morphologies through Interfacial Instabilities." J Am Chem Soc **130**(23): 7496-7502.

Zhu, J. and R. C. Hayward (2012). "Interfacial tension of evaporating emulsion droplets containing amphiphilic block copolymers: Effects of solvent and polymer composition." Journal of Colloid and Interface Science **365**(1): 275-279.

Zhu, J. T., N. Ferrer and R. C. Hayward (2009). "Tuning the assembly of amphiphilic block copolymers through instabilities of solvent/water interfaces in the presence of aqueous surfactants." Soft Matter **5**(12): 2471-2478.

Zhu, J. T. and R. C. Hayward (2008). "Spontaneous generation of amphiphilic block copolymer micelles with multiple morphologies through interfacial instabilities." J Am Chem Soc **130**(23): 7496-7502.

Zimberlin, J. A., N. Sanabria-DeLong, G. N. Tew and A. J. Crosby (2007). "Cavitation rheology for soft materials." Soft Matter **3**(6): 763-767.